UNIVERSITY OF CALIFORNIA, SAN DIEGO

X-ray Diffraction from Thin Film Structures: Characterization and Modeling

A dissertation submitted in partial satisfaction of the
requirements for the degree Doctor of Philosophy
in
Physics

by

Ge Liu

Committee in charge:

Professor Ivan K. Schuller, Chair
Professor Michael Fogler
Professor Andrew C. Kummel
Professor Sunil K. Sinha
Professor Charles W. Tu

2007

The dissertation of Ge Liu is approved, and it is acceptable in quality and form for publication on microfilm:

Chair

University of California, San Diego

2007

TABLE OF CONTENTS

LIST OF FIGURES

LIST OF TABLES

ACKNOWLEDGEMENT

Many people deserve my sincere thanks for helping me reach this point. I would first thank my wife, Xiaoying and my mother, Yue, who have supported me throughout my research. Without their efforts and sacrifices, I would never have been able to complete my Ph. D. study here.

My deepest gratitude is for my advisor, Professor Ivan K. Schuller, for his insightful guidance, warm encouragement and occasionally tough criticism. But what has influenced me the most is his enthusiasm for scientific research; it is a constant reminder of what a physicist should be. Professor Sunil K. Sinha is the other mentor I should definitely thank. My x-ray knowledge began in his course "PHYS 239". His lectures introduced me to this wonderful field where new things happen every day. I thank Professor Michael Fogler, Professor Charles W. Tu and Professor Andrew C. Kummel for their insightful comments on my candidacy proposal so that my research direction was more appropriately focused.

I thank Dr. Bernd Fruhberger for his help with my research on the semiconductor superlattice. I also thank Dr. Thomas Gredig, Dr. Casey W. Miller, Dr. Amos Sharoni and Mr. Corneliu N. Colesniuc for our pleasant collaboration on organic thin film. I thank Dr. Maribel Montero and Dr. Igor Roshchin for my thorough training on the SEM, RIE, XRD and other equipment. I need to show my thanks to Mr. David Tagatac for his valuable help on my thesis manuscript. I also thank Mr. Changpeng Li for his aid in LaTeX editing. I would also like to thank other group members, Ms. Susan Hall and Ms. Erin Gerlach, for their everyday support.

I am very grateful for the samples provided by Dr. Gail J. Brown and Dr. Heather J. Haugan from the US Air Force Research Lab. Their state-of-the-art MBE fabrication process was instrumental in preparing the samples used in this work.

Finally, I would like to mention my friends in San Diego who have made

me feel at home in a new city.

This work was supported by AFOSR MURI # F49620-02-1-0288.

VITA

1997	Bachelor of Science, Fudan University, China
2000	Master of Science, Fudan University, China
2007	Doctor of Philosophy, University of California, San Diego, USA

PUBLICATIONS

"Anomalous structural phase cancellation in thin films with anisotropic molecules." Ge Liu, Thomas Gredig and Ivan K. Schuller, (Submitted to Phys. Rev. Lett.).

"Quantitative structural characterization of InAs/GaSb superlattices." Ge Liu, Bernd Fruhberger, Ivan K. Schuller, Heather J. Haugan and Gail J. Brown, J. Appl. Phys. **100**, 063536, (2006).

"Quantitative structural analysis of organic thin films: An x-ray diffraction study." Casey W. Miller, A. Sharoni, G. Liu, C. N. Colesniuc, B. Fruhberger, and Ivan K. Schuller, Phys. Rev. **B 72**, 104113 (2005).

"Magnetoresistance of mechanically stable Co nanoconstrictions." M. I. Montero, R. K. Dumas, G. Liu, M. Viret, O. M. Stoll, W. A. A. Macedo, and Ivan K. Schuller, Phys. Rev. **B 70**, 184418 (2004).

FIELDS OF STUDY

Physics

ABSTRACT OF THE DISSERTATION

X-ray Diffraction from Thin Film Structures: Characterization and Modeling

by

Ge Liu
Doctor of Philosophy in Physics
University of California, San Diego, 2007
Professor Ivan K. Schuller, Chair

InAs/GaSb superlattices grown via molecular beam epitaxy, and containing InSb-like interfacial layers, were analyzed with a combination of x-ray diffraction (XRD) and structural refinement techniques. The superlattice refinement from x-rays (SUPREX) method determines with high accuracy the average thicknesses and d-spacings of the individual InAs and GaSb layers in addition to standard structural parameters usually obtained by XRD, such as the modulation length (periodicity), average out-of-plane interplanar spacings, and total thickness. The combined SUPREX/XRD experiments show that the absence of certain odd order satellite features in the x-ray data is due to asymmetric and inhomogeneous lattice strain. *Ex situ*-annealed InAs/GaSb superlattices were studied using atomic force microscopy (AFM) and XRD methods. Results show that annealing at temperatures between 200 °C and 350 °C for 1 hour in HVAC improves the structural quality of these superlattices. Strain relaxation occurs during the annealing process indicating that there are chemical intermixing and anion segregation in the superlattices.

The effect of the inner-molecular electron density on the x-ray diffraction profile of a layer-stacked thin film is studied. Important phase information contained in the x-ray diffraction profile of highly anisotropic molecular-based thin films is charaterized. The experimental and calculated results show that the intensity distribution of the diffraction peaks belonging to the same lattice orientation

provides important structural information. For example, tilt angle and core electron density of a molecule can be determined from the intensity distribution. The out-of-plane tilt angle relaxation is studied numerically. The results show that the relaxation can only occur at the first phthalocyanine monolayer above the substrate. The lateral grain size effect and the polar angle anisotropy are studied using a three-dimensional model. The FWHM of the center peak in associated rocking curves gives lateral coherence length or lateral grain size, and the ratio of the intensities from the diffraction peaks in normal diffraction curves shows the uniaxial angular anisotropy of the phthalocyanine thin films.

I

Introduction

I.A Structure of the dissertation

This Ph. D. dissertation studies the x-ray diffraction (XRD) from the InAs/GaSb III-V semiconductor superlattices and the organic molecular beam deposition (OMBD) phthalocyanine thin films. These are two special forms of layered crystalline materials. The refinement method and the direct calculation method are applied to characterize the structures of the superlattices after intended interfacial insertion or controlled thermal processing. Another goal is to understand how essential structural features, such as the molecular structure, the angular anisotropy and the lateral grain size, affect the x-ray diffraction profile.

The layout of six chapters is as follows:

In Chapter I, the basic theory of the x-ray diffraction is presented. The background information is presented for the systems studied in this work. Recent works related to this work are introduced and reviewed. The motivations for the work are given and the strategies are discussed.

In Chapter II, a series of InAs/GaSb superlattices with controlled interfaces are studied using x-ray diffraction. The XRD profiles are characterized using SUPREX, and strain and interfacial effects are discussed.

In Chapter III, sets of identical InAs/GaSb superlattices are annealed under different circumstances. The surface morphology and the XRD profiles are studied and a criterion for the improvement of future InAs/GaSb superlattice fabrication is discovered.

In Chapter IV, OMBD phthalocyanine thin films with similar structures are fabricated. XRD experiments are performed, and a one-dimensional model is proposed to explain the difference between the XRD profiles for different types of phthalocyanines. The explanation is generalized to show how the inner-molecular phase cancellation influences the specular XRD diffraction. Using limited experimental results, we are then able to partially determine the molecular structure and arrangement.

In Chapter V, a three-dimensional model is proposed to simulate the nature of the uniaxially-aligned phthalocyanine thin film. The studies on the rocking curves and the normal diffraction profiles suggest that the in-plane coherence (lateral grain size) and the uniaxial angular distribution are important parameters but behave differently. Analysis of the rocking curves and the normal diffraction profiles may yield an estimation for the grain size of the phthalocyanine crystallites and the average off-alignment angles (deviation angles).

In Chapter VI, a philosophical remark is given about this work. It turns out that these different chapters are connected by a central idea. Some possible future topics are presented.

I.B Principles of the x-ray diffraction

Scattering occurs when a wave propagates in a medium. As a special case, when a wave is incident on a medium with a periodic structure, which has spatial modulations with the size comparable to the wavelength of the wave, diffraction

effects can be observed. So the diffraction from waves with different wavelengths reveals the structure of a medium at different length scales.

X-rays are a form of electromagnetic radiation with wavelengths in the range of 100 to 0.1 Å. This range spans the inter-atomic distances in condensed matter. In addition, the soft and hard x-rays can detect distances outside this range. So the diffraction of x-ray is a powerful technique for characterizing the structure of various kinds of objects.

A monochromatic wave in a medium displays spatial periodicity. Its period, which is called wavelength, is related to its frequency by a dispersion relation. Such a dispersion relation is an intrinsic property of the wave and the propagation medium.

Although the quantum representation and the classical representation of an x-ray wave are quite different, they are both in the form of the wave equation. Excluding the issue of energy dispersion and causality, both representations can be written as an inhomogeneous Helmholtz Equation

$$\nabla^2\psi(\mathbf{r}) + k^2 n^2(\mathbf{r})\,\psi(\mathbf{r}) = 0 \tag{I.1}$$

or

$$\nabla^2\psi(\mathbf{r}) + k^2\psi(\mathbf{r}) = \rho(\mathbf{r}) \tag{I.2}$$

where $\psi(\mathbf{r})$, $\rho(\mathbf{r})$ and k refer to the wave function, the density of the scattering source and the wave vector respectively. The wave function of the Helmholtz Equation, which is thought to be a vector field with two polarizations transverse to the wave vector $\mathbf{k}$. These polarizations are not explicitly discussed here though the correction has been implicitly included in the equation. This wave function refers to the field amplitude for classical waves or the field operator for quantum waves. The general solution to Equation I.2 can be expanded into two terms: the first is the particular solution to the equation, and the second is the general solution to its homogeneous correspondent:

$$\psi(\mathbf{r}) = \int \hat{G}(\mathbf{r}-\mathbf{r}')\rho(\mathbf{r}')\,d\mathbf{r}' + \psi_0(\mathbf{r})\,. \tag{I.3}$$

The general solution $\psi_0(\mathbf{r})$ to the homogeneous equation is the free propagation of the wave, and the first term in Equation I.3 comes from the interaction between the wave and the medium. It is usually difficult to obtain the Green's function $\hat{G}$ in Eqution I.3. However, the Green's function can be expanded by iterating on $\hat{G}_0$ derived from the homogeneous equation:

$$\hat{G} = \hat{G}_0 + \hat{G}_0\hat{\rho}\hat{G}_0 + \hat{G}_0\hat{\rho}\hat{G}_0\hat{\rho}\hat{G}_0 + \cdots \tag{I.4}$$

where the terms correspond to single scattering, double scattering and higher order processes. Because the elastic scattering cross-section of most elements are small, the higher order processes can be neglected except at very low angles and the angles near major diffraction peaks. X-rays perturb the electron distribution by removing inner-shell electrons from an atom, and also interact with the nuclei. But the latter interaction is often neglected with the Born-Oppenheimer Approximation. Then the diffraction from a medium is reduced to a simple geometrical calculation plus the phase interference, which is the so-called kinematical theory. Defining the Thomson scattering length, $r_0 = \frac{e^2}{m_e c^2} = 2.82 \times 10^{-5}$ Å, the total scattering length of an atom is

$$-r_0 f^0(\mathbf{Q}) = -r_0 \int \rho(\mathbf{r}) e^{i\mathbf{Q}\cdot\mathbf{r}} d\mathbf{r} \tag{I.5}$$

where $f^0(\mathbf{Q})$ is known as the atomic form (scattering) factor, characterizing the diffraction amplitude from the atom. This is also the forward Fourier transform of the electron density to the momentum space. Using a similar procedure, we define the total scattering length of an ensemble of different atoms as

$$-r_0 F^0(\mathbf{Q}) = -r_0 \int \sum_n \rho_n(\mathbf{r} - \mathbf{R}_n) e^{i\mathbf{Q}\cdot\mathbf{r}} d\mathbf{r} \tag{I.6}$$

and these atoms can form a molecule, a cluster or a just random congregation. In the limit of very large population, some approximations are made in order to focus on the essential features of the ensemble. For example, a constant electron density is usually selected for a uniform amorphous medium, and a density with discrete translation symmetry is given to the crystalline forms.

One essentially useful property in the context of diffraction is the Convolution Theorem, [1] which states that the Fourier transform of the convolution of two functions $f(\mathbf{r})$ and $g(\mathbf{r})$ is equal to the product of the two individual Fourier transforms $F(\mathbf{Q})$ and $G(\mathbf{Q})$. Using mathematical language, if we define the convolution of two functions $f(\mathbf{r})$ and $g(\mathbf{r})$ as $h(\mathbf{r})$, then

$$h(\mathbf{r}) = \int f(\mathbf{r}')\, g(\mathbf{r}-\mathbf{r}')\, d\mathbf{r}' \tag{I.7}$$

and its Fourier transform is written as

$$\begin{aligned} H(\mathbf{Q}) &= \int h(\mathbf{r})\, e^{i\mathbf{Q}\cdot\mathbf{r}} d\mathbf{r} \\ &= \int f(\mathbf{r}') e^{i\mathbf{Q}\cdot\mathbf{r}'} d\mathbf{r}' \int g(\mathbf{r}-\mathbf{r}')\, e^{i\mathbf{Q}\cdot(\mathbf{r}-\mathbf{r}')} d\mathbf{r} \\ &= F(\mathbf{Q})\, G(\mathbf{Q}) \end{aligned} \tag{I.8}$$

This result can be used to reduce the complexity of the diffraction from a periodic system in real space to simpler arithmetic calculations in momentum (reciprocal) space.

I.C Basic concepts on the XRD from a crystal or a thin film

The elementary unit of condensed matter is the molecule - a group of organized atoms. The scattering from a molecule is reduced to a product of the scattering from single atoms and the phase factor due to the molecule structure. We can arrange molecules in cells called unit cells, which are the fundamental units to construct a lattice. The additional phase factor introduced by the unit cell usually contains the symmetry of the lattice. By studying the scattering from a unit cell, we can obtain valuable information about the diffraction from a crystal lattice. We repeat the procedure to introduce a lattice, which is the repetition of a unit cell in three-dimensional space. The lattice conserves discrete translational symmetry, so the diffraction problem is greatly simplified by the Convolution Theorem. The phase factor, introduced by the lattice, is represented by its reciprocal lattice

or the Laue conditions. The diffraction from a lattice can also be categorized into different families of lattice planes. Each family of lattice planes yields a special condition given by Bragg's Law. The parallelism between the lattice and its reciprocal enable crystallographers to reconstruct the crystal lattice by studying the diffraction patterns from a single crystal. When the single crystal proves too difficult to obtain, alternative method is applied to characterize the crystal lattice structure, which depends on the powder XRD [2] and procedures called Rietveld refinement and related techniques. [3, 4] The characterization methods from the single crystal XRD or from the powder XRD are so powerful that even the lattice and molecular structures of very complicated macromolecules such as proteins can be obtained. [5, 6, 7, 8] Several different XRD scan modes are briefly introduced in Appendix A.

It is useful to study the deviation from the ideal structure in a crystal. Debye [9] and Waller [10] studied the thermal vibrations of atoms and molecules in a crystal. Diffuse scattering originates from the thermal vibrations. This gives information about phonon-related processes. [11, 12, 13] Other imperfections include disorder in a crystal and variations in treatment of an alloy. [14, 15, 16]

A single-crystalline thin film is similar to a crystal, but it is extended in two-dimensional space. We might think that the diffraction from a thin film might be easier to deal with because of the absent vertical dimension, but this is not necessarily true since the analysis can be complicated by the loss of the vertical discrete translational symmetry. So very specific attention should be paid here, and the general rules, which govern the three-dimensional phenomena, need verification before being directly applied to the thin film case. Whether we discuss an isolated monolayer or a surface layer of a crystal, or some other more complicated systems, the three-dimensional reciprocal space of a two-dimensional lattice is a two-dimensional array of diffraction rods. These rods are perpendicular to the two-dimensional diffraction plane. They are lines of the diffraction, which have sharp edges in both directions parallel to the film, and are continuous in the direction

perpendicular to the film. To characterize the diffraction rods is also to learn the out-of-plane structure of a thin film.

If we assume that the in-plane structure is uniform and isotropic and the out-of-plane structure only depends on the chemical modulation (and not on the lattice structure), an optical model developed in the study of optical films and multilayers can be used to reproduce all features from the out-of-plane diffraction or the specular diffraction. The diffraction from a surface is the starting point of the optical model. It is quite simple and discussed in any electrodynamics textbook. [17] The introduction of a second surface parallel to the first one yields the prototype of the diffraction from a thin film. The phase interference between the bottom and the top surfaces displays oscillations in specular diffraction measurements. These oscillations are known as Kiessig fringes. [18] The thickness of the film can be determined from Kiessig fringes using straightforward calculation. The diffraction from a stratified multilayer can be extended by recursing the reflection and transmission at every layer-interfaces which was given by Parratt. [19] The roughness of a thin film is modeled using a statistical distribution given by Sinha *et al.* [20] The diffraction from a thin film with long-range-ordered roughness shows a very interesting feature. At certain diffraction angles, the specular diffraction is completed cancelled out. This type of thin film is the x-ray corollary of an optical blazed grating. In this case, the specular diffraction is influenced by the lateral structure of the film although the diffraction equation does not explicitly include the lateral structural information. However, the fabrication of such thin film structure with lateral long-range order proves to be very difficult. Recent studies on the self-organized lateral modulation in some semiconductor superlattices and multilayers give evidence for the existence of the phenomenon. [21, 22, 23, 24]

Although the optical model is helpful in understanding the diffraction from thin films, it loses validity when the momentum transfer enters the regime where the phase cancellation between the inner-structures within a thin film is significant. This is usually called the high angle diffraction regime. The definition

of the high angle does not mean the diffraction angle must be "high". In fact, for some structures with long d-spacings, such as the phthalocyanine films which we will extensively discuss in the latter chapters, the "high" angle diffraction can happen in the low angle regime. By incorporating the inner structures within the inter-layer structure, we may reconcile the inconsistency between the optical model and the high angle diffraction. The model that includes inner-layer structure information is often known as the kinematical diffraction model because in the high angle regime, the multi-diffraction process is usually negligible. The model can be evaluated in one, two and three dimensions, depending on the structural features of the system. But in all cases, the constraint in the out-of-plane direction must be considered. One interesting example in one dimension is quasiperiodic lattices (chains) which was comprehensively studied by several groups. [25, 26, 27, 28, 29] Their approaches to the quasiperiodic lattices indicate that the well-defined periodic structure is not a necessary requirement for sharp diffraction patterns. The kinematical model can also be applied to many other systems by including "superstructure" above the usual lattice structure. Such superstructure provides diffraction features in addition to those from the usual lattice.

I.D Superstructure and the systems for this work

A superstructure is an extension of an existing structure or baseline. This term is applied to both physical structures (e.g. buildings and ships) and to conceptual structures (social science). In the category of physical systems, a superstructure usually refers to a system, which is composed of elements with internal structures. For example, a lattice with chiral symmetry can be treated as a superstructure, which is characterized by the chiral periodicity. A superlattice as shown in Figure I.1 which is a material with periodically alternating layers of several substances, is another example of superstructure. However, this definition is not complete, because when we change our perspective, a normal structure

(lattice) can also appear to be a superstructure. For instance, suppose we have a crystal composed of molecules A, which is formed from atoms B, C, D, and F. If we take A as the primitive unit, the molecular crystal is a normal structure. If we take the inner-molecular structure B-C-D-F as the primitive unit, the molecular crystal is a superstructure.

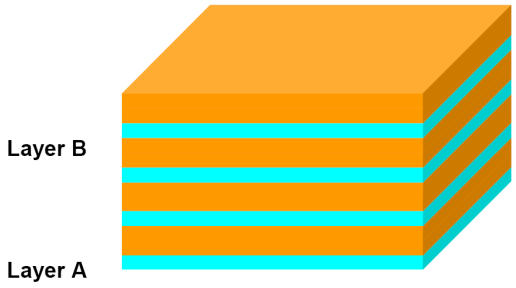

Figure I.1: The structure of a typical bilayer superlattice A/B.

The concept of superstructures either as superlattices or as the molecular crystals (e.g. phthalocyanine crystalline films) is central to the present work. The existence of superstructure in superlattices yields additional satellite diffraction peaks, which cannot be predicted without considering superstructure. The existence of superstructure in the phthalocyanine crystalline films shows unusual properties, which cannot be understood without considering superstructure either.

To clarify, let's discuss the diffraction from a superlattice A/B. Assume the d-spacing and the number of monolayers in constituent layer A are d_A and N_A respectively, and the d-spacing and the number of monolayers in constituent layer B are d_B and N_B. The modified Bragg's Law for a superlattice can be written as

$$\frac{2\sin\Theta_m}{\lambda_{X-ray}} = \frac{1}{\langle d\rangle} \pm \frac{m}{\Lambda} = \frac{N_A + N_B \pm m}{\Lambda} \tag{I.9}$$

where $\langle d\rangle = \frac{N_A d_A + N_B d_B}{N_A + N_B}$, $\Lambda = N_A d_A + N_B d_B$, and m is the index of the satellite peaks (note: for different diffraction orders, the d-spacings of monolayers and the number of monolayers can have different values). It is clear that the existence of extra periodicity yields an extra series of satellite diffraction peaks. Due to the

nature of the Fourier transform, a superstructure with a larger length scale imposes "fine-structure" in reciprocal space with a smaller length scale. The phthalocyanine crystalline film shows diffraction peaks at certain diffraction angles, which are determined by the d-spacings of the lattice when the lattice is treated as the normal structure and the molecular structure is treated as a variable. If we focus on a smaller scale and take the molecular structure as the primitive unit, the diffraction from the phthalocyanine molecule yields impact on the diffraction profiles at a larger scale (in momentum space). The superstructure can also appear in forms without periodicity. Some thin polycrystalline films are characterized by a greater probability for certain crystallographic lattice planes. This phenomenon is termed preferred orientation or texture. The texture can have a significant influence on the diffraction pattern where the density-enhanced lattice planes will accentuate the corresponding Bragg reflection intensity.

Another possible superstructure is a film with different grain size or shape. By changing the grain size or shape, the ratio of the peak intensities between the different Bragg reflections can be varied. But these two types of superstructure are irrelevant to the Convolution Theorem. Thus they need to be studied with other approaches such as geometrical averaging and size statistics. These macro-scale features are more noticeable at smaller scales in the reciprocal space.

I.E Background knowledge and the motivation

In this section, general reviews on the background information and the history of the research are given. More specific introductions addressing the different aspects of the work can be found at the beginning of each chapter.

I.E.1 On the InAs/GaSb superlattice

The names superlattice and multilayer are generally used interchangeably, but to be precise, a superlattice refers to a multilayer with a longer crystalline

coherence than the chemical modulation distance in the layer stacking direction. The idea of the superlattice was initiated by Tsu and Esaki in late 1960s. [30, 31] At the beginning, two types of superlattices achieved by doping and compositional alternating were proposed. In the 1970's and 1980's, semiconductor and metal superlattices were first fabricated. [32, 33] Thereafter, many research results in this area were achieved. The study on InAs/GaSb and related III-V compound-based superlattices were first initiated by Sai-Halasz. [34]

Three types of band alignments, I, IIA and IIB, can be achieved for a semiconductor A/B superlattice formed by semiconductor A and B (when $E_{gB} > E_{gA}$). Figure I.2 shows the differences among these types. Due to quantum confinement by the different semiconductors which form the superlattice, the bands from bulk materials realign into a new series called mini-bands. Essentially, type I superlattices are defined as those in which the electrons in conduction mini-bands and holes in valence mini-bands are confined within layers A. Type IIA superlattices are those in which the electrons and the holes are confined to alternating layers. They are often named spatially "indirect" bandgap superlattices (There are different indirect semiconductors which have indirect bandgaps in momentum space). A type IIB superlattice has a similar distribution profile for the electrons and holes. In addition, the bottom of conduction band of bulk A overlaps the top of the valence band of bulk B. Then the band gap between mini-bands of type IIB is far narrower than that of type I and IIA superlattices. A type IIB superlattice is ideal for detecting infrared photons for this reason.

The superlattices which we study in Chapters II and III are type IIB InAs/GaSb superlattices. The bandgap in an InAs/GaSb superlattice can be modified by adjusting the widths of the InAs layers or GaSb layers. Due to their unusual band structures, the family of InAs/GaSb and related compound superlattices prove very attractive for their potential application as infrared sensors and other optoelectronic devices as proposed by Smith and Mailhiot, [35]. Recent advances in passivation and processing have enabled the fabrication of fully inte-

grated imagers operating in the midinfrared region with a performance comparable to those made with HgCdTe materials. [36, 37]

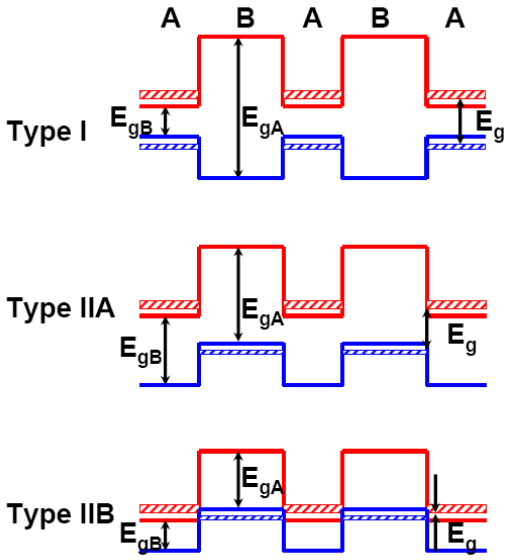

Figure I.2: Schematic diagrams of the arrangements of the bands in type I, IIA and IIB superlattices formed by two semiconductors A and B.

The x-ray diffraction characterization of superlattice systems dates back to the early years of superlattice study. [38] Several models for structural characterization were developed. [33, 39, 40, 41, 42, 43] But current x-ray diffraction studies on InAs/GaSb superlattice family usually focus on the modulation length, the average d-spacing of the superlattice and other phemonological observations. It is our purpose to show that powerful structural refinement methods enable us to extract quantitative information from the x-ray diffraction profiles which would otherwise be obtained by destructive methods such as TEM or STM cross-section imaging. The refinement study also suggests how the absence of certain orders of diffraction satellite peaks results from the inhomogeneous and asymmetric out-of-plane lattice strain profile. The line shape study will indicate the optimal thickness of the InSb-like interfacial layer for out-of-plane coherence; then the superlattice structure is also optimized. The x-ray diffraction study on the annealed InAs/GaSb superlattices will suggest a way to improve the superlattice structure *ex situ*. This

will help the fabricators to modify growth parameters for structural improvement.

I.E.2 On the OMBD phthalocyanine thin film

Phthalocyanine is derived from the Greek terms "naphtha" (rock oil) and "cyanine" (dark blue). A phthalocyanine is a macrocyclic compound having an alternating nitrogen atom-carbon atom ring structure (Figure I.3) which was reported in 1907 as an unknown by-product. [44, 45] The phthalocyanine family exhibits exceptional stability to alkalies, sulfuric acid and heat. In the 1930s to 1950s, several properties of phthalocyanines were investigated including x-ray spectra, polymorphism, magnetic properties, photoconductivity, and dielectric and semiconductor properties. The magnetic and semiconductor properties of phthalocyanine family are not particularly interesting, but, considering their thermal stability, phthalocyanines are ideal candidates for organic semiconductor thin film studies.

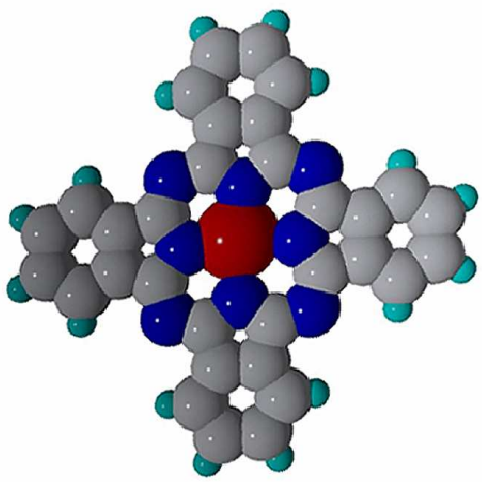

Figure I.3: The structure diagram of a phthalocyanine molecule. The center atom can be replaced with various metal atoms and ligands. In this graph, the red atom is the center atom; blue atoms are nitrogen atoms; grey atoms are carbon atoms; and cyan atoms are hydrogen atoms.

Phthalocyanines and some other organic materials appear in various crystalline forms due to different growth conditions or methods; this is called polymor-

phism. [46, 47, 48, 49] Unlike some other organic molecules which exhibit conformational polymorphism, the polymorphism of phthalocyanines is purely a consequence of different packings in the unit cells. The most common polymorphs of phthalocyanines are the α and β phases, [50, 51, 52, 53, 54, 55] which are formed by quasi-orthorhombic [56] and monoclinic [55] unit cells, respectively (Figures I.4(a) and I.4(b)). Besides the α and β phases, γ, δ, ϵ and X phases were also observed on rare occasions. [57, 58, 59, 60]

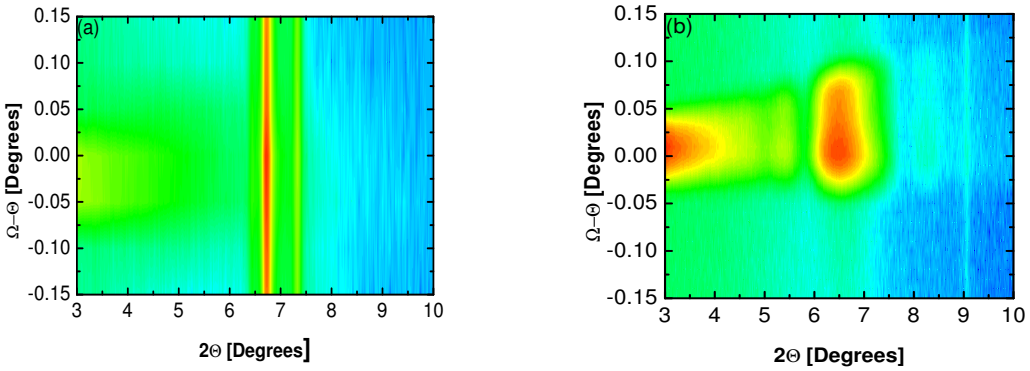

Figure I.4: XRD profiles for copper phthalocyanine (CuPc) films. (a) sublimated film and (b) OMBD grown film. The sublimated thin film usually has β structure and the OMBD film has α structure.

The phthalocyanine thin films are often grown using a sublimation method or a chemical method, such as Langmuir-Blodgett deposition. However, the films prepared using these methods are usually lacking well-defined layered structures. As an alternative to sublimation, modern vacuum technology facilitates the deposition of organic molecules layer by layer with the high reproducibility necessary for organic-on-inorganic heterostructures. Since the deposited organic thin films (e. g. phthalocyanine) do not follow the lattice structure of the substrate or buffer layer, the growth technique is named organic molecular beam deposition (OMBD) instead of organic molecular beam epitaxy (OMBE). Two-dimensional XRD results (Figures I.5(a) and I.5(b)) show that OMBD-grown phthalocyanine films have a narrower angular distribution of molecular layers than that of

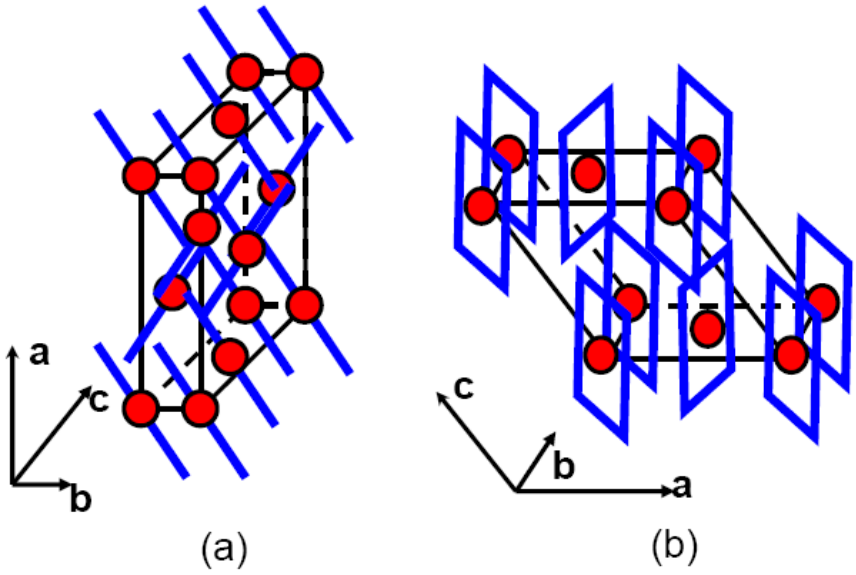

Figure I.5: The schematic diagrams of a phthalocyanine unit cell structure for (a) the α phase and (b) the β phase. The red circles represent the center atoms and the blue lines or blue planes are phthalocyanine rings.

the sublimated films. A comprehensive review of the OMBD technique and related topics was presented by Forrest. [61] The OMBD growth is governed by quasi-equilibrium stacking conditions. Particularly important is the competition between the adsorbate-adsorbate and adsorbate-substrate interactions as well as the growth temperature. "Layer-plus-islands" (Stranski-Krastanov) growth tends to be the most commonly observed mode in OMBD; in this case, the phthalocyanine thin films form layered structures with stepped rough surfaces. The OMBD molecular thin films are typically grown into structures determined by the substrate lattice rather than the bulk structure of the organic solid itself. We cannot take it for granted that the OMBD thin films form the very same structure as their macroscopic correspondence, so it is of significance to characterize the thin film structure using techniques such as surface analysis or diffraction experiments. Currently the transport of electrical carriers in organic thin films is believed to be strongly influenced by the thin film structure (e. g. anisotropy of the carrier

mobility); thus, understanding of the thin film structure important for practical purposes.

Surface morphology studies using TEM and AFM show that the size of the crystallites increases dramatically with increased deposition temperature. [62, 63, 64] It is reported that the surface morphology can be modified by *in situ* annealing or by varying the film thickness. [65, 66] An example AFM study on the surface morphology of the iron phthalocyanine (FePc) thin films is given in Figure I.6. The XRD method can be used to characterize phthalocyanine thin films. Other studies confirm that the phthalocyanine molecules are stacked into a herringbone structure so that a sharp diffraction peak at about 6.8° (and its higher order peaks) is present. [67, 68, 69, 70, 71] Theoretical models were proposed to explain the first diffraction peak and its Bragg oscillations for similar systems. [72, 73, 74] However, these models did not include the features of the phthalocyanine molecule and did not differentiate the different types of phthalocyanines. In this work, I propose a model to account for these deficiencies so that the contribution from the molecular structure is fully considered. The study will show that the molecular structure is crucial in understanding the XRD profiles of these thin films and that from the XRD profiles we also recover some information about the core electron density of the molecule and how the molecule is stacked. In previous studies, the bottom layer(s) adjacent to the substrate is (are) considered to have different stacking behavior from the upper layers. We will quantitatively show the limiting number of adjacent layers that can be described using our proposed one-dimensional model. Previous studies also address the angular distribution of the phthalocyanine crystallites with the OMBD thin film. It is generally believed that these crystallites are uniaxially aligned along the layer stacking direction. A three-dimensional model is proposed to simulate the uniaxial orientation behavior. We will try to determine how the lateral grain size and the orientation distribution affect the XRD diffraction results.

In brief, in the first part of the work, we deliver our study based on

the refinement using an existing procedure, and in the second part, we propose new models to hurdle those problems which have been overlooked or minimally addressed.

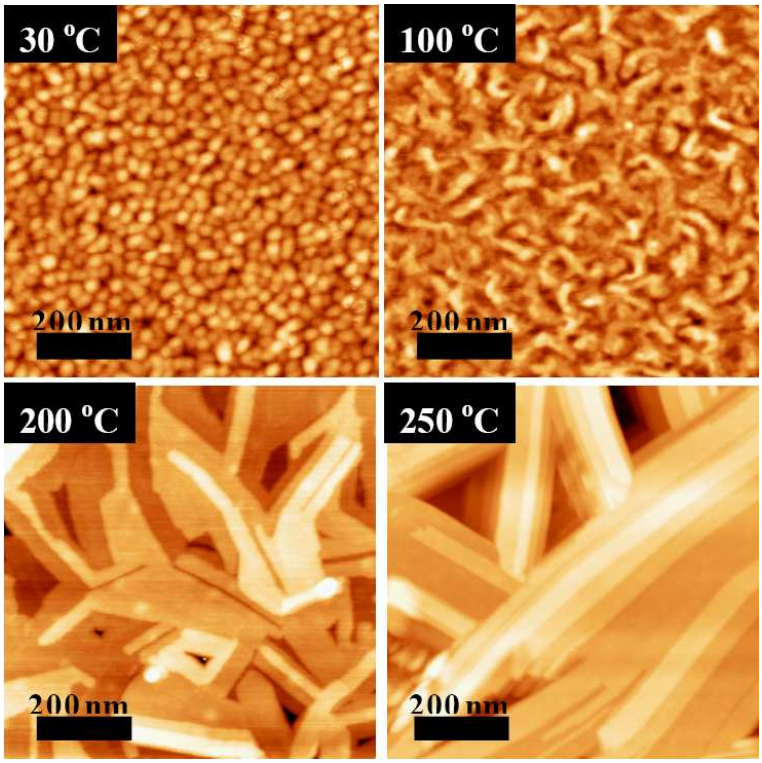

Figure I.6: Surface morphology of iron phthalocyanine (FePc) grown at different temperatures taken by AFM.

II

X-ray diffraction of InAs/GaSb superlattices with InSb-like interface

The material research and device design of high performance infrared detectors or lasers based on III-V semiconductor superlattices (SL) has received significant attention in recent years. InAs/GaSb binary-binary type-II superlattices, which were proposed nearly 20 years ago, [35, 75] are becoming a competitive alternative to silicon based or II-VI alloy based devices. Highly promising aspects of InAs/GaSb based devices include tunable band gaps, direct band transition and reduced Auger recombination noise. Comprehensive photoresponse studies of the InAs/GaSb SL band gap were carried out by several groups [76, 77, 78] and the relevant theoretical analysis was also presented in several papers. [79, 80] Previous studies show that the InAs/GaSb structure has a dominant effect on the band gap and photoresponse efficiency. [80, 81] Thus it is important to understand the way in which the superlattice structure influences its physical properties. Local surface and cross-section morphology have been studied by TEM, AFM and STM. Structure parameters such as the capping surface, buffer layer, and substrate roughness, and interlayer defect replication can be well studied with these methods. [81, 82, 83]

Raman spectroscopy offers an alternative for the determination of chemical composition and bonding configuration, making it a major tool to understand the interfacial behavior of superlattices. [84] X-ray diffractometry (XRD) is a direct structural method useful for the determination of the global superlattice structure. Analysis of Ω-$\Theta/2\Theta$ (Ω-dependent $\Theta/2\Theta$ curves or 2D scan) scans gives information along the layer-stacking z-direction as well as the parallel xy-direction. The modulation length (periodicity), the average out-of-plane interplanar spacings of bilayers, and the total thickness of InAs/GaSb superlattices can be readily obtained from typical XRD. However, further structure analysis requires the application of a structural "refinement" procedure such as SUPREX, [40, 33, 39, 41] based on nonlinear optimization of structural models. In this chapter, we apply SUPREX to InAs/GaSb superlattice samples, and examine the validity of models with different strain profiles. We discuss the relevance of interfacial layers on the strain and the coherence using our refinement results.

II.A Experiment and fitting procedure

The InAs/GaSb superlattices were fabricated by molecular beam epitaxy from elemental Ga and In, and valved cracker cells for As and Sb. The GaSb buffer layers were grown on Te-doped (100) GaSb substrates at a temperature of 500 °C. The growth temperature was then lowered to 400±5 °C for the SL layer growth. After SL growth, a 15-minute *in-situ* annealing at 450 °C under Sb-overpressure was applied for the improvement of layer quality. The InSb-like interfacial layers were inserted between the main constituent layers of the SLs to modulate the SL strain to reach stress balance. The InSb-like interfacial layers were prepared by controlling the MBE shutter sequence. [85] All superlattices were grown with the same number of 20 periods.

X-ray diffraction data was acquired using two 1/6° slits to collimate the incident x-ray beam and two 0.3 mm wide slits on the outgoing beam to achieve

Table II.1: Parameters for all of the samples studied in this chapter. All thickness values are given as expected from the growth process (L_{IF} is the Interfacial layer thickness; 1, 2 refer to the interface between InAs and GaSb, and GaSb and InAs, respectively. L_{GaSb}, L_{InAs} and L_{BUF} are the GaSb, InAs and GaSb-buffer layer thicknesses, respectively).

Sample Number	Wafer Type	L_{BUF} [Å]	L_{InAs} [Å]	$L_{IF}1$ [Å]	L_{GaSb} [Å]	$L_{IF}2$ [Å]	# of bilayers
1	GaSb (001)	10000	0	0	0	0	N/A
2	GaSb (001)	10000	49	0	40	0	20
3	GaSb (001)	10000	49	2.85	40	2.85	20
4	GaSb (001)	10000	49	3.42	40	3.42	20
5	GaSb (001)	10000	49	3.99	40	3.99	20
6	GaSb (001)	10000	49	5.13	40	5.13	20

higher momentum resolution. The Cu x-rays were not monochromized, so that for sufficiently narrow intrinsic diffraction peaks the $CuK_{\alpha 1}/CuK_{\alpha 2}$ doublet was resolved. The setup allows selection of several acquisition modes, including $\Theta/2\Theta$, Ω and Ω-$\Theta/2\Theta$ (Ω-dependent $\Theta/2\Theta$ curves or two-dimension (2D) scan) modes. The various angles of the x-ray diffraction experimental setup are defined in Figure II.1. The superlattices were aligned with the z-direction parallel to the x-ray momentum transfer.

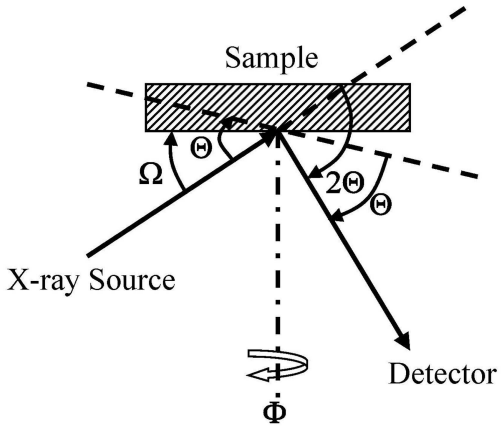

Figure II.1: Definition of the angles in the x-ray diffraction experiment.

The full $\Theta/2\Theta$ scans of our samples can be divided into (000), (002), (004) and (006) ranges. Figure II.2 shows $\Theta/2\Theta$ scans of the (004) range of the six samples studied in this chapter. From the bottom to the top they are labeled from 1 to 6, respectively, and are described in Table II.1. The data sets around the main diffraction peaks for the different ranges are simulated and analyzed using the SUPREX refinement package. [33, 39, 41] Because the particular method of preparation of the interfacial layers is expected to result in a continuous chemical transitional layer we approximate it as an interdiffusion profile in our model. Thus the approach to structural refinement employs a bilayered superlattice model which includes a strain profile along the z-direction. The details of the models and our refinement approach are detailed in Appendix B.

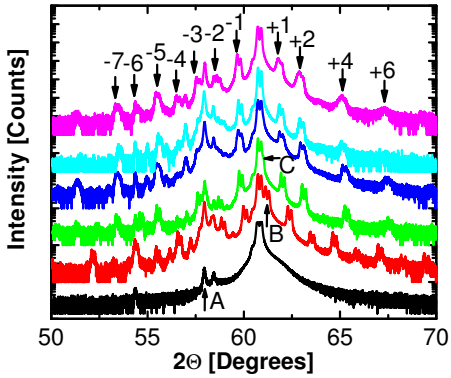

Figure II.2: $\Theta - 2\Theta$ coupled XRD results of (004) curves for a series of samples. From bottom to top, these curves are from the samples listed in Table II.1. Note the absence of some of the odd order peaks on the right hand side of the central peak.

II.B Experimental and fitting results

II.B.1 General observation and model selection

The thickness variations of the transitional InSb-like layer (treated as interdiffusion in our refinement) cause systematic changes in the XRD spectra of

the superlattices (Figure II.2). In the sample with an intended abrupt interface (i.e. without an interfacial layer; second curve from the bottom), the 0^{th} order superlattice peaks are well separated from the GaSb buffer. This indicates that the average d-spacing of the superlattice differs significantly from that of the GaSb bulk (Arrow B in Figure II.2). As the thickness of the InSb-like interfacial layer is increased, the 0^{th} order (central) superlattice peaks move closer to the GaSb peaks (Arrow C in Figure II.2), as has been observed before. [81, 84]

In general, differences in bulk chemical, structural and mechanical properties of constituent layers forming a superlattice may cause strain. This directly influences the position of the 0^{th} order peaks and the average d-spacings of the InAs and GaSb constituents. Models with different out-of-plane strain profiles that can be conceived include: A) Uniformly strained InAs and GaSb constituent layers; B) Unevenly strained constituent layers - the center parts of the layers are less strained with d-spacings approaching that of the bulk materials, and the boundary parts are more strained in order to balance stress across the layer boundary. Furthermore, the two boundaries at the bottom and at the top of each constituent layer are strained asymmetrically. [41, 86]

To understand the impact of these different strain models on the refinement, we tried both models on our experimental data. We found that the quality of fit (smaller values of χ^2) is significantly better when using the inhomogeneous and asymmetric strain model. Consequently, the discussion below focuses mainly on this model.

Among the (000), (002), (004) and (006) diffraction series, the (000) diffraction does not readily provide atomic scale information such as the d-spacing and the number of atomic layers. The (006) XRD series is superior to the remaining two in angular resolution but has less intensity resulting in a poor signal to noise ratio. Although the (002) series yields approximately the same intensity as the (004) series, it does not provide the same high angular resolution as the (004) series. Weighing all factors, we focus most attention on the (004) series. Figure II.3(a)

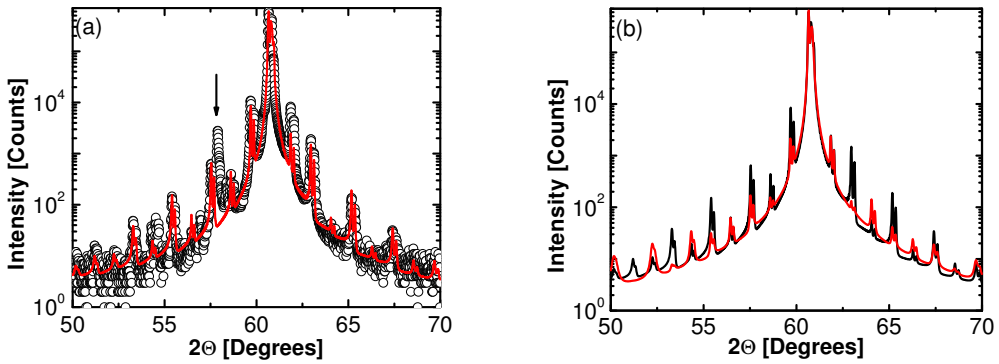

Figure II.3: (a) $\Theta - 2\Theta$ scanning results in the (004) range of sample # 3. The black circles are experimental data and the solid curve is fitted. The fit reproduces the experimental data very well except in the area denoted by an arrow; this peak is caused by the GaSb buffer layer. (b) Comparison of refinement results for sample # 3 using the two strain models: The red curve is obtained using the homogeneous and symmetric strain model; the black curve is obtained using the inhomogeneous and asymmetric strain model. Note that the latter reproduces the absence of $+3^{rd}$, $+5^{th}$, and $+7^{th}$ order peaks.

shows an example of a (004) refinement and experimental data, demonstrating the high quality refinement that can be achieved. In Figure II.3(b), refinement results from the homogeneous and symmetric model and from the inhomogeneous and asymmetric model are compared. Note that the refinement results from the latter model more closely match the experimental data, reproducing the absence of $+3^{rd}$, $+5^{th}$ and $+7^{th}$ order peaks.

II.B.2 Experimental and refinement results

The superlattice periodicity can be obtained in a straightforward way from a linear fit based on Bragg's Law. [41] In Figure II.4(a), the values obtained by this technique (Λ_1, x-axis) are plotted against the values obtained using our inhomogeneous and asymmetric strain refinement model (Λ_2, y-axis). As the figure shows, Λ_1 and Λ_2 have very high correlation. Based on Bragg's Law, the average

d-spacing of superlattices is given by:

$$\langle d \rangle = \frac{N_{InAs} d_{InAs} + N_{GaSb} d_{GaSb}}{N_{InAs} + N_{GaSb}} \tag{II.1}$$

Figure II.4(b) shows that there is also a high correlation between the d-spacing values from Bragg's Law ($\langle d \rangle_1$) and the values from our inhomogeneous and asymmetric strain refinement model ($\langle d \rangle_2$). Figure II.5 displays the change in the average d-spacings of the superlattices as a function of the InSb-like interfacial layer thickness.

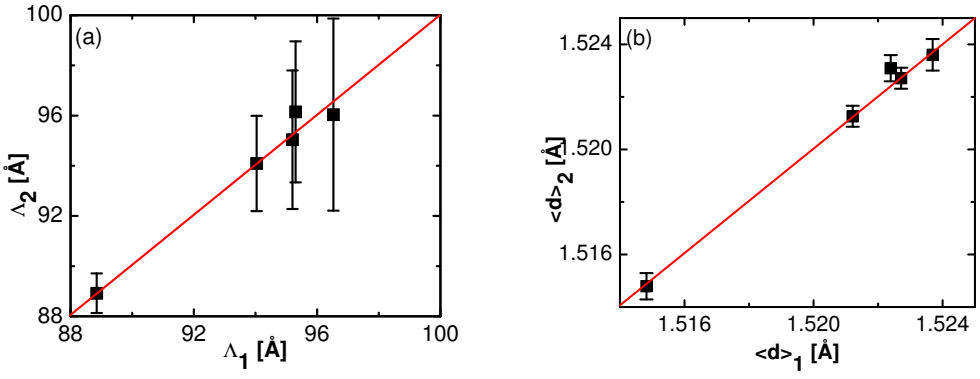

Figure II.4: (a) Correlation of periodicity Λ derived from Bragg's Law (Λ_1) and from our inhomogeneous and asymmetric strain refinement model (Λ_2). The error bars are determined by discrete roughness as defined by Fullerton *et al.* [41] (b) Correlation of average d-spacing of the superlattices between the values from Bragg's Law ($\langle d \rangle_1$) and the values from our inhomogeneous and asymmetric strain refinement model ($\langle d \rangle_2$).

Figures II.4(a), II.4(b) and II.5 prove that SUPREX refinement based on the asymmetric inhomogeneous model is in good quantitative agreement with values calculated earlier by standard methods. [78, 84, 41]

However, the complete characterization of a superlattice structure requires determination of additional parameters which may also affect the physical properties. Beside the overall periodicity and average d-spacing, detailed information of each constituent layer is essential to understand the superlattice band structure which determines physical properties such as the photoresponse

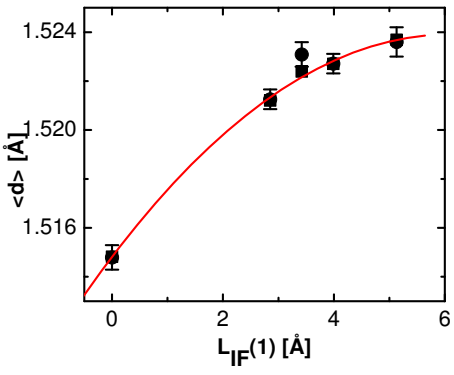

Figure II.5: Average d-spacing of the superlattice ($\langle d \rangle$) vs. nominal interfacial layer thickness ($L_{IF}(1)$). The squares represent values from Bragg's Law; the circles represent values from the inhomogeneous and asymmetric strain refinement model.

and transport. These additional parameters cannot be obtained simply from the experimental data and this issue has not been satisfactorily discussed in previous studies. [81, 84] The SUPREX refinement reproduces real x-ray diffraction data including contributions from samples and apparatus. The refinement procedure automatically adjusts fitting parameters to lead to a minimized deviation of the refined curve from the XRD profile. The full experimental curve provides a strict limitation on the refined parameters. This constraint assures that detailed structural parameters of the individual constituent layers are obtained thus providing a complete structural picture. Most other approaches do not use information from the full data set. [76, 84] Instead, they focus on the position and intensity of the diffraction peaks. It is important to realize that structural information resides in the full spectrum including peak shoulders and absence of diffraction peaks, commonly ignored. Thus SUPREX extracts structural parameters using the full spectrum rather than selected intensities.

Figure II.6(a) gives the thickness derived from the SUPREX refinement of the InAs and GaSb constituent layers. Comparing to Table II.1, we find that the values agree well with those anticipated from the growth process. The average

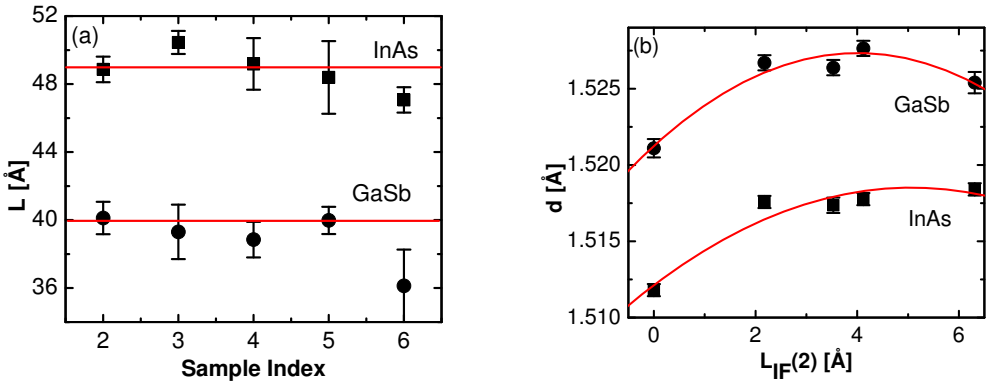

Figure II.6: (a) Thickness of individual SL layers (L) vs. sample number. The squares and the circles indicate the thickness of the InAs and GaSb constituent layers from refinement, respectively. (b) Refinement average d-spacing of constituent layers (d) vs. refinement thickness of interfacial layer ($L_{IF}(2)$). The squares are values for the InAs layer and circles are values for the GaSb layer.

d-spacing of the constituent InAs and GaSb layers vary with the different InSb-like interfacial layers, as demonstrated in Figure II.6(b). Without the InSb-like interfacial layer, both InAs and GaSb layers are slightly compressively strained in the z-direction. The InAs lattice exhibits tensile strain in the in-plane direction to match the GaSb buffer lattice, causing compressive strain along the interplanar direction due to the Poisson effect. [87] Figure II.7 illustrates the mechanism of this compressive strain. Misfit dislocations will form to relieve in-plane strain if the InAs layer thickness is beyond 2000 Å, which is far thicker than our samples. [88] In our studies, an InSb-like interfacial layer of 2.85 Å nominal thickness, significantly decreases the separation between the 0^{th} order (or center) peaks (Figure II.2: Arrows B and C) of the superlattice and that of the GaSb buffer layer. Thicker InSb-like interfacial layers behave similar to the 2.85 Å thick layer; however, a nominal 5.13 Å thick InSb-like interfacial layer appears to slightly overcompensate the lattice mismatch between the InAs and GaSb layers. An optimal superlattice structure can be achieved by controlling the thickness of the InSb-like interfacial layers. A structure with larger d-spacing such as the InSb-like interfacial

layers may alleviate the d-spacing "deficit" and relieve the vertical strain. However, thick InSb-like interfacial layers with a considerably larger d-spacing than those of the InAs and GaSb layers make superlattice heteroepitaxy unfavorable. A similar qualitative conclusion has been mentioned in a previous study, [84] but no quantitative results related to the thickness of the InSb-like interfacial layers were given.

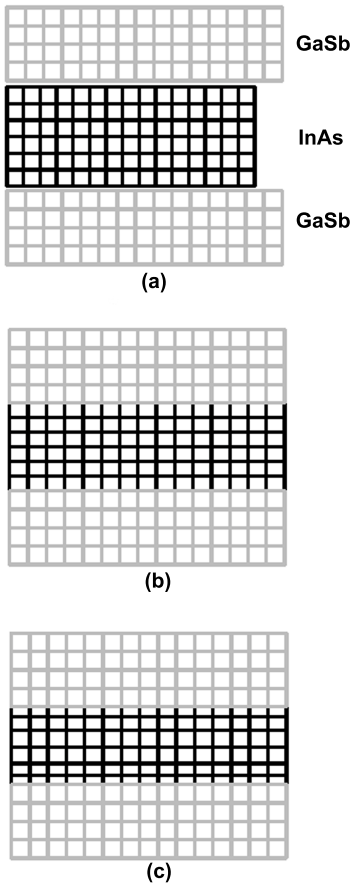

Figure II.7: Schematic diagrams illustrating how interplanar strain occurs in a lattice matched epitaxial SL. (a) The bulk d-spacing of InAs is slightly smaller than that of GaSb. In a lattice matched epitaxial SL, the in-plane d-spacing of InAs is increased to match that of GaSb, causing a d-spacing compression in the out-of-plane direction. This d-spacing compression is shown for the homogeneous and symmetric strain model (b) and the inhomogeneous and asymmetric strain model (c).

The SUPREX derived continuous roughness of all superlattice samples is

less than 0.06 Å, which can be ignored. The discrete roughness (which is discussed in the very general sense in Appendix C) of InAs and GaSb layers varies from 0.7 Å to 1.4 Å and 0.6 Å to 1.7 Å, respectively. Our SUPREX refinement determined that samples with a thick interfacial layer have a greater amount of discrete roughness than samples with an abrupt interfacial layer. However, a convincing quantitative relation between the discrete roughness and the interfacial layer thickness of all samples is unavailable. The thickness of the InSb-like interfacial layers from our SUPREX refinement is given in Figure II.8(a) and these values are also close to those expected from the growth process.

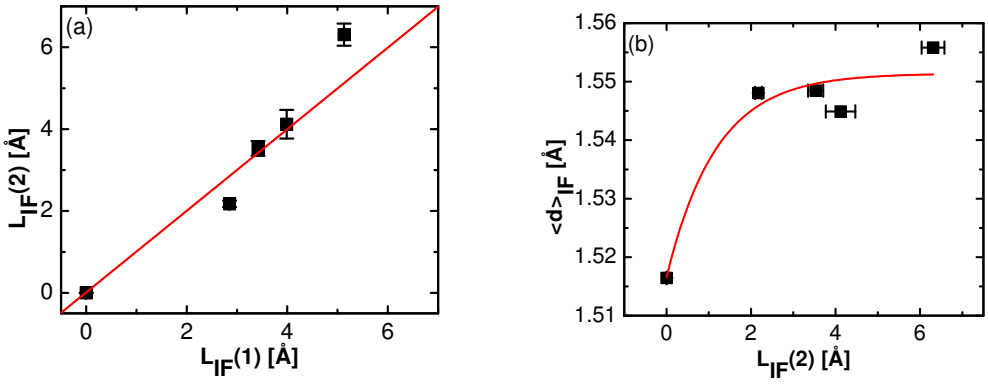

Figure II.8: (a) Correlation between the thickness of the InSb-like interfacial layer from refinement using the inhomogeneous and asymmetric strain model ($L_{IF}(2)$) and the nominal thickness of the InSb-like interfacial layer ($L_{IF}(1)$). Due to the limitations of our current model, these values can only approximately reflect the actual thickness. (b) The refinement values for the average d-spacing of interfacial layers ($\langle d \rangle_{IF}$) vs. the thickness of interfacial layers ($L_{IF}(2)$).

The lattice constant and the electron density of the interdiffusion region depend on the parameters of the InAs and GaSb layers. Our approach cannot give detailed chemical composition information of the interfacial layers. The only structural information we can derive about this region is the local d-spacing, which is determined by the strain profile across the layer boundary. The local d-spacing in the interdiffusion layer can shed some light on its chemical composition. Note

that the binary compounds of In, As, Ga and Sb can be InAs, InSb, GaAs and GaSb. InAs and GaSb have very similar interplanar d-spacing and electron density, while InSb and GaAs have the largest and smallest d-spacing, respectively. If the average d-spacing in the interdiffusion layer is larger than those of InAs and GaSb, we suggest that the corresponding interfacial layer is InSb-like. If the refinement shows a smaller d-spacing, the chemical composition is possibly GaAs-like. Figure II.8(b) shows the refinement average d-spacing in the interdiffusion region for the samples listed in Table II.1. The average d-spacing for all samples containing an interfacial layer are larger than those of InAs and GaSb, consistent with the assumption that the interface layers are InSb-like. The InAs and GaSb constituent layers have very small x-ray diffraction contrasts because of the similar lattice constant and electron density (scattering factor). The InSb-like interfacial layer, modeled as interdiffusion, is also difficult to differentiate from the remainder of the superlattice. The interdiffusion-related parameters are very sensitively correlated with other structural parameters, which makes it difficult to achieve achieving a stable refinement. We initially fix the interdiffusion parameters in the fitting process and allow the other parameters to achieve stable values. Finally, we release the confinement to interdiffusion and let these parameters vary freely. Following this strategy, we are able to avoid unphysical fits.

II.B.3 Absence of odd order peaks

Figure II.2 shows that the satellite peaks of order $+3^{rd}$, $+5^{th}$ and $+7^{th}$ are absent for samples No. 3, 4, 5 and 6, while the $+1^{st}$ order peak is present. Under special circumstances, lateral compositional modulation (LCM) [82, 83] can cause this effect. To investigate this further, we performed Ω-$\Theta/2\Theta$ 2D x-ray scans which give in-plane structural information. Our data shows that at different Φ angles, no diffraction intensity modulation exists along the Ω direction (Figure II.9), which would be expected for samples with LCM. This strongly suggests that the absence of peaks in the samples is unrelated to LCM. We found, however, that we can

reproduce the experimental spectra by including inhomogeneous, asymmetrical strain into the refinement model. Summarizing all of our refinement results, we find that a uniformly strained model results in fits with error as low as about 7%, while the inhomogeneous, asymmetrical strain model reduces the error to about 4%. In addition, the inhomogeneous, asymmetrical strain model simulates well the absence of $+3^{rd}$, $+5^{th}$ and $+7^{th}$ order peaks, beyond the ability of the uniformly strained model. This implies that our superlattices are inhomogeneous and asymmetrically strained.

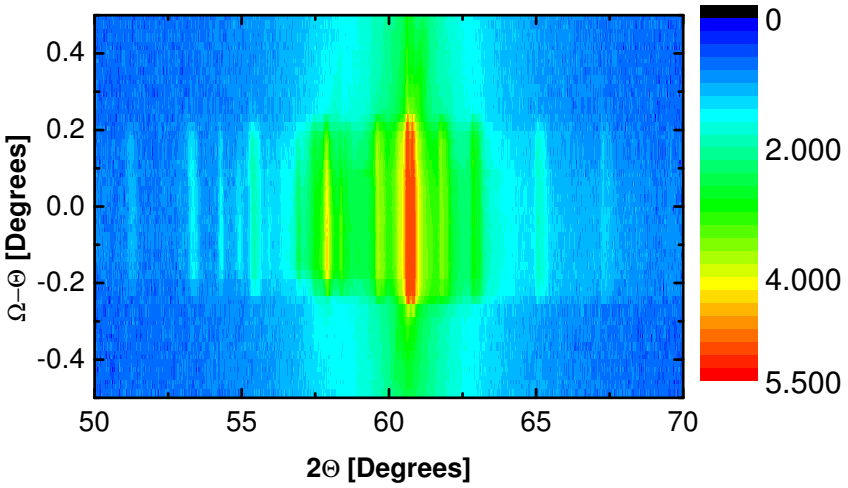

Figure II.9: Two-dimensional $\Omega - \Theta/2\Theta$ scan in the (004) range for sample number # 3. The different colors indicate the XRD intensity on a logarithmic scale.

II.B.4 Structural coherence length

Herres *et al.* [84] discussed a method to determine the x-ray coherence (grain size) length along the normal and tangential direction of InAs/GaSb superlattices on GaAs substrates. The 0^{th} order (SL center) peaks for these samples do not overlap with the GaAs (004) peaks, which allows for measurement of the 0^{th} order satellite peak FWHM directly from raw x-ray data. However, our InAs/GaSb

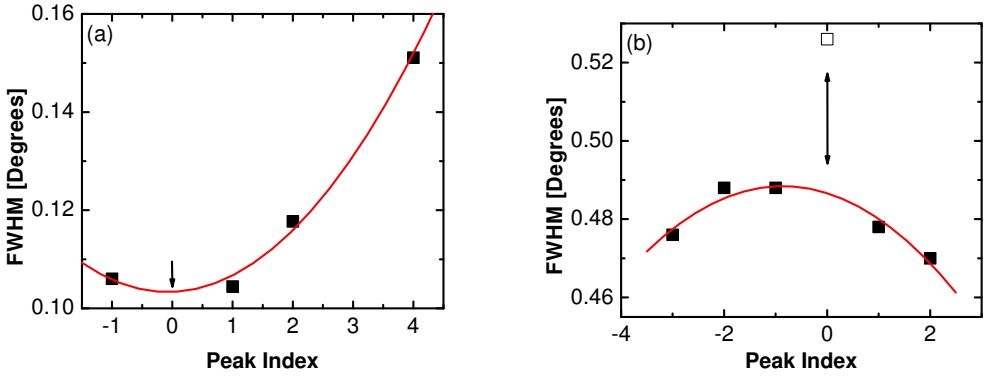

Figure II.10: (a) FWHM of higher order satellite peaks of one superlattice vs. their order ($\Theta - 2\Theta$ coupled scan). (b) FWHM of higher order satellite peaks of the superlattice vs. their order (Ω-Θ coupled scan). The solid lines are polynomial fits to the data which help determine the FWHM of the 0^{th} order peaks. The solid squares indicate the FWHM of higher order satellite peaks and the empty square indicates the FWHM of the GaSb buffer layer peak.

superlattices are grown on GaSb substrates and the 0^{th} order peaks are always very close to the GaSb (004) peaks, complicating the determination of the 0^{th} order satellite peak FWHM. Although HRXRD may improve the angular resolution significantly, this peak overlap problem is still not entirely solved. We have developed a new technique to derive the 0^{th} order peak FWHM from higher order satellite peaks. The details of this technique are given in the Appendix D. Figure II.10(a) shows the FWHM of higher order satellite peaks of a given sample, which may be easily obtained from a $\Theta/2\Theta$ scan. The 0^{th} order peak FWHM (indicated by arrows in Figures II.10(a) and II.10(b)) is obtained from a second order polynomial fit to the data. All 0^{th} order peaks FWHM of the (002), (004) and (006) series can be restored by this method. A similar analysis can be performed on the Ω-Θ data (rocking curve). The solid squares in Figure II.10(b) represent the FWHM of high order peaks from Ω-Θ data and the hollow square represents the FWHM of the GaSb buffer peak. The coherence length in the normal direction is calculated and plotted against the thickness of the InSb-like interfacial layer in Figure II.11. When the superlattice has an InSb-like interfacial layer of about 2.2 Å thick, the

superlattice is found to have the longest coherence length (largest grain size in the normal direction). When the thickness of the InSb-like interfacial layers is greater than about 5 Å, the coherence length in the z-direction drops significantly. We did not find any relationship between the thickness of the InSb-like interfacial layers and the coherence length in the xy-direction.

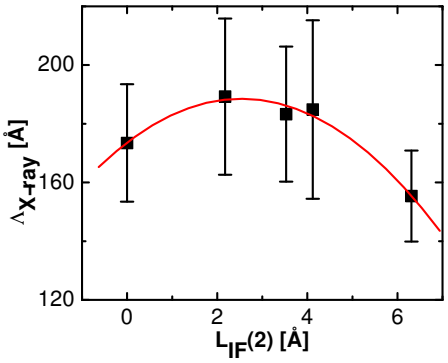

Figure II.11: Structural coherence length (Λ_{X-ray}) in the z-direction (obtained from grain size calculations [84] based on the FWHM of the 0^{th} order peaks) vs. refinement thickness of interfacial layers ($L_{IF}(2)$).

II.C Conclusion

The average d-spacing of InAs/GaSb superlattices increases with insertion of InSb-like interfacial layers between the InAs and GaSb. SUPREX refinement reveals that an InSb-like interfacial layer of nominal thickness ≥ 2.85 Å compensates the lattice mismatch between InAs and GaSb layers. The average d-spacings of individual InAs and GaSb constituent layers are nearly constant as a function of the thickness of the interfacial layer as long as its thickness is greater than 2.85 Å. The SUPREX method provides not only the average d-spacing but also the thickness of individual InAs and GaSb layers with high accuracy. The thickness of the interfacial layers can also be estimated and the refined values for the local d-spacing across the InAs and GaSb boundary support the assumption

that the interfacial layers are InSb-like. The thicknesses of individual InAs, GaSb and interfacial layers derived with SUPREX are well correlated with nominal values expected from the growth process.

In conclusion, we have used the SUPREX structural refinement method to obtain lattice parameters, roughnesses and strain profiles in InAs/GaSb superlattices.

The structural coherence length or grain size was obtained from the 0^{th} order superlattice peak FWHM even for samples where this peak is not resolved. Superlattices with mismatch-compensated lattices have longer coherence lengths, but over-compensation greatly reduces the coherence.

2D XRD results exclude the possibility that a lateral compositional modulation causes the absence of odd order satellite peaks in these types of superlattices. SUPREX refinement proves that a model with an inhomogeneous and asymmetric strain profile in the z-direction can reasonably describe the details of the full XRD data.

II.D Acknowledgement

This work was supported by AFOSR MURI # F49620-02-1-0288.

III

Study on annealed InAs/GaSb superlattice

The structural quality mentioned in Chapter II can be tuned not only by interfacial insertion, but also by optimization of the deposition parameters and by post-growth thermal processing (annealing). Bennett [89] found that both the growth temperature and the molecule composition of the gas sources can impact the structure of GaSb/GaAs, InSb/InAs, AlSb/AlAs and InAs/InSb superlattices. Xu *et al.* [90] showed that annealing at various temperatures allows for modification of the structural properties of InAs/AlSb SLs. Furthermore, Xu and Bennett also noticed pronounced structure degradation and significant strain relaxation. There is evidence that annealing causes interfacial atomic segregation and intermixing for several types of III-V binary superlattices. [86, 91, 92] It is generally believed that the superlattice of InAs/GaSb and its ternary variations may be improved by inserting an antimony-soaked interfacial layer to avoiding Ga-As bonding. Rapid *in situ* thermal annealing may also work to prevent Ga-As bonding. [93, 94] However, due to technical issues, it is difficult to anneal *in situ* a series of samples deposited under identical circumstances. And it is also difficult to grow *in situ* a series of superlattices at different temperatures on a single wafer. It is important to understand how the *ex situ* annealing affects the InAs/GaSb superlattices in

controlled experiments. Such a study will be helpful in optimizing the growth parameters of the family of InAs/GaSb and related superlattices. By examining the XRD profiles of these annealed superlattices, we can also understand the dynamics of structure transformations at different temperatures.

III.A Sample preparation and the annealing process

The InAs/GaSb superlattices with the intended structure (InAs 20.5 Å)$_{90}$ / (GaSb 24 Å)$_{90}$ (InAs layer 20.5 Å thick, GaSb layer 24 Å thick and the number of bilayers is 90) which is illustrated in Figure III.1, are deposited on 1-inch wafers using MBE fabrication procedures similar to those mentioned in Chapter II. Thin Sb-soaked interfaces of about 1.2 monolayers thick are inserted between InAs and GaSb layers to avoid Ga-As bonding.

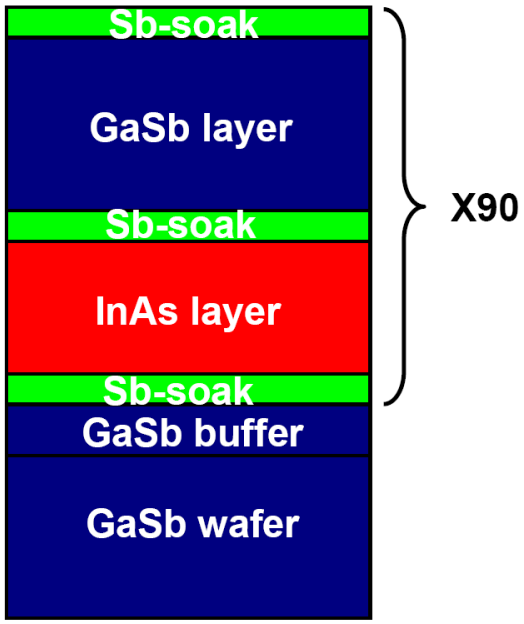

Figure III.1: A schematic diagram of the intended structure of the initial InAs/GaSb superlattice grown on a 1-inch GaSb wafer.

Next, the samples are cut into pieces and annealed at 200 °C, 300 °C,

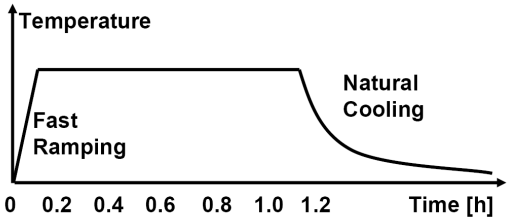

Figure III.2: A schematic diagram of the annealing procedure.

350 °C, 400 °C, 425 °C, 450 °C and 500 °C for one hour in HVAC to study how the annealing temperature modifies the structure. Some other pieces are annealed for 0.5 hour, 1 hour, 4 hours, 8 hours and 16 hours at 200 °C and 400 °C to study the time-dependence structural evolution. The annealing shown in Figure III.2 is a three-step procedure: 1) Ramp up the annealing temperature to the target value at the fastest rate; 2) Keep the furnace at a constant temperature for given period of time; 3) Let the system cool down bye removing the heat source. The annealing time has a half hour uncentainty from the thermal lag of the furnace.

III.B Surface morphology

The annealed samples were cleaned using methanol and isopropanol. Then the surface morphology was studied for patterns using atomic force microscope (AFM) at small scale and optical microscope at large scale. Figures III.3(a)-III.3(h) show the AFM and optical microsocopy images for the samples annealed at different temperatures for the same annealing time (1 hour). The surface of the sample without annealing (Figure III.3(a)) shows no trace of roughness so that it is believed to have an atomically flat surface. The sample annealed at 200 °C displays impurities adsorbed to the surface, but the dark part, which represents the surface of the superlattice, is still flat. Larger impurity adsorption occurred on top of the sample annealed at 300 °C. We notice that the surface shows some roughness under the adsorption sites. A porous surface, indicative of lateral instability, is observed for the sample annealed at 350 °C. Such lateral instability is caused

either by mild sublimation of the top layer or the relaxation of the in-plane strain. The annealing at 400 °C shows very strong nucleation at the surface indicating that the thermal fluctuations tend to deform the epitaxially grown quasi-stable layered structure in order to minimize the total free energy. The dimensions of the patterns of Figure 3.3(f)-3.3(h) are too large to be observed using AFM. The pebbles formed at 400 °C reorganize along parallel lines at 425 °C to form a so-called stripe-like structure. Two consecutive lines are about 5 μm apart. Annealing at a higher temperature completely eliminates the stripes and encourages macroscopic patterns to form. In fact, we notice that strong sublimation occurs when we anneal samples at temperatures above 450 °C.

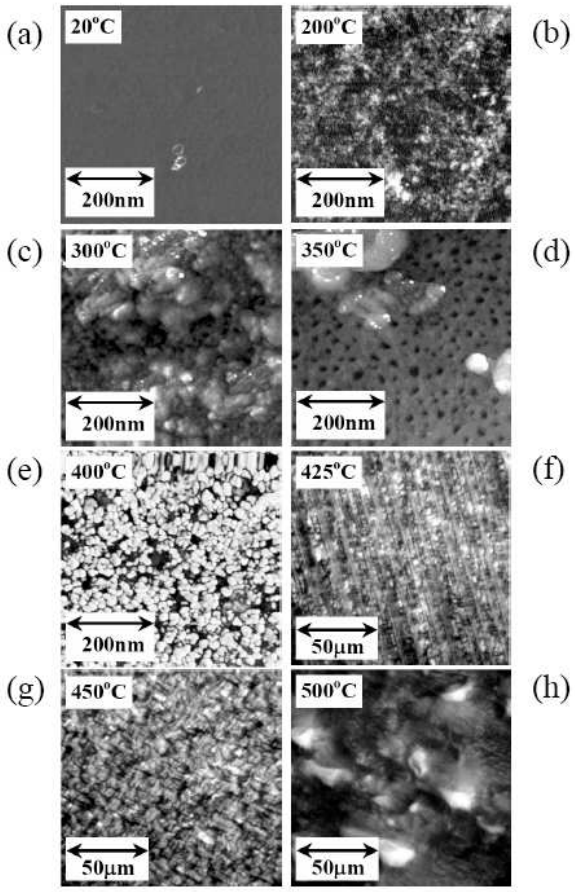

Figure III.3: The AFM images (a)-(e) and the optical microscope images (f)-(h) of the surfaces of the InAs/GaSb superlattices annealed at different temperatures.

III.C Temperature-dependent XRD result

In addition to the AFM study of the surface morphology, we recorded the XRD profiles of these samples. Although these pieces were cut from the same sample so that the initial XRD profiles are identical, the XRD profiles for the samples undergoing the annealing process appear very different. Figure III.4 shows the XRD profiles in a single graph. Different profiles are displaced vertically for clarity. From the bottom to the top, the lines refer to the profiles at RT, 200 °C, 300 °C, 350 °C, 400 °C, 425 °C, 450 °C and 500 °C in sequence. The profile for RT occasion shows the absence of -4^{th}, -3^{rd}, and -2^{nd} order satellite peaks. The samples annealed at 200 °C and 300 °C show more satellite peaks in the low angle range. Therefore, a better long-range order is achieved in these samples than in the sample without annealing. The -4^{th} order satellite peak disappears in the sample annealed at 350 °C. When the annealing temperature is increased, more high order satellite peaks vanish. For instance, at 400 °C, we can still find -1^{st}, $+1^{st}$ and $+2^{nd}$ order satellite peaks, but at 425 °C, we can only observe the -1^{st} order satellite peak. When the annealing temperature is above 450 °C, all satellite peaks are eliminated. The successive disappearance of satellite peaks indicates that the out-of-plane long-range order or the interlayer correlation in those superlattices is gradually destroyed and finally entirely removed when the annealing temperature goes up to above 450 °C for 1 hour period of time. Therefore judging by how many satellite peaks show in the XRD profiles, we can understand qualitatively how the structure of these superlattices evolve as the annealing temperature varies. Besides the difference in the population of the satellite peaks, we also notice that the sample without annealing has a broad background bump in the range between -2^{nd} and -1^{st} order satellite peaks, highlighted by the red circle in Figure III.4. This background suggests the probable existence of unintended crystalline structure with d-spacing longer than those of the InAs and GaSb constituent layers. Comparing this d-spacing with those of some common III-V InAsGaSb based bi-

nary compounds, we postulate that the background is directly related to In-Sb bondings within the superlattice. The black circle indicates a background structure with a shorter d-spacing in the superlattices annealed in the temperature range from 400°C to 425°C. This shorter d-spacing coincides with the d-spacing from a Ga-As type bonding structure. As we did not intend to deposit the superlattices with Ga-As bonding at the interfaces, the background is not caused by the intended structures, but related to Ga-As bonding. This issue is addressed in a later section.

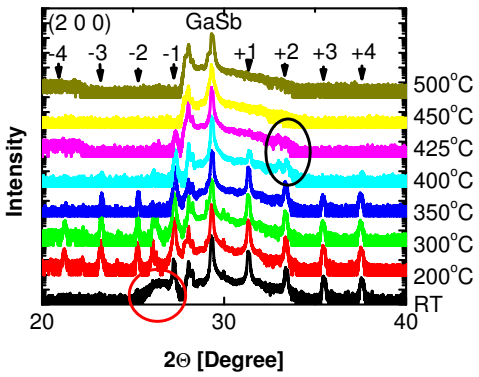

Figure III.4: The XRD profiles for the series of the annealed InAs/GaSb superlattices in the temperature range from RT to 500 °C. The curves are shifted vertically for clarity.

Further investigation into the annealed InAs/GaSb superlattices by focusing on the center area of the XRD profiles shows that the satellite peaks of the superlattices experience peak-drifting from the low angle side to the high angle side. Figures III.5(a) and III.5(b) show how the -1^{st} and $+1^{st}$ order satellite peaks drift in the (200) order diffraction range and how the 0^{th} order satellite peak drift in the (400) order diffraction range. At lower annealing temperatures or without annealing, the 0^{th} order satellite peak sits to the left of the GaSb substrate peak (indicated by the straight line). As the annealing temperature is increased, the satellite peak shifts to the right. Figure III.6 shows the shortening of the average d-spacing of the superlattices as the annealing temperature varies. Note that

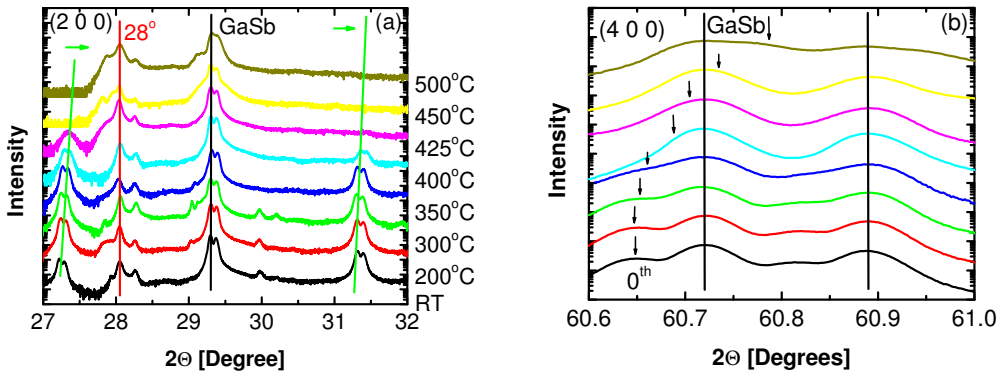

Figure III.5: (a) Center area of the XRD profiles in the (200) range and (b) in the (400) range. The substrate peaks are marked with black lines and the annealing temperatures are given in Figure III.5(a). From bottom to top, the first four peaks (indicated by arrows) are interpolated from the higher order satellite peaks, and the rest peaks are derived using double-Guassian-peak fitting. Due to the limitations of the data, only approximate values (large uncertainty) can be obtained for the top four 0^{th} order satellite peaks.

the average d-spacings of the superlattices at lower annealing temperatures are longer than that of the bulk GaSb. According to the elastic theory of the superlattice strain, the average d-spacing of the InAs/GaSb superlattice is expected to be shorter than that of the bulk GaSb. This is because the d-spacing in a lateral-tensively strained InAs layer is predicted to be shorter than the InAs bulk value by the Poisson effect. The unusual longer average d-spacing in the superlattices implies that there must be some kind of structure with a longer d-spacing incorporated into the superlattice structure to account for the length deficit. Tracking back to the fabrication procedure, we realize that such structure with longer d-spacing is originated from the Sb-soaked interfaces, because these interfaces can be bonded with InAs layers by In-Sb type bondings (longer d-spacings).

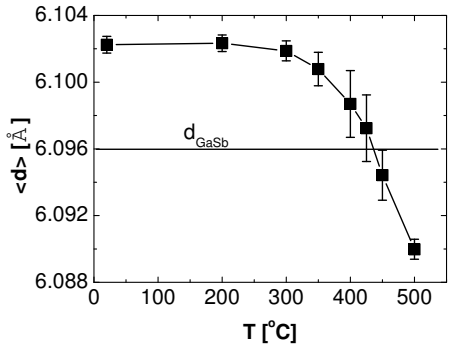

Figure III.6: The average d-spacing of the InAs/GaSb superlattice ($\langle d \rangle$) as a function of the annealing temperature (T). The horizontal straight line is the d-spacing of bulk GaSb (d_{GaSb}).

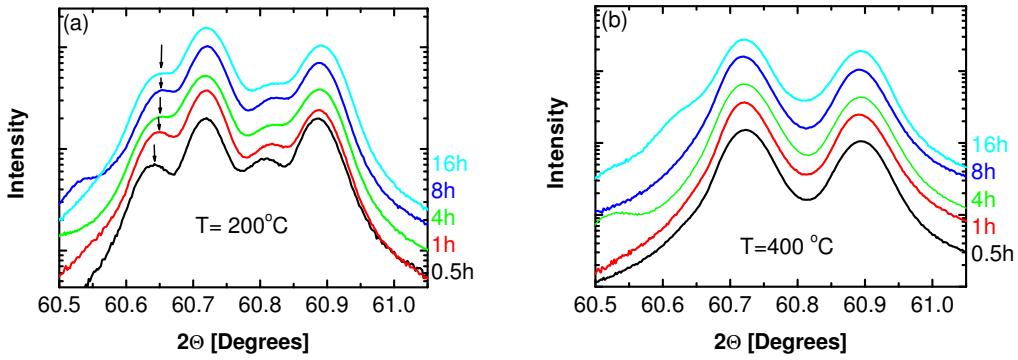

Figure III.7: Center area of the XRD profiles of InAs/GaSb superlattices annealed for different periods at (a) 200 °C and (b) 400 °C. The arrows in (a) indicate the positions of the 0^{th} order satellite peaks.

III.D Time-dependent XRD result

Now that we understand the temperature-dependent behavior of the annealed InAs/GaSb superlattice, we turn our attention to the study on the time-dependent behavior. Two annealing temperatures (200 °C and 400 °C) are chosen here because the previous study suggests structural improvement at 200 °C and structural degradation at 400 °C. Figures III.7(a) and III.7(b) give the XRD profiles at these two temperatures. We find that the 0^{th} order satellite peaks of the 200 °C series drift to the high angle side so slightly that only tiny d-spacing shrinking takes place. The 0^{th} order satellite peaks of the 400 °C series drift so fast that the drifting process cannot be recorded. The strain relaxation at 400 °C is such a quick process that the transition is completed within the shortest annealing period of one half hour. The line shapes of the curves in each series do not differ much. The time-dependence is the secondary in importance to temperature dependence.

III.E Quantitative analysis

The former qualitative discussion is based on general observation from the XRD curves. Further information can be derived from a more careful analysis. The first quantitative result we have is out-of-plane coherence vs. annealing time, which is given in Figure III.8. This curve is similar to Figure III.6. Both the coherence length and the average d-spacing are nearly constant in the range between RT and 300 °C, followed by a sudden drop related to the coherence degradation or the d-spacing relaxation. The samples annealed at 200 °C and 300 °C show the longest coherence length where the long-range out-of-plane inter-layer couplings are also the strongest. Because of the total absence of any noticeable satellite peaks in the curve at 450 °C and 500 °C, there is no possibility to estimate the coherence length. But in principle, the absence of satellite peaks itself strongly discloses the nature of incoherence in these samples.

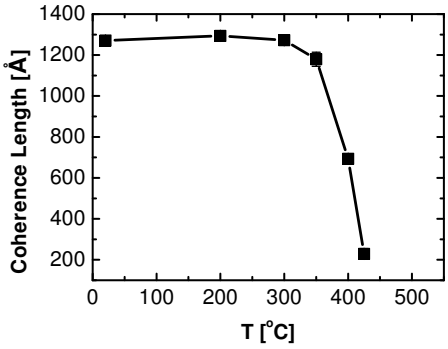

Figure III.8: The out-of-plane coherence length as a function of the annealing temperature. The maximum value can be found at 200 °C.

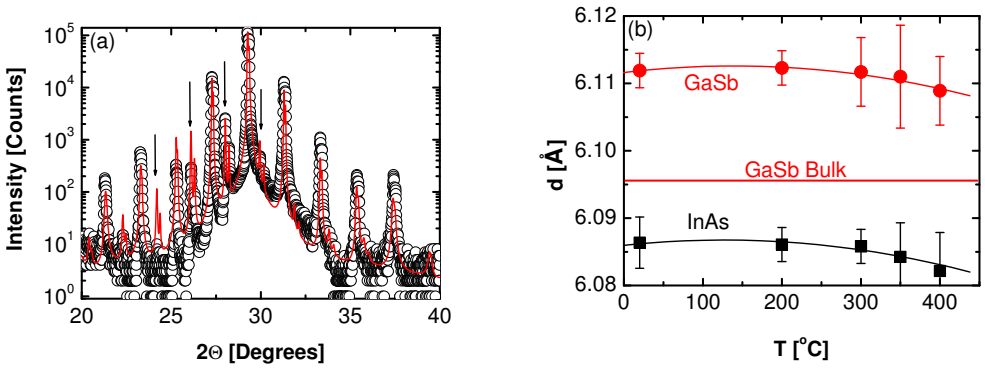

Figure III.9: (a) The experimental data and the SUPREX fitting curve. The additional satellite peaks labeled with arrows are the contribution from the tungsten contamination. (b) The d-spacings of the InAs and GaSb constituent layers given by the SUPREX refinement. The horizontal red line indicates the d-spacing of bulk GaSb.

SUPREX is utilized to analyze these diffraction profiles. Figures III.9(a) and III.9(b) show an example fitting and the refined d-spacings in InAs and GaSb constituent layers. The positive strains confirm the qualitative conclusion. They are identified in both constituent layers. The strains in both layers also demonstrate a contractive relaxation manner as the annealing temperature increases. Due to the unavailability of some higher order satellite peaks, the refined d-spacings yield larger uncertainty at higher annealing temperatures. Above 400 °C, sharper drop of the d-spacings is expected following the trend of the fitting curves. However, this cannot be testified by SUPREX refinement because of the absence of satellite peaks.

III.F Discussion

III.F.1 Additional satellite peaks

Another series of satellite peaks labeled by the arrows in Figure III.9(a) need special attention. We postulate that one additional superlattice with longer average d-spacing than the InAs/GaSb superlattice might yield these satellite peaks. The seemingly additional superlattice structure might be produced from the structural or chemical defects such as threading faults, or from a self-organized structure within the InAs/GaSb superlattice (which is utilized to grow semiconductor nanowires), or from inclined blocks (quite impossible) of the InAs/GaSb superlattice, which we cannot exclude. A more realistic explanation assuming that the additional satellite peaks are from the additional x-ray lines other than CuKα doublets might be the case. Therefore, we should figure out whether the introduction of the additional x-ray lines may reproduce these satellite peaks or not. In fact, the example fitting (Figure III.9(a)) exactly addresses this issue by superimposing the XRD profiles of an InAs/GaSb superlattice from both CuKα doublets and spectral lines with wavelengths of 1.4755 and 1.4864 Å. Next, if we assume that the extra satellite peaks are caused by the additional x-ray lines, there

Table III.1: The characteristic x-ray spectral lines of tungsten.

Line Name	Transition	Wavelength [Å]	Energy [keV]
$K_{\alpha 2}$	$K - L_2$	0.21381	57.99
$K_{\alpha 1}$	$K - L_3$	0.20899	59.32
$K_{\beta 1}$	$K - M_3$	0.18436	67.25
$K_{\beta 1}$	$K - N_3, N_2$	0.17950	69.07
$L_{\alpha 2}$	$L_3 - M_4$	1.48742	8.3356
$L_{\alpha 1}$	$L_3 - M_5$	1.47635	8.3981
$L_{\beta 1}$	$L_2 - M_4$	1.28176	9.6730
$L_{\beta 2}$	$L_2 - N_5$	1.24458	9.9620

must be noticeable similar additional peaks from samples other than the samples in this study. The XRD profiles of the tests run with Au (111) thin film and sapphire wafer confirm the existence of similar additional peaks at the low angle side of the major diffraction peaks, and the wavelengths corresponding to these peaks are quite similar to our prediction. Thus the test supports the hypothesis for the origin of the extra peaks. The spectral lines for tungsten are tabulated in Table III.1. This data is from the *International Tables for Crystallography*. The wavelengths of the W$L\alpha$ doublets match those lines which were chosen for SUPREX simulation. Tungsten contamination is not uncommon in x-ray systems because the filament is made of tungsten. When the rotating target has been used for a long time, tungsten atoms may adsorb on the target surface and emit the unintended characteristic lines, yielding unexpected diffraction spectra.

III.F.2 The backgrounds in XRD profiles

The origin of the XRD backgrounds in Figure III.4 was briefly addressed in Section III.C, but we need to further examine the reasons for these backgrounds.

In general, the modes of film growth or monolayer stacking can be categorized as 1) Layer-by-layer growth or Frank-van der Merve growth, 2) Layer-plus is-

land growth or Stranski-Krastanov growth and 3) Island growth or Vollmer-Weber growth. [95] By which mode the film is grown is determined by the temperature and the material properties via free energy and surface energy minimization.

Growth of III-V alloys on III-V alloys is believed to produce the layer-by-layer mode. Metals on semiconductors can be grown either layer-by-layer or layer-plus-island. [96] The purpose of inserting an Sb-soaked interfacial layer between the InAs constituent layer and the GaSb constituent layer is to avoid Ga-As bonding which frustrates the long-range out-of-plane interlayer correlation. But as a general rule, the deposition of exactly one monolayer of Sb between InAs and GaSb is impossible. Then, Ga-As bondings form at the void sites at the interface and Sb-Sb bonds form at the sites where two or more Sb atoms sit. Both Ga-As and Sb-Sb (usually referred to open bonding) bonding arrangements are not preferable in Zinc-blende III-V InAs/GaSb superlattices. Either the d-spacings differ too much from those of the InAs and GaSb (Ga-As) layers to achieve epitaxial growth, or those bondings violate the symmetry of a Zinc-blende lattice (Sb-Sb) so that a long-range coherent lattice cannot be established. In the original superlattices (without annealing), the Ga-As and Sb-Sb bonds, which weaken the inter-layer correlation, do exist because of the quasi-equilibrium nature of the epitaxial growth. Thus, fewer satellite peaks and a background to the left of the GaSb substrate peak appear in the XRD profile.

The Ga-As bonds deform the lattice locally, increasing elastic energy. The Sb-Sb bonds or void sites increase the local electrostatic energy. All of these extra energy costs can be eliminated by a moderate annealing which accelerates the local relocation of Sb atoms along the interfacial plane and encourages the incorporation of free bonding atoms with the entire superlattice. Thus, the out-of-plane coherence is improved.

However, as the annealing temperature increases, the thermally-introduced atomic global migration becomes more significant, which makes the segregation of As in InAs layer or the segregation of Sb in GaSb layer more likely. So the struc-

tures of GaAs or InSb may be formed at even lower energy levels (we do not know whether those structures are domained or extensive along the interfaces). Thus traces of the GaAs background are expected in the XRD profiles for heavily annealed samples. Due to global chemical segregation and intermixing, the boundary between two constituent layers becomes less identifiable and finally disappears. As the segregation and intermixing continue, the superlattice structure transforms to a more thermally favorable form with the loss of superlattice as the cost.

The process of local interfacial atom relocation and incorporation, and the process of global chemical segregation and intermixing compete each other and result in an optimized condition where the superlattice has the best quality (the longest coherence).

III.G Conclusion

Ex situ annealed InAs/GaSb superlattices were studied using AFM morphology and x-ray diffraction techniques. Quantitative structural characterization on the superlattices was also performed. Our results show that the annealing at temperature between 200 °C and 350 °C for 1 hour in HVAC improves the out-of-plane coherence of the InAs/GaSb supelattices, which is the major criterion to quantify the structural quality of a superlattice. The annealing above this temperature range results in a structural degradation demonstrated by the disappearance and broadening of the higher order satellite peaks. Heavy annealing above 425 °C will entirely eliminate the chemical modulation of a superlattice structure. Therefore, only the diffraction features from the substrate and the complicated quaternary or ternary alloy of In-As-Ga-Sb are left. The time-dependent annealing study shows that the structural transition (strain relaxation) of the InAs/GaSb superlattices at 200 °C is extremely slow and insignificant. However, strain relaxation occurs in a period of time shorter than 0.5 hour, indicating that the chemical intermixing and the anion segregation are fast processes.

The surface morphology also evolves as the annealing temperature changes. With increasing annealing temperature, the surface becomes rougher and rougher. The morphology is also drastically transformed from a flat plane at the atomic scale to a macroscopic island-patterned surface, which implies that the nucleation becomes severe at higher temperatures.

Unexpected additional satellite peaks are discovered and explained by the diffraction profile from a tungsten-contaminated rotating target; however, the possible explanation, which relies on the nature of the samples instead of the x-ray target, is not excluded.

III.H Acknowledgement

This work was supported by AFOSR MURI # F49620-02-1-0288.

IV

One-dimensional model of phthalocyanine thin films

The macromolecular structure is routinely reconstructed using single crystal or powder x-ray diffraction experiment in conjunction with a procedure called Rietveld refinement. Due to limitations of diffraction, phase information is usually inaccessible from an ordinary diffraction experiment (there are exceptions, but very strict experimental condition must be satisfied). One classic technique for retrieving the phase information is called isomorphous replacement, which substitutes certain atoms within the molecule with other atoms (usually heavy atoms) to perturb the diffraction pattern in order to deduce an estimate of the phase information. However, in the case of thin film x-ray diffraction, the information obtained from the specular diffraction is too limited for any attempt to restore the molecular structure. There is a common misunderstanding that the inner-molecular structure (the structure related to the molecule without considering the lattice structure) does not significantly influence the x-ray diffraction (XRD) profile of a thin film, especially when the diffraction peaks belong to the same series of lattice planes. However, the inner-molecular phase cancellation greatly influences the XRD profile at large angular scale due to the Convolution Theorem. [1] When dealing with larger and more anisotropic molecules, the influence can be so

crucial that it is possible to collect structural information about the molecule and its spatial arrangement from the very limited experimental data.

In the past two decades, there have been advancements to ultrahigh vacuum (UHV) techniques to control the growth of organic thin films. This has boosted the research on the optoelectronics based on organic materials. [97] The so-called organic molecular beam deposition (OMBD) or organic molecular beam epitaxy (OMBE) is superior to other deposition methods such as Langmuir-Blodgett deposition [98] or self-assembled monolayers from solution [99] due to its precise control over the deposited structure. Organic materials, such as phthalocyanines and other polycyclic aromatic compounds, such as hexaphenyl, pentacene, perylene, perylene-3,4,9,10-tetracarboxylic-3,4,9,10-dianhydride (PTCDA), hexabenzocoronene and diindenoperylene etc., are recently receiving intensive study as the working agents in gas sensors, photodiodes and solar cells. The optoelectronic properties of such molecules were discussed comprehensively by Forrest. [61]

As we showed in Chapter I, crystalline phthalocyanines (Pc), which have polymorphous structure, mainly appear as the α and β phases. [100, 101, 102] The phthalocyanine thin film deposited on the top of a metal (e. g. Au or Pt) or PTCDA buffer layer, may show X phase because of the strong attraction between the center metal atom and the metal substrate. As the most common in bulk form, β phthalocyanines are room-temperature stable crystalline powder-like materials with monoclinic lattices with two molecules per unit cell, while the α phthalocyanines, which appear most commonly in UHV deposition, have quasi-orthorhombic lattices with four molecules per unit cell. In addition to the difference between unit cells, phthalocyanine molecules can have different tilt angles with respect to the b-axis of the lattice, which is often called the molecular stacking axis, in both α and β phases. [55] Both α and β phthalocyanines can be prepared using OMBD techniques by varying the substrate temperature. Since the β phthalocyanines are more thermally stable than the α phthalocyanines, the latter can be transformed into the former one by post-growth annealing in the temperature range from 200 °C

Table IV.1: Summary of bulk crystal structural parameters for α and β phases of phthalocyanines (See ref. [103]).

	α H_2Pc	β H_2Pc	α CuPc	β CuPc	α FePc	β FePc
a [Å]	26.14	19.85	25.92	19.6	25.90	20.2
b [Å]	3.184	4.72	3.790	4.79	3.765	4.77
c [Å]	23.97	14.8	23.92	14.6	24.10	15.0
β [°]	91.1	122.25	90.4	120.6	90.0	121.6
number of molecules	4	2	4	2	4	2
space group	C2/C	$P2_1/a$	C2/C	$P2_1/a$	C2/C	$P2_1/a$

to 250 °C. [67] The structural parameters of some common phthalocyanine compounds, taken from Buchholz *et al.* [103], are tabulated in Table IV.1.

It is generally believed that the lattice structure and the molecular arrangement strongly impact the magnetic properties of the phthalocyanines. [104, 105, 106] When the central atom is replaced, phthalocyanines show different behavior in the electronic spectrum. This is a crucial feature in the devices based on the phthalocyanines. [68] For example, a metal-free phthalocyanine molecule has two hydrogen atoms at the center, and its properties are mainly determined by the policyclic phthalocyanine ring. On the other hand, metallophthalocyanines (e.g. iron phthalocyanine) have a metal atom at the center which may provide free carrier and unpaired spin to the whole system, determining the electrical and magnetic behaviors of metallophthalocyanine materials.

In this chapter, we present the experimental and theoretical results in order to find a criterion using x-ray diffraction (XRD) to differentiate metal-free phthalocyanine from metallophthalocyanines. We will show that the center atom and the tilt angle of the molecules dominate the diffraction pattern (the relative intensity of diffraction peaks), although such factors are generally not considered. More importantly, the conclusion can be generalized to other systems with similar structural nature. We obtain the numerical results using a full calculation method by incorporating the molecule, lattice structure and the substrate into a framework.

Our goal is not to achieve the least fitting error, but to show how the structural parameters such as the core charge density, the tilt angle and the substrate gap influence the XRD profile. We will also address the difference of the full calculations from the existing approximations. The contribution from the substrate, which turns out to be a small correction to the calculation, is discussed. Finally, the molecular orientation relaxation in the layer stacking direction is addressed, and the possible range for the relaxation is presented. The effect of the relaxation of the tilt angle on the diffraction profile is analyzed.

IV.A The description of the one-dimensional model

IV.A.1 Structure of the model phthalocyanine molecule

A metallophthalocyanine molecule with 32 carbon atoms (grey), 8 nitrogen atoms (blue), 1 metal atom (red), and 16 hydrogen atoms (cyan) is shown in Figure I.3. The structure of metal-free phthalocyanine is slightly different in which the center metal atom is substituted by two hydrogen atoms with non-zero displacement along the symmetry axis. In most cases, the displacement can be neglected due to the fact that the center hydrogen atoms do not provide carriers and show the least diffraction cross-section. The molecule is planar in the case of metal-free phthalocyanine or compounds of light metal, such as copper phthalocyanine (CuPc). Compounds of heavy metals (e. g. lead phthalocyanine or PbPc) take the shape of badminton birdies. Extensive studies of the molecular structure have been made using Rietveld refinement [55, 107, 108, 109] and DFT/HF calculation. [110, 111] The results suggest that the phthalocyanine ring does not deform significantly when replacing the center hydrogen atoms with other light metal atoms. Therefore, to avoid complications of molecular deformation, we assume a rigid phthalocyanine ring with a 4-fold symmetry in the following calculations. The coordinates of these atoms are listed in Table IV.2.

Table IV.2: The XYZ coordinates of all the atoms in the model phthalocyanine molecule. The small displacement of two center hydrogen atoms in a H_2Pc molecule along the symmetry axis is neglected. M refers to the center metal atom or two H atoms.

Index	Element	X [Å]	Y [Å]	Z [Å]	Index	Element	X [Å]	Y [Å]	Z [Å]
1	M	0	0	0	30	C	1.384	5.2	0
2	N	1.8	0	0	31	C	-1.384	5.2	0
3	N	-1.8	0	0	32	C	1.384	-5.2	0
4	N	0	1.8	0	33	C	-1.384	-5.2	0
5	N	0	-1.8	0	34	C	6.4	0.692	0
6	N	2.31	2.31	0	35	C	-6.4	0.692	0
7	N	-2.31	2.31	0	36	C	6.4	-0.692	0
8	N	2.31	-2.31	0	37	C	-6.4	-0.692	0
9	N	-2.31	-2.31	0	38	C	0.692	6.4	0
10	C	2.6	1.11	0	39	C	-0.692	6.4	0
11	C	-2.6	1.11	0	40	C	0.692	-6.4	0
12	C	2.6	-1.11	0	41	C	-0.692	-6.4	0
13	C	-2.6	-1.11	0	42	H	5.2	2.384	0
14	C	1.11	2.6	0	43	H	-5.2	2.384	0
15	C	-1.11	2.6	0	44	H	5.2	-2.384	0
16	C	1.11	-2.6	0	45	H	-5.2	-2.384	0
17	C	-1.11	-2.6	0	46	H	2.384	5.2	0
18	C	4	0.962	0	47	H	-2.384	5.2	0
19	C	-4	0.962	0	48	H	2.384	-5.2	0
20	C	4	-0.962	0	49	H	-2.384	-5.2	0
21	C	-4	-0.962	0	50	H	7.266	1.192	0
22	C	0.962	4	0	51	H	-7.266	1.192	0
23	C	-0.962	4	0	52	H	7.266	-1.192	0
24	C	0.962	-4	0	53	H	-7.266	-1.192	0
25	C	-0.962	-4	0	54	H	1.192	7.266	0
26	C	5.2	1.384	0	55	H	-1.192	7.266	0
27	C	-5.2	1.384	0	56	H	1.192	-7.266	0
28	C	5.2	-1.384	0	57	H	-1.192	-7.266	0
29	C	-5.2	-1.384	0					

IV.A.2 Interpolation of the atomic scattering factor

Bound electrons in an atom show discrete energy levels. The electrons in the K shell are the most tightly bounded to the nucleus. These electrons usually have binding energies comparable to typical x-ray photons. The main term of the scattering factor for an atom comes from the elastic scattering, which is given by Equation I.5. A small real correction and a small imaginary correction are given at the absorption edges to include the dissipation behavior. By collecting these terms the total atomic scattering factor (sometimes called atomic form factor) can be written as

$$f\left(\mathbf{Q},\hbar\omega\right)=f^{0}\left(\mathbf{Q}\right)+f'\left(\hbar\omega\right)+if''\left(\hbar\omega\right) \tag{IV.1}$$

where the second and the third terms are known as the dispersion corrections. Given the wavelength of the x-ray source, these terms can be found in the *International Tables of Crystallography*. The energy of the x-ray, $\hbar\omega$, in Equation IV.1 is not explicitly shown in the elastic scattering (diffraction) case.

The first term in Equation IV.1 is solely a function of the momentum transfer. Methods for calculating this term are given in the *International Tables of Crystallography* and need no more discussion. The analytical interpolation of the atomic scattering factor can be written as

$$f^{0}\left(\frac{\mathrm{Q}}{4\pi}\right)=\sum_{j=1}^{4}a_{j}e^{-b_{j}\left(\frac{\mathrm{Q}}{4\pi}\right)^{2}}+c=\sum_{j=1}^{4}a_{j}e^{-b_{j}\left(\frac{\sin\Theta}{\lambda}\right)^{2}}+c \tag{IV.2}$$

where the fitting coefficients can be found in the same reference. Equation IV.2 is accurate enough when the momentum transfer is in moderate range. Thus, it is suitable for our numerical study.

IV.A.3 The molecular scattering factor of phthalocyanine

Based on the analytical interpolation of individual atomic scattering factors, we may consider the scattering from a phthalocyanine molecule by summing

the contribution from all 57 atoms as

$$F^{\mathrm{Pc}}(\mathbf{Q}) = \sum_{j=1}^{57} f_j(\mathbf{Q})\, e^{i\mathbf{Q}\cdot\mathbf{r}_j} = F^{\mathrm{Center}}(\mathbf{Q}) + F^{\mathrm{Ring}}(\mathbf{Q}) \tag{IV.3}$$

Because the imaginary part of the center atomic scattering factors is typically small, the imaginary part of Equation IV.3 is mainly determined by the contribution from the ring (phthalocyanine ring). However, the real part of the scattering factor of the center atom can be quite significant, and cannot be neglected. Unlike for a single atom, where the imaginary part of the scattering factor is a constant, the imaginary part of the molecular scattering factor is related to the spatial distribution of the molecule which is not constant.

IV.A.4 The structure factor and one-dimensional layer chain

A crystalline material is extended by periodically repeating a primitive unit cell in a three-dimensional space. The unit cell is either composed of several atoms or composed of several molecules depending on the material. The diffraction pattern from a single crystal is determined by the Laue conditions and is described by the so-called reciprocal lattice. Major diffraction peaks are expected when the momentum transfer equals the linear combination of whole-number multiples of three independent reciprocal unit vectors. Although the position of the diffraction peaks are entirely determined by the lattice structure and the lattice symmetry, the intensity of the diffraction peaks is determined by the diffraction pattern from a unit cell together with the lattice. The scattering factor from a unit cell is termed as the unit cell structure factor, or more concisely the structure factor, which is defined by the equation

$$F^{\mathrm{Cell}}(\mathbf{Q}) = \sum_{j=1}^{Z} F_j^{\mathrm{Pc}}(\mathbf{Q})\, e^{i\mathbf{Q}\cdot\mathbf{R}_j} \tag{IV.4}$$

where $F_j^{\mathrm{Pc}}(\mathbf{Q})$ refers to the indexed molecular scattering factor from the j^{th} molecule, Z is the number of molecules per unit cell, and $\mathbf{R}_j$ is the indexed position of the j^{th} molecule.

In a single-element unit cell, or in a unit cell composed of one type of isotropic molecules, the atomic or molecular scattering factor is constant or position-independent. Thus these atoms or molecules are considered identical for the x-ray diffraction. The situation is complicated when the unit cell is constructed with one type of anisotropic molecules, because the molecular scattering factor at each site is not necessarily the same, especially when the angular arrangement of these molecules is anisotropic. As a special case, two distinct groups of phthalocyanine molecules are packed into unit cells forming herringbone structures. Thus, given an arbitrary momentum transfer, different diffraction amplitudes result despite these two molecular groups having the same chemical composition.

The AFM or SEM study suggests that the phthalocyanine film forms a polycrystalline structure in-plane and has a layered structure in the out-of-plane direction, which is labeled as $(h00)$ direction for α type of lattice or $(00l)$ direction for β type of lattice. This type of thin film can be modeled as a one-dimensional (1D) layer chain if no lateral correlation is present. Each site along the 1D chain represents a contribution from a phthalocyanine monolayer. Since the lateral structure is not incorporated into the 1D model, the model is incapable of addressing the momentum transfer with a lateral component. We stipulate that our discussion based on 1D model only applies to normal specular diffraction in the absence of lateral momentum transfer and in-plane correlation. Additional efforts will be made in Chapter V to tackle the problems beyond normal diffraction.

IV.A.5 The phthalocyanine thin film with a rough surface

Phthalocyanine films are deposited following a growth mode called Stranski-Krastanov growth, where the film forms a layer-plus-island structure. Except for the continuous out-of-plane deformation and the thermal vibration, the surface of the phthalocyanine film is considered a terrace-like stepping surface. General discussion on the x-ray diffraction from a rough surface is not given here but can be found in the results by Wong [112] and Sinha *et al.* [20] The scaling behavior

and surface roughening of the H_2Pc thin films was studied by Yim *et al.* [66] We do not intend to discuss the discrete roughness of the phthalocyanine films in this chapter because the intensity at each major Bragg peak is independent of discrete roughness (the intensity is related to the continuous roughness, but the introduction of the continuous roughness only imposes a Debye-Waller-like damping factor if the diffuse scattering is not considered), [1] which is also confirmed by my numerical studies. To simplify the discussion, we assume the diffraction is totally coherent, and the surface roughness is totally uncorrelated, so that the diffraction amplitude takes the average value according the discrete roughness. The intensity is the product of the averaged amplitude with its complex conjugate:

$$\begin{aligned} I(\mathbf{Q}) &= corr \left\langle \sum_{n=0}^{N-1} F^{\mathrm{Cell}}(\mathbf{Q})\, e^{iQn\Lambda} \right\rangle^{*} \left\langle \sum_{\mathrm{n}=0}^{\mathrm{N}-1} F^{\mathrm{Cell}}(\mathbf{Q})\, e^{iQn\Lambda} \right\rangle \\ &= corr \left| F^{\mathrm{Cell}}(\mathbf{Q}) \right|^2 \left\langle \sum_{n=0}^{N-1} e^{-iQn\Lambda} \right\rangle_N \left\langle \sum_{n=0}^{N-1} e^{iQn\Lambda} \right\rangle_N \end{aligned} \tag{IV.5}$$

where *corr* is the correction coefficient termed as the product of Lorentz factor, projection factor and polarization factor (instrumental correction), [1] Λ is the monolayer d-spacing, and N is the total number of the monolayers.

IV.A.6 The correction from the substrate

Equation IV.5 gives the intensity of the specular diffraction from a phthalocyanine plain film with an uncorrelated stepping surface. The phthalocyanine molecules, which are mainly composed of light elements (H, C and N), are more loosely packed in a unit cell than other inorganic thin films. Therefore, given the film thickenss, the XRD intensity from a phthalocyanine film is much weaker than that from its inorganic corollary. The background intensity from the substrate, which is usually inorganic, is so strong at low angles that the contribution from the substrate should not be ignored. A typical correction for the substrate is to add a Lorentzian line to the diffraction profile of a plain film without considering the phase cancellation between the substrate and the film. In our study, the phase cancellation is included by introducing a parameter termed the "substrate gap",

which is defined in Figure IV.1. Equation IV.5 is modified to

$$I(\mathbf{Q}) = corr \left\langle F^{\mathrm{Sub}}(\mathbf{Q}) + e^{iQ\Delta} F^{\mathrm{Film}}(\mathbf{Q}) \right\rangle^{*} \left\langle F^{\mathrm{Sub}}(\mathbf{Q}) + e^{iQ\Delta} F^{\mathrm{Film}}(\mathbf{Q}) \right\rangle \quad \text{(IV.6)}$$

where the term from the substrate is calculated using $F^{\mathrm{Sub}}(\mathrm{Q}) = \int_{-\infty}^{0} \rho(z) e^{-\frac{\mu z}{2}} e^{iQz} dz$. $\rho(z)$ is the electron density of the substrate, and μ is the attenuation of the substrate.

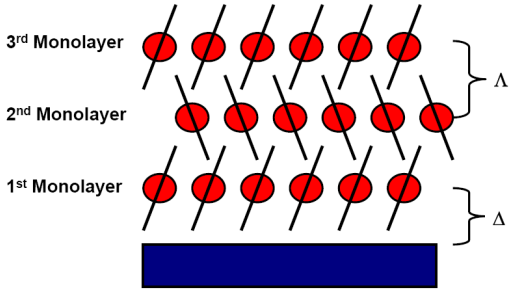

Figure IV.1: The definition of the subtrate gap Δ, which is the distance between the edge of the substrate and the center of the 1^{st} phthalocyanine monolayer; the definition of the d-spacing of phthalocyanine monolayer Λ.

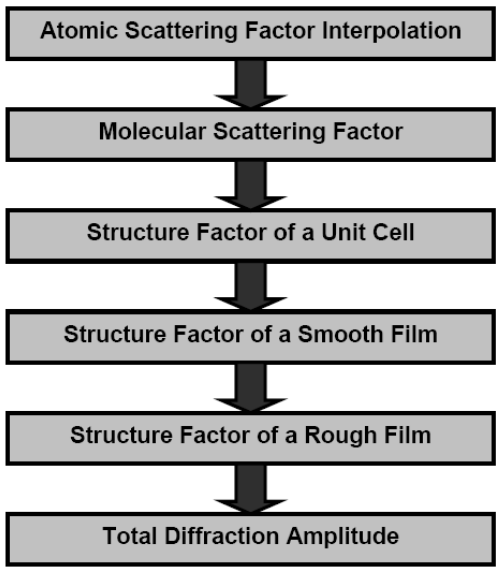

Figure IV.2: The derivation steps of the theory for the numerical study in this chapter.

The whole procedure for the calculation is illustrated by Figure IV.2,

which shows the steps how the calculation is performed.

IV.B The numerical and experimental results

X-ray diffraction from thin films of covalently-bonded inorganic materials such as InAs, GaAs semiconductors and small organic molecules with slight spatial anisotropies can be modeled using a theory based on a one-dimensional atomic monolayer chain. The inner-molecular structure is neglected. This approach works well not only with thin films but also with multi-layers and superlattices. [41] Previous quantitative studies on the x-ray diffraction from phthalocyanine thin films focus on the interlayer (between stacked monolayers) structural parameters such as d-spacing, roughness and strain. They assume either a step-function, [72] a sinusoidal [113] or a Gaussian [73] electron density profile within a monolayer. To simulate the asymmetry of the Bragg oscillations about the main diffraction peak around 6.8°, an amorphous capping (buffer) layer layer was assumed to achieve better fits. [72, 73] Our theory includes the features of the molecular structure. To describe the full calculation, we first need to consider the diffraction from a single phthalocyanine molecule.

IV.B.1 The molecular scattering factor and the electron density

The molecular coordination, the azimuthal angle and the polar angle of a phthalocyanine molecule are depicted in Figure IV.3. The tilt angle θ, which is defined as the angle between the molecular symmetry axis and the column stacking b-axis, has the same value as the polar angle here. The difference between the scattering factors of a copper phthalocyanine (CuPc) molecule at different tilt angles is demonstrated in Figure IV.4(a)- IV.4(f). When the momentum transfer is parallel to the z-axis, the real part of the molecular scattering factor is azimuthally isotropic and the imaginary part is a constant. As the momentum transfer deviates from the z-axis, both the real and the imaginary parts of the molecular scattering

factor become azimuthally anisotropic and the imaginary part is no longer constant. The mappings in Figure IV.4(c)- IV.4(f) are 4-fold symmetric, which is the same as the symmetry in real space. Such parity indicates that the symmetry is conserved after a Fourier transformation. We also notice that the patterns of the real part and the imaginary part are similar although the amplitude can be very different. The similarity between the real and imaginary parts of the scattering factors indicates that the structural information is encoded in both the real and imaginary parts.

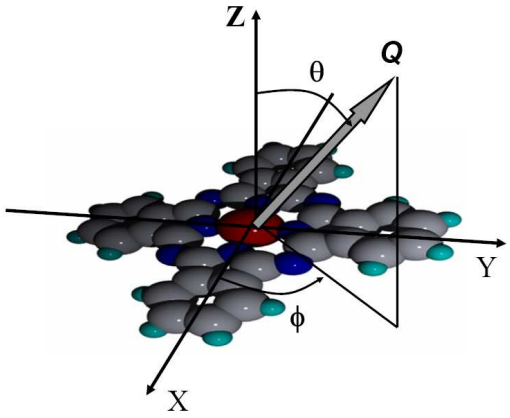

Figure IV.3: The molecular coordinates (XYZ), the azimuthal (ϕ) and polar (θ) angles of the momentum transfer (**Q**). In this graph, the red atom is the center atom; blue atoms are nitrogen atoms; grey atoms are carbon atoms; and cyan atoms are hydrogen atoms.

Figure IV.5 shows the scattering factor as a function of the diffraction angle, for a Cu atom and for CuPc at different tilt angles. Both the scattering factor for a Cu atom and the scatting factor for CuPc at zero tilt angle show steadily decaying as the diffraction angle increases (the momentum transfer increases). But the two scattering factors in the titled cases show a very complicated dependence on angle - a sharp drop within $0 - 10^{\circ}$ and several zero points at high angles. Figures IV.6(a) and IV.6(b) are the 2D mappings of the product of the scattering factor with its complex conjugate for a H_2Pc and CuPc respectively. Increasing tilt angle pushes the valleys in Figures IV.6(a) and IV.6(b) to higher angles. When

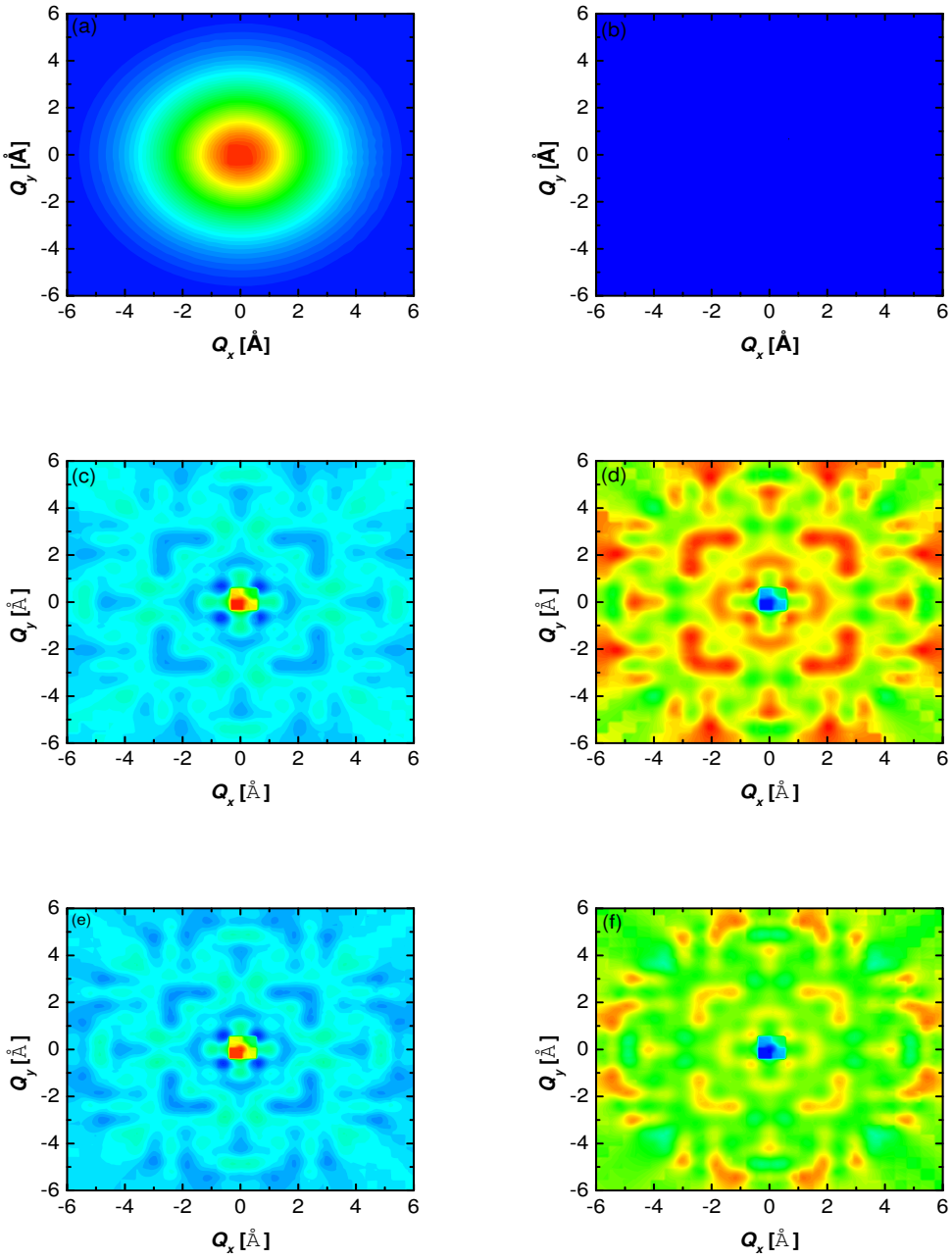

Figure IV.4: Two-dimensional molecular scattering factor maps of copper phthalocyanine (CuPc). (a) the real part as $\theta \to 0$, (b) the imaginary part as $\theta \to 0$; (c) the real part when $\theta = 64°$, which is the $\alpha - (100)$ direction, (d) the imaginary part when $\theta = 64°$; and (e) the real part when $\theta = 90°$ which is the $\beta - (001)$ direction, (f) the imaginary part when $\theta = 90°$.

the tilt angle approaches 90°, these valleys disappear. Differences can also be found between the mappings for these two molecules. The pattern for H_2Pc shows lower density in the middle range; thus it is more anisotropic than the CuPc because the anisotropy of the latter is partially offset by the heavier center Cu atom.

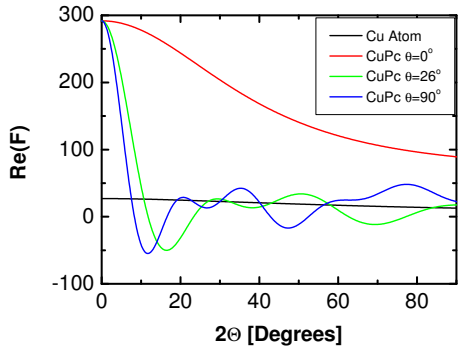

Figure IV.5: The calculated real parts of the scattering factors from a Cu atom and a CuPc molecule when the azimuthal angle (ϕ) equals 45°, the wavelength of the x-ray is 1.5418 Å, and the tilt angle (θ) equals 0°, 26° and 90° (natural unit).

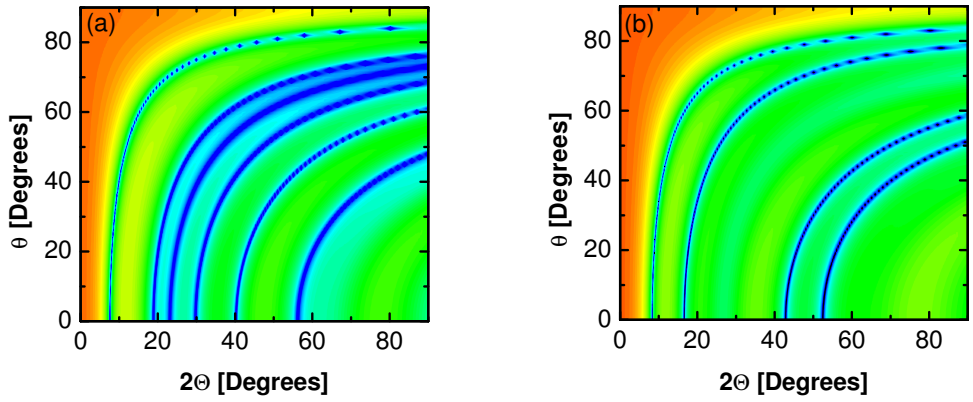

Figure IV.6: The product of the molecular scattering factor with its complex conjugate as the function of the diffraction angle 2Θ and the tilt angle θ in logarithmic scale for (a) H_2Pc and (b) CuPc.

To understand why the molecular scattering factor is so sensitive to the tilt angle, we need to know what happens when the molecule is tilted. Fig-

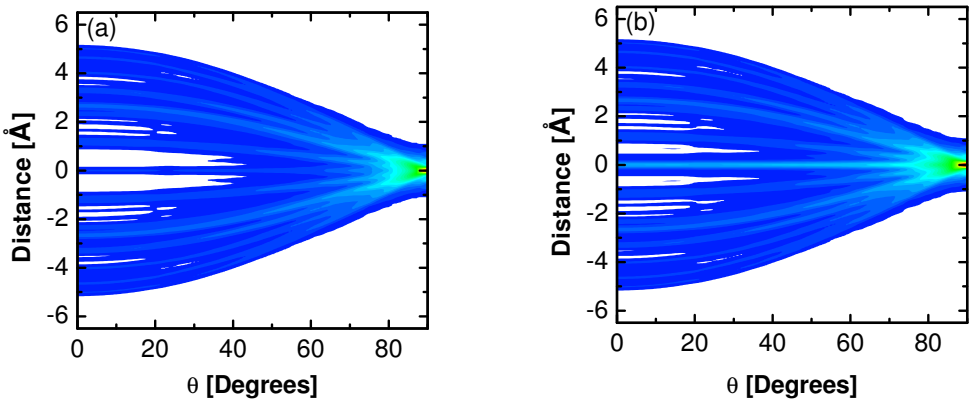

Figure IV.7: The electron density map as a function of the tilt angle (θ) and the distance from the center atom for (a) H_2Pc and (b) CuPc.

ures IV.7(a) and IV.7(b) illustrate the spatial electron density maps as a function of tilt angle for H_2Pc and CuPc over a distance of 13 Å, which is about the d-spacing of a phthalocyanine monolayer. The electron density of each individual atom is calculated from an inverse Fourier transform from the atomic scattering factor analytically interpolated using the method given in IV.A.2. The patterns far from the x-axis are identical and the center area of CuPc show higher electron density than that of H_2Pc. The pattern of electron density stretches out farther along the y-axis at lower tilt angles and collapses to a Gaussian-like distribution at 90°. The electron density profiles at 0° and at 26° represent the values for β (vertically standing) and α phases (tilted), respectively. The electron density profile at 90° represents the case when phthalocyanine molecules lay parallel on the substrate, which is also equivalent to the approximation that all atoms within the molecule sit together at the center. The different electron density in real space and the subtle difference of the electron density at the center area for different phthalocyanine compounds cause significant changes in the scattering factor curves.

IV.B.2 The number of monolayers and the bulk limit

The positions of the diffraction peaks from a plain film are the same as the positions of the diffraction peaks from a bulk material if the d-spacings are chosen the same. However, this is not true if the contribution from the substrate is included, especially when the film is deposited on a substrate with a very different lattice constant. The diffraction peaks drift significantly at low angles where the diffraction shoulder plays an essential role. In order to exclude such an "artificial" drifting effect from the discussion, a thin film should satisfy the following conditions: A) the film is not thick enough that finite-size oscillations disappear; B) the film is not thin enough that the essential features of the diffraction profile are very sensitive to the thickness.

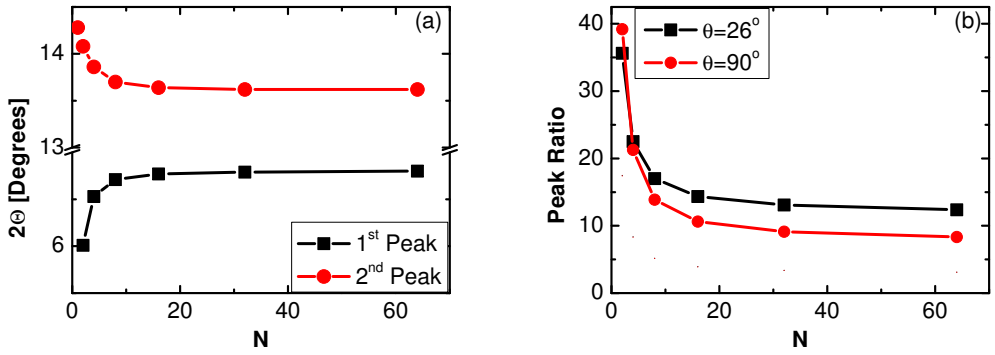

Figure IV.8: (a) The position of the 1^{st} and 2^{nd} order diffraction peaks and (b) the intensity ratio of the 1^{st} to 2^{nd} order diffraction peaks as a function of the number of CuPc monolayers (N).

Figure IV.8(a) gives the positions of the 1^{st} and 2^{nd} order diffraction peaks from a CuPc thin film on the sapphire substrate as a function of the number of CuPc monolayers, assuming a 26° tilt angle, a 13 Åd-spacing and 10% roughness. Figure IV.8(b) shows the intensity ratio of the 1^{st} order peak to the 2^{nd} order peak. Both the position of the peaks and the intensity ratio change drastically when there are a small number of monolayers. When the number of monolayers is greater than 16, these values converge to the bulk limits. In the following studies,

we assume that the number of monolayers is 20. We also intend to deposit thin films about 20 monolayers thick.

IV.B.3 Phenomenological observation on the calculated XRD profiles

Several different approaches are chosen to compare the diffraction profiles of a phthalocyanine film. These approaches are, A) assume the diffraction is contributed entirely from the center atom, B) assume the diffraction from the phthalocyanine molecule when all atoms sit at the same site, C) assume the diffraction is from the phthalocyanine molecule, including the molecular structure with the lattice arrangement of the α phase and finally D) the diffraction is from the phthalocyanine molecule, including the molecular structure with the lattice arrangement of the β phase. In principle, these models assume different electron density distributions. Models A) and B) assume a Gaussian-like electron density but differ in the magnitude. The calculations from models C) and D) differ in the molecule tilt angle resulting in complicated and unique electron density distributions.

Figure IV.9(a) shows the XRD profiles from a plain CuPc film calculated using models A) to D) assuming 10% roughness. Unlike the prediction from models C) and D), models A) and B) do not show complete intensity cancellations between the 1^{st} and 2^{nd} order peaks, and between the 2^{nd} and 3^{rd} order peaks. More realistic calculations of the XRD profiles require the introduction of the substrate background, which are demonstrated in Figures IV.9(b) for CuPc and IV.9(c) for H_2Pc. There are no observable diffraction peaks from model A) for H_2Pc because the two center H atoms are virtually transparent to x-rays. We conclude that model A) which only counts the diffraction from the center atom(s) is an unreasonable approximation; it does not reproduce the XRD profile from a H_2Pc film. By carefully comparing the XRD profiles between models B), C) and D), we also realize that the relative intensity of the diffraction peaks over the background intensity varies for models C) and D) but not for model B). The comparison between the

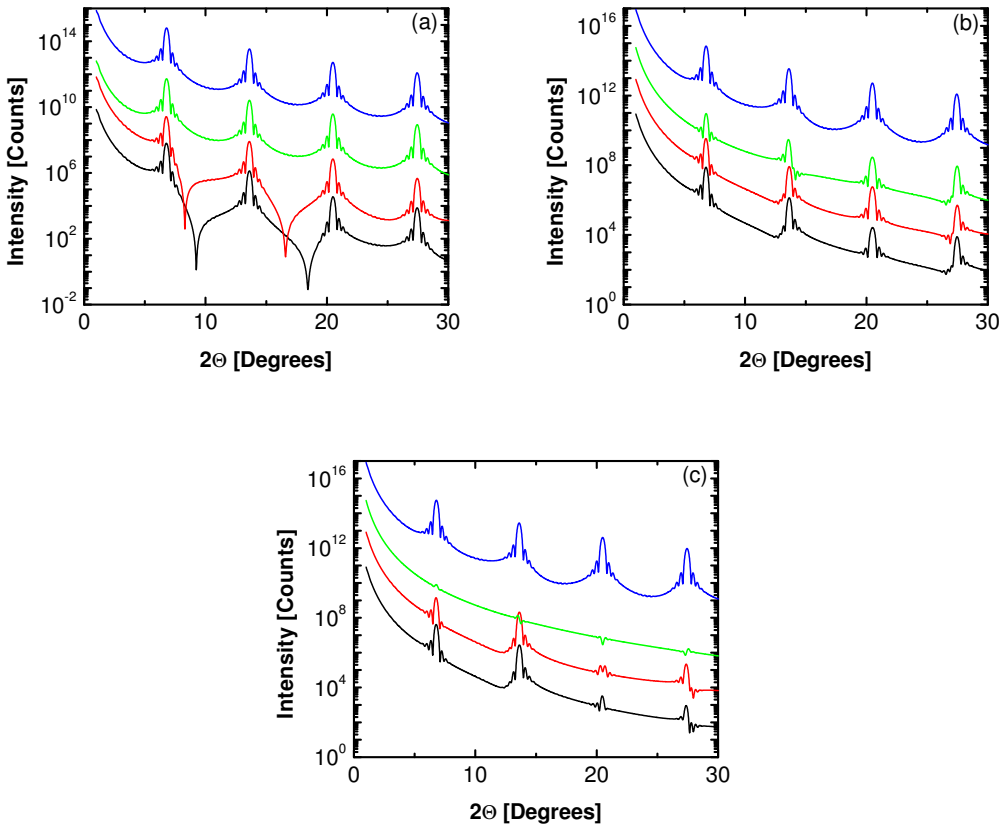

Figure IV.9: The XRD profiles calculated using different models for (a) a plain CuPc film, (b) a CuPc film on a sapphire substrate and (c) a H_2Pc film on a sapphire substate. Green, blue, black and red lines are the XRD profiles of model A, B, C and D respectively.

results from CuPc and H_2Pc films also suggests that the intensity ratios between the different diffraction peaks are compound-relevant for models C) and D), but not for model B).

IV.B.4 The effect of the center atom(s)

In order to understand the extent to which the center atom changes the XRD profiles using calculation based on models C) and D), we artificially introduce different center atoms with atomic indices between 1 (H) and 56 (Ba) into the phthalocyanine ring. Figure IV.10(a) shows the intensities of the 1^{st} and 2^{nd} order peaks as a function of the atomic index of the center atom. It is not surprising to find that the intensity of the 1^{st} order peak increases approximately logarithmically due to the increase in the total number of electrons within a molecule (The results show that a logarithmical fitting is better than a quadratic fitting); however, the decreasing intensity of the 2^{nd} order peak is unexpected. This decrease can only be explained by phase cancellation within the phthalocyanine molecule. Figure IV.10(b) shows the intensity ratio of the 1^{st} order peak to the 2^{nd} order peak, which also increases with atomic number. Similar calculations can be performed using model B), but the intensity of the 2^{nd} order peak steadily increases as the atomic index goes larger.

To determine which model satisfies the experimental result, we fabricated two series of phthalocyanines thin films. Thin films of H_2Pc and CuPc, about 20 monolayer thick, were deposited on (0001) sapphire substrates using OMBD methods and the XRD profiles were taken using either a Bruker D8 or a Rigaku RU200 system. The intensities at the 1^{st} and 2^{nd} order peaks were recorded using rocking curves. Figure IV.11 shows the XRD profiles of two H_2Pc and CuPc samples for comparison. The even order diffraction peaks of CuPc film are significantly lower than those of H_2Pc. The bumps at 3.3°, 6.6°, and so on, are related to the background from the sapphire substrates. Plotting the ratio of the 1^{st} and 2^{nd} order peaks for these samples, we find that the experimental data (dots) matches the

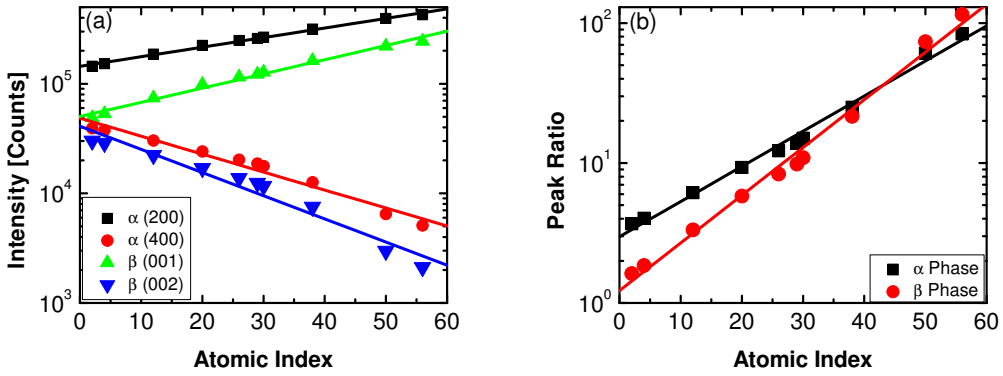

Figure IV.10: (a) The intensity of the 1^{st} and 2^{nd} order peaks as a function of the atomic index of the center atom, and (b) the intensity ratio of the 1^{st} order peak to the 2^{nd} order peak.

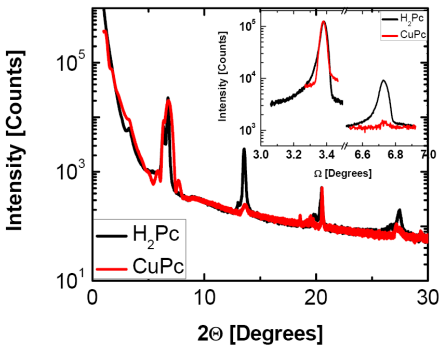

Figure IV.11: The experimental XRD profiles of H_2Pc (black) and CuPc (red) OMBD films. The insert graph shows the rocking curves.

simulations of the a phase (straight lines) in Figure IV.12. Thus, we conclude that the model incorporating the molecular structure reproduces the XRD features of phthalocyanine films. Both model A), which has already been excluded, and model B) are unable to predict the compound-relevant change in the intensity ratio. The calculation based on model C), based on the α phase, yields a better prediction than model D), based on the β phase. This point confirms previous studies, which suggest that the OMBD phthalocyanine films prefer the α phase.

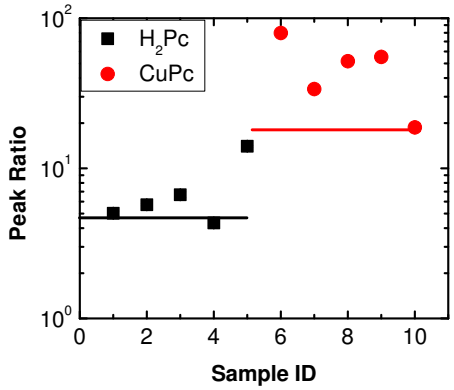

Figure IV.12: The experimental and theorectical results of the intensity ratio of the 1^{st} order diffraction peak to the 2^{nd} order diffraction peak for H_2Pc and CuPc films.

IV.B.5 The effect of the tilt angle

Besides the phase cancellation between the center atom and the rest of the phthalocyanine ring, the tilt angle tunes the spatial range of the electron density along the momentum transfer direction, which causes additional phase cancellation. Although an arbitrary tilt angle of the molecules in a phthalocyanine thin film cannot be realized experimentally, we are still able to study how the XRD profiles change as a function of the tilt angle theorectically. Figure IV.13(a) shows how H_2Pc differs from CuPc, including in both cases the background of the sapphire substrate. The intensities of the 1^{st} order peak for both cases increase steadily. The intensity of CuPc is higher than that of H_2Pc. The smallest difference

between these compounds appears when the tilt angle equals 90°. The intensity of the 2^{nd} order peak has a more complicated dependence on angle; there is a minimum between low angles and high angles, indicating that the scattering factors of the phthalocyanine ring and the center atom cancels out the most in this range. Figure IV.13(b) plots the peak ratio of the first two peaks against the tilt angle. It is clear that the difference between H_2Pc and CuPc reaches its maximum as the molecule stand straight up. As the tilt angle increases, the distinction between the two compounds diminishes. When the molecule lies flat, there is no detectable difference between these two compounds. Note that the diffraction with a tilt angle at 90° is equivalent to the approximation that all atoms in the molecule are placed at the same site so that the molecule can be treated as an isotropic particle without internal structure (model B)). The same conclusion can be obtained with other metallophthalocyanine compounds.

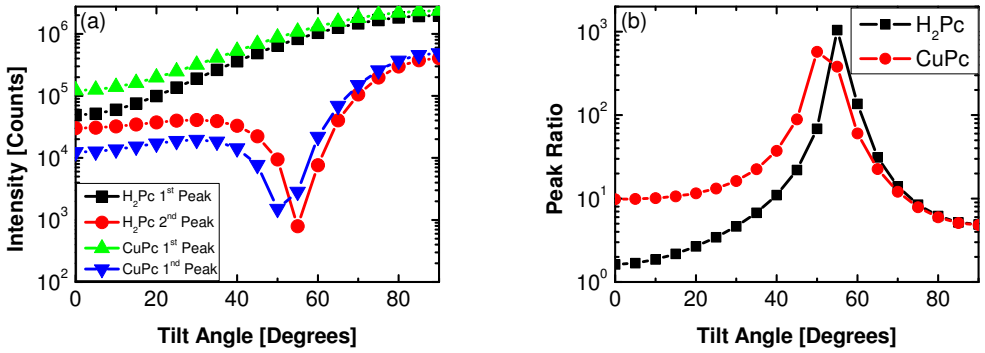

Figure IV.13: (a) The intensity of the 1^{st} order and 2^{nd} order diffraction peaks of H_2Pc and CuPc films and (b) the intensity ratio of the 1^{st} order diffraction peaks to the 2^{nd} order diffraction peaks as the function of the molecular tilt angle.

IV.B.6 The effect of the substrate

In the discussion above, the substrate gap Δ is defined in Figure IV.1. The diffraction background from the sapphire substrate is included, and Δ is kept constant at half of the d-spacing of a phthalocyanine monolayer. In fact, the

magnitude of the peak ratio amy also be affected by phase cancellation between the phthalocyanine thin film and the substrate. This cancellation is sensitive to the substrate gap Δ. We may ask the question: "to what extent does the substrate gap affect the intensity ratio of the 1^{st} to 2^{nd} order peaks?" The answer to this question determines whether our previous remarks are generally true or only true for very special circumstances.

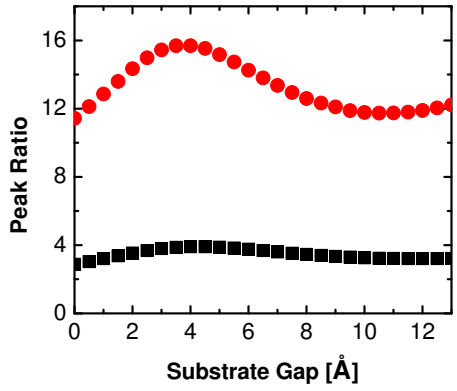

Figure IV.14: The intensity ratio of the 1^{st} and 2^{nd} order diffraction peaks as the function of the substrate gap. Black square and red circle refer to the results for H_2Pc and CuPc calculated using model C.

Figure IV.14 shows how the intensity ratio of the 1^{st} order peak to the 2^{nd} order peak changes as a function of the substrate gap. The maximum and the minimum values deviates from the average value by less than 20%. Therefore the uncertainty due to the substrate background must be less than 20% and is not enough to disapprove our previous conclusions.

IV.B.7 The tilt angle relaxation

In the previous discussion, we assume that the tilt angles in all monolayers are the same. Some studies [73] claim that the 1^{st} phthalocyanine monolayer lies parallel to the substrate surface and the rest of the monolayers have a tilt angle same as the bulk a phase. Sakurai suggests that the tilt angles of the first several

monolayers probably experience a gradual relaxation. [114, 115] It is of importance to know how the tilt angle relaxation modifies the XRD profiles.

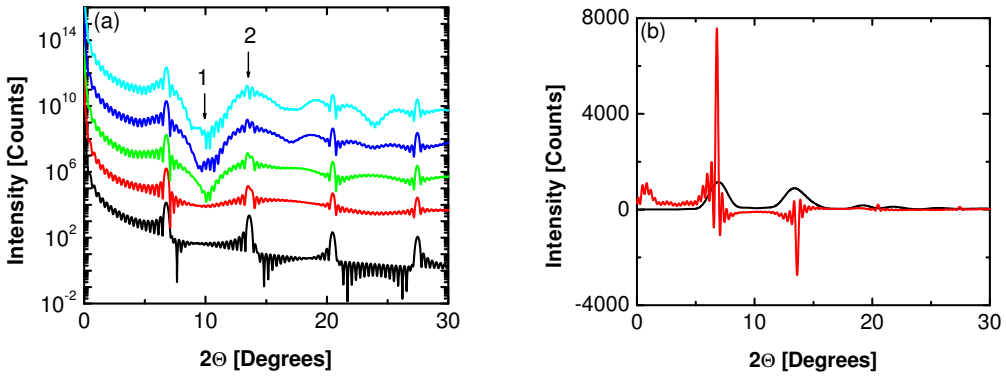

Figure IV.15: (a) The XRD profiles for four phthalocyanine films including the tilt angle relaxation. From the bottom to the top, the number of the relaxation monolayers is 0, 1, 2 and 4 in order. Two arrows point to the features discussed in the main text. (b) The first (black) and second (red) terms of the deviation from the thin film case, as defined in Equaion IV.8 when the number of the relaxation equals 4.

To reach this goal, we need to make a slight change to the theory discussed in Section IV.A. The revised version of Equation IV.5 is written as

$$I\left(\mathbf{Q},\{\theta\}\right)=corr\left\langle \begin{array}{c}\left(\sum_{m=0}^{N-1}F_{m}^{\mathrm{Cell}}\left(\mathbf{Q},\theta_{m}\right)e^{iQm\Lambda}+F^{\mathrm{Sub}}\left(\mathbf{Q}\right)\right)^{*}\\ \times\left(\sum_{m=0}^{N-1}F_{n}^{\mathrm{Cell}}\left(\mathbf{Q},\theta_{n}\right)e^{iQn\Lambda}+F^{\mathrm{Sub}}\left(\mathbf{Q}\right)\right)\end{array}\right\rangle \qquad \text{(IV.7)}$$

where the scattering factor for each monolayer is tilt-angle-dependent. $\{\theta\}$ represents a series of tilt angles of the monolayers from bottom to top. Let's assume the tilt angle relaxes gradually from 90° to 26° in a linear behavior. For example, if the relaxation occurs over the first three layers, the tilt angles of 1^{st}, 2^{nd}, 3^{rd} and 4^{th} layers are chosen as 90°, 68.67°, 47.33°, and 26°. Then we can examine the corresponding XRD profiles as the number of the relaxation monolayers varies. This result is given in Figure IV.15(a). Here we do not include the discrete roughness for it is irrelevant to this issue. Two features are identified with arrows 1 and 2. As the number of the relaxation monolayers increases, a valley is formed between

the 1^{st} and the 2^{nd} order peaks. The 2^{nd} order peak also transforms from a single peak to a double peak. Broad shoulders are also found in the immediate vicinity of each Bragg peak. To understand why there are such differences in the XRD profiles, we regroup the terms in Equation IV.7 as

$$\begin{aligned} I(\mathbf{Q}) &= corr\left\langle \begin{bmatrix} \left(\sum_{m=0}^{N-1} F^{\text{Cell}}(\mathbf{Q})\, e^{iQm\Lambda} + F^{\text{Sub}}(\mathbf{Q})\right) \\ + \sum_{m=0}^{N-1} \left(F_m^{\text{Cell}}(\mathbf{Q},\theta_m) - F^{\text{Cell}}(\mathbf{Q})\right) e^{iQm\Lambda} \end{bmatrix}^* \right. \\ &\quad \left. \times \begin{bmatrix} \left(\sum_{n=0}^{N-1} F^{\text{Cell}}(\mathbf{Q})\, e^{iQn\Lambda} + F^{\text{Sub}}(\mathbf{Q})\right) \\ + \sum_{n=0}^{N-1} \left(F_n^{\text{Cell}}(\mathbf{Q},\theta_n) - F^{\text{Cell}}(\mathbf{Q})\right) e^{iQn\Lambda} \end{bmatrix} \right\rangle \\ &= corr\left[\left\langle \left|F_1(\mathbf{Q})\right|^2\right\rangle + \left\langle \left|F_2(\mathbf{Q},\{\theta\})\right|^2\right\rangle + 2\text{Re}\left(\left\langle F_1^*(\mathbf{Q})\, F_2(\mathbf{Q},\{\theta\})\right\rangle\right)\right] \end{aligned} \tag{IV.8}$$

where $\left\langle \left|F_1(\mathbf{Q})\right|^2\right\rangle = \left\langle \left|\sum_{m=0}^{N-1} F^{\text{Cell}}(\mathbf{Q})\, e^{iQm\Lambda} + F^{\text{Sub}}(\mathbf{Q})\right|^2 \right\rangle$ is the Bragg diffraction term from a film without angular distortion, $\left\langle \left|F_1(\mathbf{Q})\right|^2\right\rangle$ is the same as Equation IV.5, the other terms, where

$$\left\langle \left|F_2(\mathbf{Q},\{\theta\})\right|^2\right\rangle = \left\langle \left|\sum_{m=0}^{N-1} \left(F_m^{\text{Cell}}(\mathbf{Q},\theta_m) - F^{\text{Cell}}(\mathbf{Q})\right) e^{iQm\Lambda}\right|^2 \right\rangle$$

and

$$2\text{Re}\left(\left\langle F_1^*(\mathbf{Q})\, F_2(\mathbf{Q},\{\theta\})\right\rangle\right) = 2\text{Re}\left(\left\langle \begin{array}{l} \left(\sum_{m=0}^{N-1} F^{\text{Cell}}(\mathbf{Q})\, e^{iQm\Lambda} + F^{\text{Sub}}(\mathbf{Q})\right)^* \\ \times \left(\sum_{n=0}^{N-1} \left(F_n^{\text{Cell}}(\mathbf{Q},\theta_n) - F^{\text{Cell}}(\mathbf{Q})\right) e^{iQn\Lambda}\right) \end{array} \right\rangle\right)$$

show the deviation from the ideal film. $\left\langle \left|F_1(\mathbf{Q})\right|^2\right\rangle$ is the diffraction from the distorted structure subtracting the diffraction without distortion, which is always positive. $2\text{Re}\left(\left\langle F_1^*(\mathbf{Q})\, F_2(\mathbf{Q},\{\theta\})\right\rangle\right)$ reveals the interference between the ideal structure with the distorted structure. This term may be positive or negative. These extra terms show the nature of the diffuse scattering, given in Figure IV.15(b). The features in Figure IV.15(a) identified by the arrows are not observed in all experimental results. We believe that the tilt angle relaxation can only occur in the first monolayer; otherwise, the double-peak pattern would be observed.

IV.C Conclusion

The electron densities of different phthalocyanines differ only in the core. This subtle difference in the electron density profile can cause a huge difference in the x-ray diffraction profile over a larger scale in momentum space. The phase cancellation between the central metal atom and the surrounding organic rings of the molecule is an essential part of the diffraction profile for layer-stacking organic thin films. Without considering the surrounding organic rings, the ratio of the 1^{st} to 2^{nd} order diffraction peaks would be a constant for all compounds in the phthalocyanie family. The experimental data shows a significant difference in the peak ratio between H_2Pc and CuPc. This confirms that the models which neglect the phase cancellation between the center atom and the aromatic rings are inaccurate.

The study on the molecular tilt angle reveals that the spatial range of the electron density of the anisotropic planar molecules is crucial in the diffraction behavior from crystalline thin films with precisely defined layer structure. The peak ratio between the 1^{st} and the 2^{nd} order peaks decreases as the electron density is confined to a smaller area. So the peak ratio between these peaks helps to determine (A) the core electron density of the molecule, and (B) the tilt angle.

The study on the substrate issue shows that the substrate gap increases or reduces the intensity ratio of the 1^{st} and the 2^{nd} order peaks by less than 20%. Thus, our previous conclusions are still true when the substrate effect is included.

Finally, a simple model to include the tilt angle relaxation suggests that only the first monolayer can lie flat on the substrate; all the other monolayers are tilted at the same angle if we assume a linear relaxation profile of the tilt angles. The complicated diffraction profiles resulting from Equation IV.8 suggest a new type of diffuse scattering which is not related to the distorted lattice structure but rather related to the distorted tilt angle distribution.

IV.D Acknowledgement

This work was supported by AFOSR MURI # F49620-02-1-0288.

V

Angular distribution and lateral grain size of phthalocyanine films

We have provided an extensive discussion on the x-ray diffraction from a phthalocyanine thin film using a one-dimensional model incorporating both the lattice and molecular structures. The study focuses on how the center atom and the extended electron density influence the XRD profile. Unusual features such as the different peak ratio and the complication from the tilt angle relaxation were considered. We intentionally neglected the lateral structural properties of the phthalocyanine film such as the in-plane texture and the lateral grain size. We also excluded the effects of angular misalignment of the $(h00)$ direction of the phthalocyanine crystallites with the normal to the substrate plane.

Studies show that the ordered structural domains of the very first H_2Pc layers may be formed on InSb (111) substrates. The H_2Pc molecules can be aligned in an either hexagonal or rectangular array. [116] In-plane rocking curves confirm that the CuPc crystallites are aligned along preferred directions parallel to the direction at which the substrates are rubbed. [117, 118] Similar in-plane order in different systems is reported by other groups. [119, 120, 121] On the other hand, random azimuthal orientation of the phthalocyanine crystallites is also reported. [62]

Uniaxial anisotropy is detected in OMBD phthalocyanine thin films using IR spectroscopy and ellipsometry. [122, 123] Similar uniaxial anisotropy is also reported in spin coated phthalocyanine films. [124] Similar phenomena have been observed in some other systems such as LB films, [125] metal films, [126] and liquid crystals. [127, 128, 129]

Daillant gave a general review on the x-ray diffraction study of ordered (uniaxial or textured) films and structures. [130] A broad range of topics on texture and anisotropy were discussed by Wenk. [131] Wenk pointed out that the Rietveld method can be expanded to include texture analysis and that in a textured material, there are systematic intensity deviations from those observed in a randomly oriented powder. However, the texture and anisotropy of crystalline thin films with controlled out-of-plane thickness (as in the family of phthalocyanines, porphyrins and perylene-3,4,9,10-tetracarboxylic-3,4,9,10-dianhydrides (PTCDAs)) has not been studied extensively. In this chapter, we propose a simple model for studying how the distribution of angles off the preferred axis and lateral grain size affect the rocking curves and the diffraction profiles. We are not attempting to derive a general framework to deal with all similar problems. Instead, we want to identify some essential features and determine how these features are manifested in the diffraction profiles. The issue of sampling population of the simulation is also addressed.

V.A Fundamental concepts and the three-dimensional XRD model

V.A.1 Two-coordinate systems and the Euler rotation

The orientation of a vector is usually given by two orthogonal directional angles. To determine the spatial arrangement of a rigid body, one more angle is needed to define the rotation about the axis which is determined by the polar and azimuthal angles. A two-circle goniometer cannot exhaust all possible orientations

of a specimen for this reason. A four-circle goniometer was developed to compensate for the shortcomings of the two-circle goniometer so that all possible rotations of a specimen can be measured.

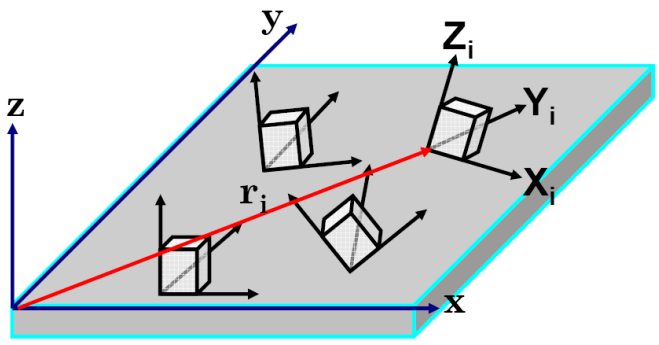

Figure V.1: The specimen frame (x, y, z) and the local frame (X_i, Y_i, Z_i) for the i^{th} crystallite.

The coordinate system used by the Euler cradle of an XRD instrument is that of the specimen coordinate. The two axes in the sample plane are usually called the x- and y- axes, and the z- axis is usually vertical to the sample surface. Another local coordinate system is introduced to describe the smaller-scaled structures such as domains, grains or crystallites. This coordinate system is fixed to the structure which is illustrated in Figure V.1. These two frames are related by a three-step rotation which is called the Euler rotation. There are totally 12 ways to define the Euler rotation and we keep the $z - x' - z''$ convention [132] which is illustrated in Figure V.2.

Assume we have a momentum transfer $\mathbf{Q}$, which is identified by $(\mathrm{Q_x}\ \mathrm{Q_y}\ \mathrm{Q_z})$ in the specimen coordinates. This same momentum vector can be reformulated as

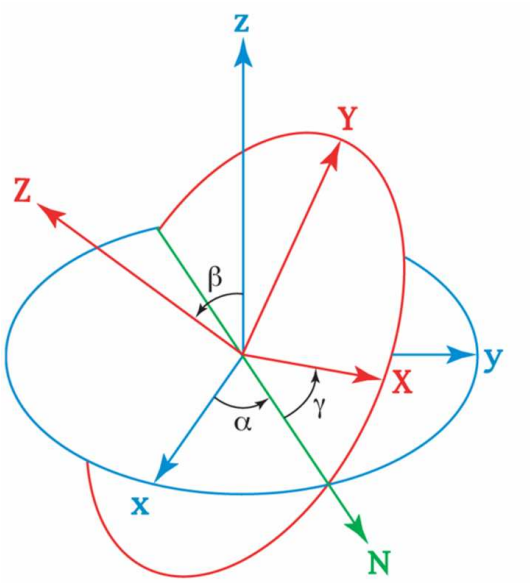

Figure V.2: The schematic diagram shows the Euler rotation by $z - x' - z''$ convention (The three-step rotation is not shown here, Ref. [132] gives a detailed description). The capital lettered frame is the local frame; and the lower lettered frame is the specimen frame.

$(\mathrm{Q}''_{\mathrm{x}}\,\mathrm{Q}''_{\mathrm{y}}\,\mathrm{Q}''_{\mathrm{z}})$ using the local coordinates

$$
\begin{aligned}
\mathbf{Q} &= \begin{pmatrix} \mathrm{Q_x} & \mathrm{Q_y} & \mathrm{Q_z} \end{pmatrix} \begin{pmatrix} \hat{\mathrm{i}} \\ \hat{\mathrm{j}} \\ \hat{\mathrm{k}} \end{pmatrix} \\
&= \begin{pmatrix} \mathrm{Q_x} & \mathrm{Q_y} & \mathrm{Q_z} \end{pmatrix} \hat{\mathrm{R}}^{-1}(\alpha;\mathbf{z})\,\hat{\mathrm{R}}^{-1}(\beta;\mathbf{x}')\,\hat{\mathrm{R}}^{-1}(\gamma;\mathbf{z}'') \\
&\quad \times \hat{\mathrm{R}}(\gamma;\mathbf{z}'')\,\hat{\mathrm{R}}(\beta;\mathbf{x}')\,\hat{\mathrm{R}}(\alpha;\mathbf{z}) \begin{pmatrix} \hat{\mathrm{i}} \\ \hat{\mathrm{j}} \\ \hat{\mathrm{k}} \end{pmatrix} \\
&= \begin{pmatrix} \mathrm{Q}''_{\mathrm{x}} & \mathrm{Q}''_{\mathrm{y}} & \mathrm{Q}''_{\mathrm{z}} \end{pmatrix} \begin{pmatrix} \hat{\mathrm{i}}'' \\ \hat{\mathrm{j}}'' \\ \hat{\mathrm{k}}'' \end{pmatrix}
\end{aligned}
\tag{V.1}
$$

so that the three coordinates in the local frame can be written as

$$\begin{aligned}\begin{pmatrix} \mathrm{Q}_\mathrm{x}'' & \mathrm{Q}_\mathrm{y}'' & \mathrm{Q}_\mathrm{z}'' \end{pmatrix} &= \begin{pmatrix} \mathrm{Q}_\mathrm{x} & \mathrm{Q}_\mathrm{y} & \mathrm{Q}_\mathrm{z} \end{pmatrix} \hat{\mathrm{R}}^{-1}(\alpha;\mathbf{z})\,\hat{\mathrm{R}}^{-1}(\beta;\mathbf{x}')\,\hat{\mathrm{R}}^{-1}(\gamma;\mathbf{z}'') \\ &= \begin{pmatrix} \mathrm{Q}_\mathrm{x} & \mathrm{Q}_\mathrm{y} & \mathrm{Q}_\mathrm{z} \end{pmatrix} \begin{pmatrix} \mathrm{cos}\alpha\mathrm{cos}\gamma & -\mathrm{cos}\beta\mathrm{cos}\gamma\mathrm{sin}\alpha & \mathrm{sin}\alpha\mathrm{sin}\beta \\ -\mathrm{cos}\beta\mathrm{sin}\alpha\mathrm{sin}\gamma & -\mathrm{cos}\alpha\mathrm{sin}\gamma & \\ \mathrm{cos}\gamma\mathrm{sin}\alpha & \mathrm{cos}\alpha\mathrm{cos}\beta\mathrm{cos}\gamma & -\mathrm{cos}\alpha\mathrm{sin}\beta \\ +\mathrm{cos}\alpha\mathrm{cos}\beta\mathrm{sin}\gamma & -\mathrm{sin}\alpha\mathrm{sin}\gamma & \\ \mathrm{sin}\beta\mathrm{sin}\gamma & \mathrm{cos}\gamma\mathrm{sin}\beta & \mathrm{cos}\beta \end{pmatrix}\end{aligned} \tag{V.2}$$

Equation V.2 gives the Euler rotation, which is an element of the $\mathcal{SO}(3)$ group. We can further define the orientation probability function (OPF) which is generally expressed by the Euler angle series expansion of harmonic functions

$$g(\alpha,\beta,\gamma) = \sum_{lmn} C_{lmn} Y_{lm}(\alpha,\beta)\, e^{in\gamma} \tag{V.3}$$

where the Jacobian is written as $\frac{1}{8\pi^2}\sin\beta \mathrm{d}\alpha\mathrm{d}\beta\mathrm{d}\gamma$. Equation V.3 is usually applied to a system with central symmetry, where the physical quantities can also be expressed using harmonic functions. In this case the equations describing these quantities can be reduced to the sum of the coefficients in Equation V.3 by the orthogonality relation and the completeness relation.

V.A.2 The diffraction from a phthalocyanine cuboid block with finite size

The OMBD phthalocyanine films are usually identified as having a quasi-orthorhombic lattice, and the lattice constants are given in Table V.1. The diffraction amplitude from a phthalocyanine cuboid-shape crystallite can be written as

$$\begin{aligned} F^{Cuboid}(\mathbf{Q}) &= \sum_{n_1=0}^{N_1-1}\sum_{n_2=0}^{N_2-1}\sum_{n_3=0}^{N_3-1} F^{UC}(\mathbf{Q})\, e^{i\mathbf{Q}\cdot\mathbf{l}(n_1 n_2 n_3)} \\ &= F^{UC}(\mathbf{Q}) \prod_{i=1}^{3} \frac{\sin\left(\frac{N_i Q_i l_i}{2}\right)}{\sin\left(\frac{Q_i l_i}{2}\right)} e^{i(N_i-1)Q_i l_i} \end{aligned} \tag{V.4}$$

where $F^{UC}(\mathbf{Q})$ is the structural factor of a unit cell, and $Q_i \in \{Q_x, Q_y, Q_z\}$ and $l_i \in \{b, c, a\}$, so that the (010), (001), and (100) axes are fixed to the local frame.

V.A.3 The ensemble of phthalocyanine crystallites and the averaging strategy

As we mentioned, the phthalocyanine thin films fabricated using the OMBD method usually show a well defined layered structure, and the layer stacking direction is the (h00) direction in the α phase lattice. Including the lateral structure, the film is thought of as an ensemble of phthalocyanine crystallites with their (h00) axes aligned with the layer stacking direction.

According to Equations V.2 and V.4, the diffraction from the ith crystallite is given by

$$\begin{aligned} F^i(\mathbf{Q}) &= F^{Cuboid}(\mathbf{Q})\, e^{i\mathbf{Q}\cdot\mathbf{r}_i} \\ &= \left(F^{UC}(\mathbf{Q}'') \prod_{i=1}^{3} \frac{\sin\left(\frac{N_i Q_i'' l_i}{2}\right)}{\sin\left(\frac{Q_i'' l_i}{2}\right)} e^{i(N_i-1)Q_i'' l_i} \right) e^{i\mathbf{Q}\cdot\mathbf{r}_i} \end{aligned} \tag{V.5}$$

where the term in the outer brackets has been transformed to the local frame. If we assume the diffraction to be completely coherent, the total contribution from the ensemble can be written as

$$\begin{aligned} \langle F(\mathbf{Q})\rangle &= \left\langle \left\langle \left(F^{UC}(\mathbf{Q}'') \prod_{i=1}^{3} \frac{\sin\left(\frac{N_i Q_i'' l_i}{2}\right)}{\sin\left(\frac{Q_i'' l_i}{2}\right)} e^{i(N_i-1)Q_i'' l_i} \right) e^{i\mathbf{Q}\cdot\mathbf{r}_i} \right\rangle \right\rangle \\ &= \int\int_S \rho(\mathbf{r})\, e^{i\mathbf{Q}\cdot\mathbf{r}} d\mathbf{r} \int_G \frac{g(\alpha,\beta,\gamma)}{s} \frac{\sin\beta d\alpha d\beta d\gamma}{8\pi^2} \left\langle F^{UC}(\mathbf{Q}'') \prod_{i=1}^{3} \frac{\sin\left(\frac{N_i Q_i'' l_i}{2}\right)}{\sin\left(\frac{Q_i'' l_i}{2}\right)} e^{i(N_i-1)Q_i'' l_i} \right\rangle_{N_1 N_2 N_3} \end{aligned} \tag{V.6}$$

in which the first integration is 2D surface intergral in the xy-plane, the second integration is 3D volume intergral in the space of three Euler angles and the third mean value is about the average crystal size. s is the projection of the crystallite onto the xy-plane.

Assuming the diffraction to be completely incoherent, the total contribu-

tion from the ensemble can be written as

$$\langle I(\mathbf{Q})\rangle = \left\langle\left\langle \left(I^{UC}(\mathbf{Q}'') \prod_{i=1}^{3} \left(\frac{\sin\left(\frac{N_i Q_i'' l_i}{2}\right)}{\sin\left(\frac{Q_i'' l_i}{2}\right)} \right)^2 \right)\right\rangle\right\rangle$$

$$= \int\int_S \rho(\mathbf{r})\, e^{i\langle \Delta\mathbf{r}\cdot\mathbf{Q}\rangle} d\mathbf{r} \int_G \frac{g(\alpha,\beta,\gamma)}{s} \frac{\sin\beta d\alpha d\beta d\gamma}{8\pi^2} \left\langle I^{UC}(\mathbf{Q}'') \prod_{i=1}^{3} \left(\frac{\sin\left(\frac{N_i Q_i'' l_i}{2}\right)}{\sin\left(\frac{Q_i'' l_i}{2}\right)} \right)^2 \right\rangle_{N_1 N_2 N_3} \tag{V.7}$$

In Equations V.6 and V.7, the inner bracket is spatial average, and the outer bracket is angular average. The main difference between Equations V.6 and V.7 is the averaging procedure: for the first equation we use an average diffraction amplitude, and for the second one we use an average diffraction intensity. It is impossible to solve such complicated equations, so some approximations must be made:

1. The projection of the crystallite to the xy-plane is dependent on the Euler angles. However for a uniaxially aligned system, where the crystallite bottom plane is nearly parallel to the substrate surface, s can be taken approximately as the bottom area of the crystallite, $N_2 b \times N_3 c$.

2. It is possible that the size of the crystallites is dependent on the orientation probability function and/or the spatial density. For simplification, we assume that these quantities are independent.

3. An in-plane uniformity is assumed so that we take $\rho(\mathbf{r}) = 1$. The in-plane coherence is accounted for by the grain size effect, so the averaging term relating to the xy-coordination can be neglected.

V.A.4 Modeling the size of crystallites

In Equations V.6 and V.7, we treat the N_1, N_2 and N_3 equally as free variables. During OMBD growth, the number of monlayers (N_1) is a controlled variable and the other two are usually uncontrolled variables. Thus, the diffraction

from an "average" crystallite is reduced to a simpler form:

$$\begin{aligned}\left\langle F^{Cuboid}\left(\mathbf{Q}''\right)\right\rangle &= F^{UC}\left(\mathbf{Q}\right)\left\langle \prod_{i=1}^{3}\frac{\sin\left(\frac{N_i Q_i'' l_i}{2}\right)}{\sin\left(\frac{Q_i'' l_i}{2}\right)}e^{i(N_i-1)Q_i'' l_i}\right\rangle \\ &= CF^{UC}\left(\mathbf{Q}''\right)\left(\sum_{N_1}\frac{\sin\left(\frac{N_1 Q_z'' a}{2}\right)}{\sin\left(\frac{Q_z'' a}{2}\right)}e^{i(N_1-1)Q_z'' a}e^{-\frac{(N_1-\bar{N}_1)^2}{2(\sigma N_1)^2}}\right) \\ &\times\left\langle\frac{\sin\left(\frac{N_2 Q_x'' b}{2}\right)}{\sin\left(\frac{Q_x'' b}{2}\right)}e^{i(N_2-1)Q_x'' b}\right\rangle\left\langle\frac{\sin\left(\frac{N_3 Q_y'' c}{2}\right)}{\sin\left(\frac{Q_y'' c}{2}\right)}e^{i(N_3-1)Q_y'' c}\right\rangle\end{aligned} \tag{V.8}$$

for coherent diffraction, or

$$\begin{aligned}\left\langle I^{Cuboid}\left(\mathbf{Q}''\right)\right\rangle &= I^{UC}\left(\mathbf{Q}\right)\left\langle \prod_{i=1}^{3}\left(\frac{\sin\left(\frac{N_i Q_i'' l_i}{2}\right)}{\sin\left(\frac{Q_i'' l_i}{2}\right)}\right)^2\right\rangle \\ &= CI^{UC}\left(\mathbf{Q}''\right)\left(\sum_{N_1}\left(\frac{\sin\left(\frac{N_1 Q_z'' a}{2}\right)}{\sin\left(\frac{Q_z'' a}{2}\right)}\right)^2 e^{-\frac{(N_1-\bar{N}_1)^2}{(\sigma N_1)^2}}\right) \\ &\times\left\langle\left(\frac{\sin\left(\frac{N_2 Q_x'' b}{2}\right)}{\sin\left(\frac{Q_x'' b}{2}\right)}\right)^2\right\rangle\left\langle\left(\frac{\sin\left(\frac{N_3 Q_y'' c}{2}\right)}{\sin\left(\frac{Q_y'' c}{2}\right)}\right)^2\right\rangle\end{aligned} \tag{V.9}$$

for incoherent diffraction (no diffuse scattering is considered here). In fact we realize that Equation V.9 is equivalent to the powder diffraction from a system composed of lamellar grains. It does not preserve as much phase information as Equation V.8 does. But we find that the average values of the last two terms in Equation V.8 diverge when $Q_x'' b = 2m\pi$ and $Q_y'' c = 2m\pi$, which makes the numerical simulation extremely unstable. So we still study the properties of this system in the incoherent diffraction limit using EquationV.9.

V.A.5 Modeling the orientation probability function

The complete form of the orientation probability function (OPF) is given by Equation V.3. Because the lattice structure is centrally symmetric, we are not able to use an expansion of harmonic functions to facilitate the simulation procedure. We assume that the OPF can be written as the product of three angular functions $g\left(\alpha,\beta,\gamma\right) = \mathrm{A}\left(\alpha\right)\mathrm{B}\left(\alpha,\beta\right)\Gamma\left(\alpha,\beta,\gamma\right)$, but this form is still too abstract for a numerical study. In considering the case where crystallites are randomly

orientated in xy-plane, we have $g(\alpha,\beta,\gamma) = \mathrm{B}(\alpha,\beta)\,\Gamma(\alpha,\beta,\gamma)$. To simulate the uniaxial behavior of the polar angle b, we can choose an elliptical distribution (The reasons are the following: 1) elliptical distribution has a very simple form and 2) the angular anisotropy can be represented by the eccentricity.)

$$\mathrm{B}(\beta) = \sqrt{\left(\frac{\cos^2\beta}{\sqrt{1-e_1^2}} + \sqrt{1-e_1^2}\sin^2\beta\right)\frac{1}{\pi}} \tag{V.10}$$

where e_1 is the eccentricity. A similar approximation can be applied to the last part of the OPF which gives

$$\Gamma(\gamma) = \sqrt{\left(\frac{\cos^2\gamma}{\sqrt{1-e_2^2}} + \sqrt{1-e_2^2}\sin^2\gamma\right)\frac{1}{\pi}} \tag{V.11}$$

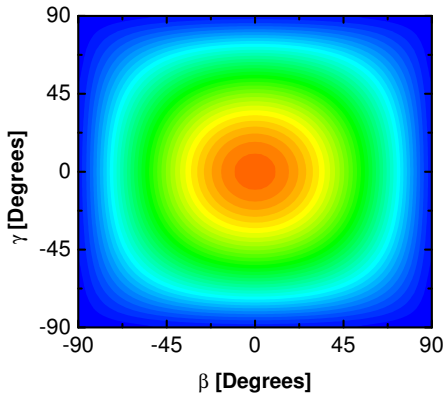

Figure V.3: The OPF mapping on the $\beta\gamma$-plane where e_1 and e_2 are 0.999 and 0.1.

Equation V.11 represents the anisotropy in the (010) direction, although it is often not as well defined as the anisotropy in the (100) direction in the phthalocyanine thin films due to correlation with the anisotropy of polar angle β. So we only study the behavior when $e_2 = 0$ which yields an isotropic distribution and when $e_2 \to 1$ which gives the extreme anisotropic limit. Figure V.3 gives an example of the OPF. It is obvious that our simple model represents the texture of an elliptical pillar in the three-dimensional space of Euler angles. When $e_1, e_2 = 0$, the model gives the diffraction profiles from a randomly oriented system. When

Table V.1: The eccentricity and its corresponding deviation angles defined in Equation V.12.

e_1	$\delta\alpha$
0	45°
0.9	23.55192°
0.99	8.02959°
0.999	2.56°
0.999 9	0.81021°
0.999 99	0.25623°
0.999 999	0.08103°
0.999 999 9	0.02562°
0.999 999 99	0.0081°
0.999 999 999	0.00256°

$e_1, e_2 = 1$, the model gives the XRD from a thin film where (100) direction is perpendicular to the surface plane, and the (010) direction is parallel to the surface plane. Our motivation is to discover what happens as the texture in the $\beta\gamma$-plane diffuses from a point to the whole plane.

The ratio of the short axis to the long axis characterizes the deviation angle from the long axis. The deviation angle is given by

$$\delta\alpha = \tan^{-1}(\sqrt{1 - e_1^2}) \tag{V.12}$$

which is demonstrated by Figure V.4, and some values are tabulated in Table V.1.

V.B The numerical result

V.B.1 The grain size effect

Assume that the number of monolayers is 20 (10 unit cells), and the number of monolayers along the c-axis ((001) direction) is also 20. It is commonly understood that the phthalocyanine grains are rod-like and the b-axis (or (010)

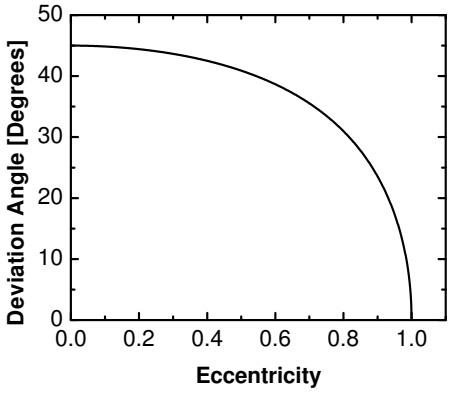

Figure V.4: The deviation angle as a function of the eccentricity. Some values are given in Table V.1.

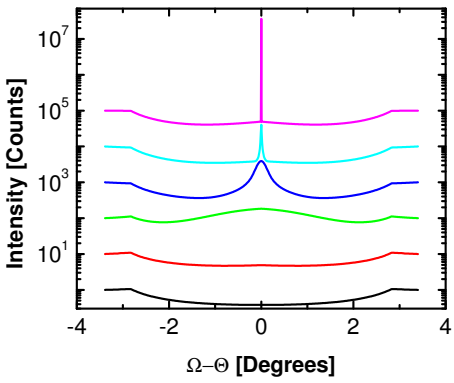

Figure V.5: The rocking curves vs. the in-plane coherence. From bottom to top, the numbers of the monolayers in the (010) direction are 2, 20, 200, 2 000, 20 000, and 200 000.

direction) is the elongated direction. So we take the number of monolayers along the b-axis as the variable. The rocking curves at 6.8°, which correspond to the 1^{st} order diffraction peak from the film, are given in Figure V.5. From bottom to top, the numbers of the monolayers on the b-axis (N_2) are 2, 20, 200, 2 000, 20 000, and 200 000. The average grain size of the crysallites here is determined by N_2 which also characterizes the in-plane coherence length. When the in-plane coherence length is short, only powder-like XRD rocking curves are found. As the in-plane coherence length exceeds about 2 000 times the d-spacing along b-axis, coherent diffraction features start to appear. The numerical study in the coherent diffraction regime suggests similar behavior, but the off-alignment tail is one nuance.

V.B.2 The angular anisotropy effect

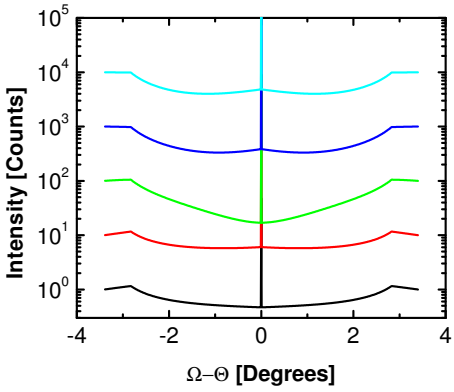

Figure V.6: The rocking curves when e_2= 0.999 999 999 for different eccentricities. From bottom to top, the eccentricities are 0, 0.99, 0.999 9, 0.999 999 and 0.999 999 999.

To exclude features from the short in-plane grain size, we assume that there is long in-plane coherence, when N_2 equals 200 000 and that there is a very sharp peak at 0°. By changing the eccentricity, we are tuning the angular anisotropy in the (100) direction (layer stacking direction). Figure V.6 shows how the rocking curves change. From bottom to top, e_1 is chosen from 0, 0.99 to

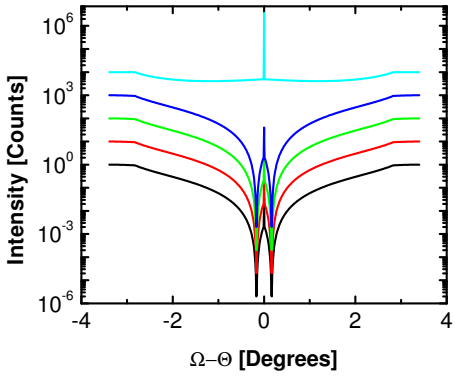

Figure V.7: The rocking curves when e_1= 0.999 999 999 for different eccentricities. From bottom to top, the eccentricities are 0, 0.99, 0.999 9, 0.999 999 and 0.999 999 999.

0.999 999 999. This covers the range from a film with the crystallites in random orientation to a virtually flat film. The randomly oriented film demonstrates a similar off-alignment tail as the film with short in-plane coherence. The relative height of the center peak vs. the off-alignment background decreases as the eccentricity decreases. Though the off-alignment tails in each case are quite different, the sharp center peaks always exist. This is inconsistent with the common belief that the rocking curve is the criterion to test the in-plane alignment. When dealing with the grain size effect, the elimination of in-plane coherence wipes out lateral crystalline features. However, a broad angular distribution maintains the crystalline features so that those almost vertically aligned crystallites still contribute to the center peak. The other eccentricity e_2 can be addressed in a similar way. We notice that the rocking curves as the function of e_2 (Figure V.7) show very complicated features. Increasing e_2 expands the space of Euler angles and creates two minima beside the center peak. This feature is decided by the OPF or model-related, thus lacks the experimental correspondence.

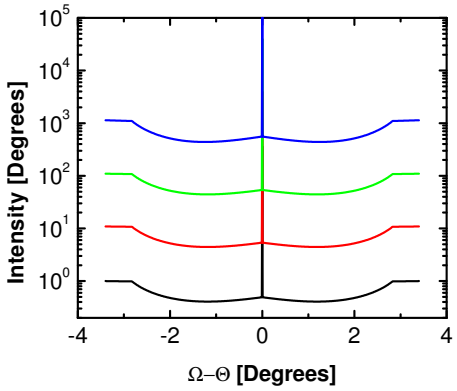

Figure V.8: The rocking curves in the (100) direction for different values of discrete surface roughness - 0%, 5%, 10% and 30%.

V.B.3 The surface discrete roughness

Figure V.8 shows the rocking curves for different values of surface discrete roughness. These curves are the same shape. Since we assume that the (100) surface is a totally uncorrelated stepped surface, this type of roughness does not impact the in-plane diffraction. Introducing surface correlation will result in more features on the rocking curve, which is beyond the scope of this work.

V.B.4 The profiles of normal diffraction

The normal XRD profiles ($\Theta - 2\Theta$ coupled scans) reflect the d-spacings of the possible structures in a thin film. It is straightforward to follow a similar procedure to that used for the simulation for the rocking curves (Equation V.9). Considering the three-dimensional space of Euler angles, if we choose 0.1° as the sampling step, the total population of the sampling reaches 729 000 000, which is impossible to simulate numerically. Reducing the sampling population usually degrades the result so that spurios peaks appear in the XRD profiles. Figure V.9 gives an example of the simulated XRD profiles of a phthalocyanine thin film composed of crystallites assuming that N_1, N_2, and N_3 are 20, 2 000 and 200, respectively. The noisy background prevents us from obtaining any meaningful

information.

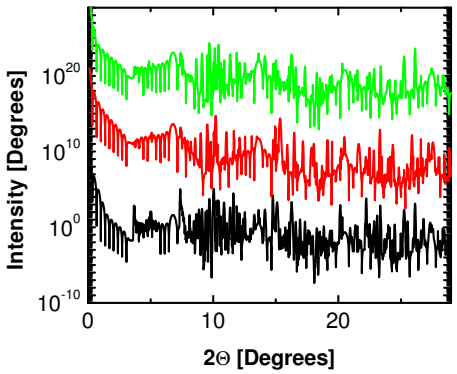

Figure V.9: The XRD profiles of phthalocyanine thin films with zero roughness from the full calculation simulations assuming N_1, N_2 and N_3 are 20, 2 000, 200, respectively.

If we restrict the freedom of rotation to one dimension, the numerical study can overcome the problem of under-population. Two special cases have been studied.

In the first case, we assume that the (010) axis is perfectly parallel to the substrate surface, and the (100) axis deviates from the out-of-plane direction, resulting in an elliptical distribution. Changing the elliptical eccentricity, we obtain the diffraction profiles with different deviation angles. Figure V.10(a) shows the results of a phthalocyanine thin film assuming N_1, N_2, and N_3 are 20, 200 and 60, respectively. We intentionally choose larger lateral size to amplify the effect from the lattice in the lateral direction. From bottom to top, the eccentricities are 0.0, 0.999 9 and 0.999 999 999. First of all, we identify the diffraction peaks, that do not belong to the (h00) series, such as (002), (202), (004), (006) and (402) etc. The intensities of the (002), (004) and (006) peaks change drastically while those of the (202) and (402) peaks are nearly constant. Plotting the intensity of the (200) and (006) peaks as the function of deviation angles (refer to Table V.1), we find that the intensity of the (200) peak increases as the deviation angle decreases and the intensity of the (006) peak decreases as the deviation angle decreases

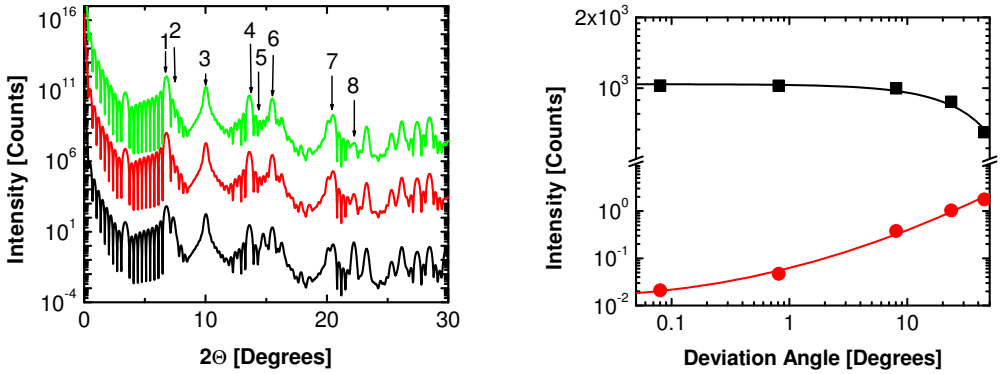

Figure V.10: (a) The XRD profiles of plain phthalocyanine thin films with elliptical eccentricities of 0.0, 0.999 9 and 0.999 999 999 when the (010) axis is parallel to the surfaces. ($N_1 = 20$, $N_2 = 200$ and $N_3 = 60$, zero surface roughness assumed. Arrows 1 - 8 point to the (200), (002), (202), (400), (004), (402) and (006) peaks, respectively.) (b) The intensities of the (200) diffraction peak (black) and the (006) diffraction peak (red) as functions of the deviation angle defined in Equation V.12.

(Figure V.10(b)).

Next, we assume that the (001) axis is perfectly parallel to the substrate surface. Following the same procedure, we obtain the diffraction profiles shown in Figure V.11(a) where the eccentricities are the same as above. Different series of diffraction peaks such as (020), (220) and (420) are found. The intensity of the (020) peak changes significantly in different curves. The intensities of the (200) and (020) peaks as functions of deviation angle are given in Figure V.11(b).

According to the results shown in Figures V.10(b) and V.11(b), the ratio between the ($h00$) peak intensity to that of the ($0k0$) or ($00l$) is the characteristic quantity that determines the polar angle deviation from the normal direction. Although the diffraction peaks labeled with mixed indices - ($hk0$), ($h0l$) and (hkl) - are also relevant to the misalignment, the intensity does not change as significantly as the ($0k0$) and ($00l$) series do.

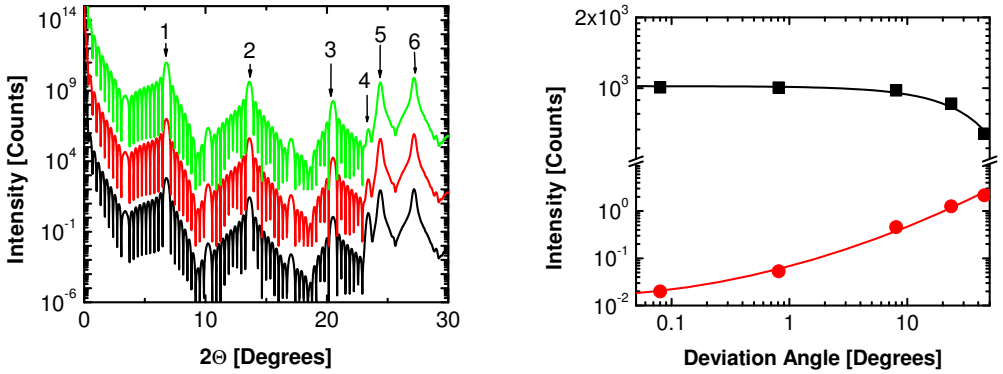

Figure V.11: (a) The XRD profiles of plain phthalocyanine thin films with elliptical eccentricities of 0.0, 0.999 9 and 0.999 999 999 when the (001) axis is parallel to the surfaces. ($N_1 = 20$, $N_2 = 200$ and $N_3 = 60$, zero surface roughness assumed. Arrows 1 - 6 point to the (200), (400), (600), (020), (220) and (420) peaks, respectively.) (b) The intensities of the (200) diffraction peak (black) and the (020) diffraction peak (red) as functions of the deviation angle defined in Equation V.12.

V.C Conclusion

A new model that considers the contribution from lateral structure and angular anisotropy is proposed. Our study shows that lateral coherence plays the most important role in rocking curves. By tuning the lateral coherence length or the grain size, the features from diffuse scattering and coherent diffraction can be reproduced. The peak width (FWHM) of the center peak in the rocking curves is mainly determined by the lateral grain size.

The angular anisotropy influences the rocking curve in a way that was previously misunderstood. The existence of the center peak, which reveals the crystalline nature of thin films, cannot be used to identify the extent to which the grains are off the normal axis. Deviation angles are related to the height of the center peak and affect the shape of the off-alignment tail. But, in general, it cannot be used to assess the deviation angle for the reason that the contribution from substrate and capping layer changes the diffraction intensity and the line shape. Because the rocking curve "picks" out a certain d-spacing from the diffraction

pattern (the diffraction related to other d-spacings does not complicate the features of rocking curves), the sampling population size in the numerical study does not play an important role.

The normal diffraction profiles show different shapes as the deviation angle changes. Due to the vast volume of the three-dimensional space of Euler angles, it is practically impossible to perform a complete numerical study. The results of two special cases, where the contribution from the substrate was ignored, suggest that the ratio of the $(h00)$ peak intensities to those of the $(0k0)$ or $(00l)$ peaks can quantitatively characterize the polar angular deviation from the normal direction. However, due to the low intensity of the $(0k0)$ and $(00l)$ series of diffraction peaks, the ratio can only be obtained only from an XRD system equipped with very strong beam source.

In brief, the FWHM of the center peak in rocking curves gives the lateral coherence length or the lateral grain size of the phthalocyanine thin film, and the ratio of the intensities from the diffraction peaks related to perpendicular lattice planes tells the uniaxial angular anisotropy of the phthalocyanine thin film. Neither of these features is available from the one-dimensional layer chain model discussed in Chapter IV.

V.D Acknowledgement

This work was supported by AFOSR MURI # F49620-02-1-0288.

VI

Ending remarks

As an x-ray physicist, I have a hope that someday a general XRD model will be developed for application to the most complicated problems in any physical system. But the reality is that such a catholicon is not possible, so we have to deal with complexity by introducing approximations. The philosophy that I have come to embrace during my Ph. D. study is that good theory usually focuses on the most important features and tries to make everything as simple as possible.

Physics, as a subject, serves to summarize the universality that exists across diverse systems and to specify general rules to fit a unique problem. Interesting results are found when uniqueness meets commonality.

In the first part of this work, a very general approach is applied to a very specific system. This gave us insight into the way that the interfacial layer in a III-V semiconductor superlattice and the annealing process affect the superlattice structure. We prove that there is a certain thickness of the interfacial layer as well as an annealing temperature range for optimal quality. These conclusions can be used to guide future fabrication.

In the second part of this work, we attempt to model a very specific system by including the molecular structural information. Such a study leads us to the conclusion that the electron density distribution greatly influences the specular diffraction profiles. It was previously considered impossible, but it now

seems that some very important structural information can be determined from the specular diffraction. Our effort to model a specific system results in a general understanding on a large number of similar systems. The study of uniaxially aligned crystalline phthalocyanine films indicates that there is a profound difference between the superposition of the phase factors and a pure geometrical averaging. In both cases, the diffraction is a result of the phase, although the phase cannot be observed directly.

In reflecting on the research questions addressed, we observed several interesting research topics. These would allow us to further evaluate and expand the findings of this dissertation.

In Chapters II and III, the SUPREX refinement method was used to characterize InAs/GaSb superlattices. The standard A/B model was chosen to reproduce the features in the XRD profiles. As a possibility for future work, a model including four layers in each modulation unit may give us better understanding of the structure of interfaces and how these interfaces influence the XRD profiles. Monte-Carlo method proves computational inefficient in simulating the XRD profiles of superlattices, but a hybrid model incorporating the analytical nature of standard A/B model and the non-deterministic nature of Monte-Carlo method may overcome this inefficiency.

In Chapters IV and V, direction calculation method was applied to study the structure of phthalocyanine thin films. Another possibility for future work, a refinement procedure based on this study may help us to obtain the structural parameters of these thin films from the XRD profiles. A similar approach may be applied to study the XRD profiles of some similar organic thin films with molecular anisotropy. In addition, a coherent scattering study of these thin films using a synchrotron source may give us better understanding of the out-of-plane and lateral coherence between phthalocyanine crystallites.

A

The x-ray scan configurations

The $\Theta/2\Theta$-coupled (Θ-2Θ) and Ω measurements can be performed using both two-circle and four-circle systems. The working principle of a $\Theta/2\Theta$-coupled scan is shown in Figure A.1. The sample is mounted at the center of the goniometer cradle and the plane determined by the incident and outgoing x-ray beams is perpendicular to the sample surface. The incident beam is directed at the sample surface at an angle Θ_i and the outgoing beam leaves the sample surface at an angle Θ_f; the total diffraction angle is 2Θ. The sample surface and the bisecting plane of the diffraction angle 2Θ form an angle Ω. The diffraction momentum transfer $\mathbf{Q}$ and the diffraction angle 2Θ are related by:

$$\mathbf{Q} = \frac{4\pi \sin\Theta}{\lambda_{x-ray}} \left(\hat{\mathbf{k}}_f - \hat{\mathbf{k}}_i \right) \tag{A.1}$$

A typical $\Theta/2\Theta$-coupled scan is usually taken when the misalignment angle Ω, which is defined as $\Omega = \frac{\Theta_i - \Theta_f}{2}$, equals 0. Off-aligned $\Theta/2\Theta$-coupled scan can also be performed, but this usually results in a far weaker signal.

Keeping the diffraction angle 2Θ constant, we obtain the diffraction spectrum as a function of Ω; this is called a rocking curve. The rocking curve tells us mixed information about the in-plane structure and out-of-plane structure. Rocking curves are also used to examine in-plane coherence length (often called lateral grain size) and angular misalignment between the crystallites within a sample.

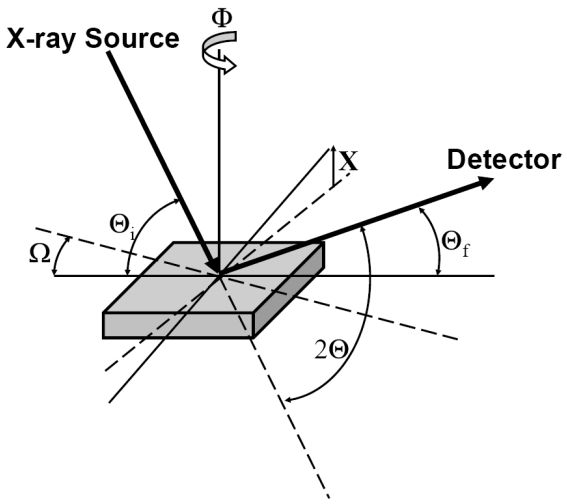

Figure A.1: A schematic diagram shows the four common scan modes using a four-circle XRD system.

Another commonly used scan mode is grazing incidence diffraction (GID). The GID method is a method that is based on $\Theta/2\Theta$-coupled scan when the incident and outgoing x-ray beams are close to the critical angle, and the beam plane is nearly parallel to the sample surface. This scan mode is applied to study the in-plane structure of the sample. First, the sample is aligned using a rocking curve scan at a very low diffraction angle. Then, the sample is tilted by changing the angle X defined in Figure A.1 so that the sample surface is almost perpendicular to the initial sample surface. Finally, an in-plane $\Theta/2\Theta$-coupled scan is performed.

The last common scan configuration is the Φ scan or azimuthal scan. This is performed by setting the tilt angle X of the goniometer cradle to a constant value appropriate for the off-normal reflections under study and varying the azimuthal angle Φ. The Φ scan usually tells us the in-plane texture and the symmetry of the in-plane two-dimensional lattice. Note that the last two modes can only be performed using a four-circle diffraction system.

B

Description of the SUPREX approach and applied models

SUPREX, or superlattice refinement by x-ray diffraction, was developed [40, 33, 39, 41] for quantitative structural refinement of superlattices and thin films from x-ray diffraction data. SUPREX is a "refinement" method, as opposed to a simulation, which provides accurate values for lattice parameters and structural disorder. In a refinement, the average atomic structure of the superlattice along with structural disorder are incorporated into a general kinematical diffraction model, which is used in conjunction with a nonlinear fitting algorithm to fit the entire x-ray diffraction profile. Both lattice constants and disorder parameters can be determined from this method. A detailed description of the method [33, 39, 41] is beyond the scope of this work, and the software is available as free download from http://ischuller.ucsd.edu/Suprex.html.

Both the homogeneous and symmetric strain model and the inhomogeneous and asymmetric strain model mentioned here are based on the standard A/B model included in the SUPREX software package. Since epitaxially grown crystalline InAs/GaSb superlattices with high quality were obtained, a crystalline-crystalline mode of the standard A/B model is selected. The "ideal" superlattice consists of repeated, alternating layers of A and B. In a "real" superlattice, the

different layers (A and B) are separated by some kind of an interface. Even if the "bulk" of each A and B layer is perfect, the interface can have imperfections from interdiffusion, discrete disorder, or continuous disorder (roughness). A schematic diagram (Figure B.1) shows how strain is introduced into one of the layers of the standard model. The number of monolayers of layer A is given as N_A. The quantities d_A, Δd_{A1}, Δd_{A2} are defined as the d-spacing in the center layer A, and the strain at the first monolayer nearest to the interface on the lower and upper sides, respectively. α is a constant that characterizes the exponential strain decay from the interface and is typically assumed to be 0.5. Equivalent terms are also defined for layer B. The d-spacings at three monolayers closest to the interface are given in Figure B.1. The average d-spacing of a constituent layer can be determined by the sum of d-spacings inside it ("thickness of one constituent layer") divided by the average number of monolayers:

$$\langle d \rangle = \frac{\left[\sum_{i=0}^{2} \Delta d_1 \exp(-i\alpha_1) + \sum_{i=0}^{2} \Delta d_2 \exp(-i\alpha_2) + Nd\right]}{N}. \tag{B.1}$$

The discrete roughness of each constituent layer is given as the standard deviation of the number of monolayers multiplied by the d-spacing, $\sigma_N d$. Chemical interdiffusion can be introduced into the standard model and a symmetric interdiffusion about the interface is assumed here. Two parameters determine the amount of interdiffusion and the interdiffusion depth. The thickness and average d-spacing of the interdiffusion layer were obtained from the refined values of strain profile and interdiffusion parameters.

The *inhomogeneous and asymmetric* strain model assumes bulk d-spacing at the center of each layer and a varying strain profile, which can be different at each interface. The *homogeneous and symmetric* strain model assumes that the d-spacing may be different from the bulk value but is constant throughout a layer.

In general, the structural refinement strategy can be divided into five major steps:

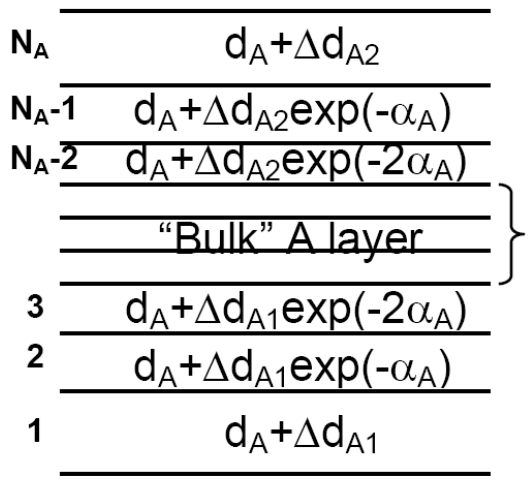

Figure B.1: A schematic diagram of the strain for a single constituent layer A of the superlattice used in the refinement.

1. Start by assuming a perfect superlattice structure. Using the nominal individual layer thicknesses, bulk lattice constant and modulation length derived from the intervals between satellite peaks, [41] an initial simulation profile is generated. Interdiffusion parameters are also introduced to reflect the additional contribution by the InSb-like interfacial layers.

2. A strain profile, representing the distortion near the interface between two layers is introduced. After this, the shape and intensity of the simulation greatly improves. Roughness is subsequently included to suppress the redundant oscillations and a Lorentzian doublet is added to the fitting profile to simulate the main GaSb buffer peak. The experimental curve is then initially simulated qualitatively, without attempting to reach the ultimate, smallest χ^2.

3. In addition to the expected GaSb features, our Te-doped GaSb wafers contained features related to the tungsten contamination, as is indicated by Arrow A in the bottom curve of Figure B.1. Satisfactory simulations can be achieved with the above approach except in the areas near these spectral features. To avoid complications from the presence of these features, we removed

the portions of the data containing these features by drawing an approximated background in their place. The data is then treated as a GaSb-buffer-free data set.

4. Further high accuracy fitting is carried out to the experimental data, by including a strain profile and thickness of the constituent layers to achieve the lowest possible fitting error χ^2. Once these fitting parameters are stable, the interdiffusion parameters are adjusted to reflect the local chemical intermixing and scattering factor change near the interfaces.

5. Structural parameters such as the individual average d-spacing, the statistical distribution of the thicknesses of the InAs and GaSb layers, and the thickness of the transitional interfacial layer are calculated.

C

Remarks on the discrete roughness of a superlattice

The effects of discrete layer thickness fluctuations can be modeled by assuming a discrete Gaussian variation of the number of atomic monolayers in each constituent layer, about an integer average value termed the discrete roughness. A comprehensive discussion on the discrete roughness can be found in the results of Sevenhans *et al.* [39] The diffraction from superlattice with discrete roughness is determined by the average value of each constituent layer according to the discrete Gaussian distribution and the inter-constituent layer correlation according to the same discrete roughness. This can be written as

$$\begin{aligned}
\left\langle F_{SL}\left(\mathbf{Q}\right)\right\rangle &= \left\langle \sum_{j=0}^{N-1} \left\{ \begin{array}{c} \left[F_A\left(\mathbf{Q}\right)\frac{1-e^{im\mathbf{Q}\cdot\mathbf{d}_A}}{1-e^{i\mathbf{Q}\cdot\mathbf{d}_A}} + F_B\left(\mathbf{Q}\right)\frac{1-e^{in\mathbf{Q}\cdot\mathbf{d}_B}}{1-e^{i\mathbf{Q}\cdot\mathbf{d}_B}}e^{i\mathbf{Q}\cdot\left(m\mathbf{d}_A+\boldsymbol{\Delta}_{AB}\right)}\right] \\ \times e^{i\mathbf{Q}\cdot\left(j\left(m\mathbf{d}_A+\boldsymbol{\Delta}_{AB}+n\mathbf{d}_B+\boldsymbol{\Delta}_{BA}\right)\right)} \end{array} \right\} \right\rangle_{(m,n)} \\
&= \sum_{j=0}^{N-1} \left\{ \begin{array}{c} \left[F_A\left(\mathbf{Q}\right)\left\langle\frac{1-e^{im\mathbf{Q}\cdot\mathbf{d}_A}}{1-e^{i\mathbf{Q}\cdot\mathbf{d}_A}}\right\rangle_m + F_B\left(\mathbf{Q}\right)\left\langle\frac{1-e^{in\mathbf{Q}\cdot\mathbf{d}_B}}{1-e^{i\mathbf{Q}\cdot\mathbf{d}_B}}\right\rangle_n e^{i\mathbf{Q}\cdot\left(\bar{m}\mathbf{d}_A+\boldsymbol{\Delta}_{AB}\right)}\right] \\ \times e^{i\mathbf{Q}\cdot\left(j\left(\bar{m}\mathbf{d}_A+\boldsymbol{\Delta}_{AB}+\bar{n}\mathbf{d}_B+\boldsymbol{\Delta}_{BA}\right)\right)} \end{array} \right\} \\
&= \sum_{j=0}^{N-1} \left\{ \begin{array}{c} \left[\begin{array}{l} F_A\left(\mathbf{Q}\right)\sum\limits_{m=m_{\min}}^{m_{\max}}\left(\frac{1-e^{im\mathbf{Q}\cdot\mathbf{d}_A}}{1-e^{i\mathbf{Q}\cdot\mathbf{d}_A}}P_A\left(m\right)\right) \\ +F_B\left(\mathbf{Q}\right)\sum\limits_{n=n_{\min}}^{n_{\max}}\left(\frac{1-e^{in\mathbf{Q}\cdot\mathbf{d}_B}}{1-e^{i\mathbf{Q}\cdot\mathbf{d}_B}}P_B\left(n\right)\right)e^{i\mathbf{Q}\cdot\left(\bar{m}\mathbf{d}_A+\boldsymbol{\Delta}_{AB}\right)} \end{array} \right] \\ \times e^{i\mathbf{Q}\cdot\left(j\left(\bar{m}\mathbf{d}_A+\boldsymbol{\Delta}_{AB}+\bar{n}\mathbf{d}_B+\boldsymbol{\Delta}_{BA}\right)\right)} \end{array} \right\}
\end{aligned} \tag{C.1}$$

where $\bar{m}$, $\bar{n}$ are the mean values of the numbers of atomic monolayers of the two constituent layers, and the other parameters are similar as the definitions in Ref [39]. The evaluation of the intensity requires extra terms to account for the inter-constituent-layer correlation. This approach is well-defined and straightforward to x-ray physicists.

However, the theoretical physicists working on the band calculation of the superlattices and multiplayer structures prefer a "supercell" calculation. Instead of calculating the average structure and the correlation from the discrete roughness, they would rather evaluate the diffraction from an arbitary supercell structure first, and then take the statistical average from all possible supercells. Thus the average value of the diffraction amplitude from all possible arbitury supercells can be written as

$$\begin{aligned}\left\langle F_{SL}\left(\mathbf{Q}\right)\right\rangle &= \left\langle \sum_{j=0}^{N-1} \left\{ \begin{array}{l} \left[F_A\left(\mathbf{Q}\right)\frac{1-e^{im(j)\mathbf{Q}\cdot\mathbf{d}}}{1-e^{i\mathbf{Q}\cdot\mathbf{d}}} + F_B\left(\mathbf{Q}\right)\frac{1-e^{in(j)\mathbf{Q}\cdot\mathbf{d}}}{1-e^{i\mathbf{Q}\cdot\mathbf{d}}}e^{i\mathbf{Q}\cdot(m(j)\mathbf{d}_A+\mathbf{\Delta}_{AB})}\right] \\ \times e^{i\mathbf{Q}\cdot\left(\sum_{k=0}^{j} m(k)\mathbf{d}_A+j\cdot\mathbf{\Delta}_{AB}+\sum_{k=0}^{j} n(k)\mathbf{d}_B+j\cdot\mathbf{\Delta}_{BA}\right)} \end{array} \right\} \right\rangle \\ &= \sum_{\{m(j)\}=m_{\min}}^{m_{\max}} \sum_{\{n(j)\}=n_{\min}}^{n_{\max}} \left\{ \sum_{j=0}^{N-1} \left\{ \begin{array}{l} \left[\begin{array}{l} F_A\left(\mathbf{Q}\right)\frac{1-e^{im(j)\mathbf{Q}\cdot\mathbf{d}}}{1-e^{i\mathbf{Q}\cdot\mathbf{d}}}+ \\ F_B\left(\mathbf{Q}\right)\frac{1-e^{in(j)\mathbf{Q}\cdot\mathbf{d}}}{1-e^{i\mathbf{Q}\cdot\mathbf{d}}}e^{i\mathbf{Q}\cdot(m(j)\mathbf{d}_A+\mathbf{\Delta}_{AB})} \end{array} \right] \\ \times e^{i\mathbf{Q}\cdot\left(\sum_{k=0}^{j} m(k)\mathbf{d}_A+j\cdot\mathbf{\Delta}_{AB}+\sum_{k=0}^{j} n(k)\mathbf{d}_B+j\cdot\mathbf{\Delta}_{BA}\right)} \end{array} \right\} \right. \\ &\qquad \left. \times P\left(\left\{m\left(j\right)\right\},\left\{n\left(j\right)\right\}\right) \right\}\end{aligned} \tag{C.2}$$

All possibilities of the combination of $\{m\left(j\right) : m\left(j\right) \in [m_{\min}, m_{\max}]\}$ and $\{n\left(j\right) : n\left(j\right) \in [n_{\min}, n_{\max}]\}$ when $j \in [0, N-1]$ are exhausted, and $P\left(\left\{m\left(j\right)\right\},\left\{n\left(j\right)\right\}\right)$ is the joint probability of a possible supercell structure in this huge ensemble. Equation C.2 looks simple but proves very difficult to evaluate numerically. The reason is that the number of terms for all the possible combinations is $\left[\left(m_{\max}-m_{\min}+1\right)\left(n_{\max}-n_{\min}+1\right)\right]^{N-1}$, which becomes extremely large as N increases. To give an idea how large it can be, we assume $\left(m_{\max}-m_{\min}+1\right)\left(n_{\max}-n_{\min}+1\right)=4$ and $N=20$, then there are 549 755 813 888 terms given by Equation C.2!!! In fact, the population increases exponentially as

the number of the bilayers increases so that the numerical study of Equation C.2 is typically identified as a problem with computational complexity *NP* and should not be pursued.

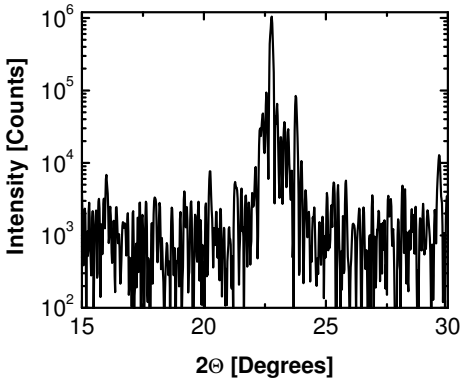

Figure C.1: Simulation using Monte-Carlo method by 1 iteration.

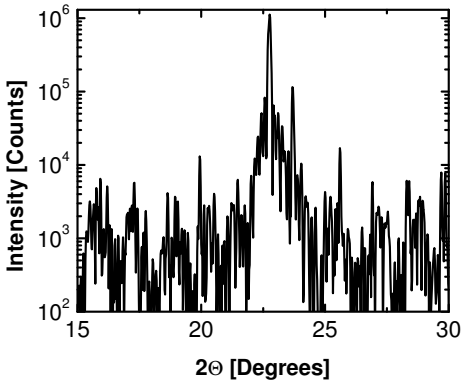

Figure C.2: Simulation using Monte-Carlo method by 10 000 iterations.

Although the rigorous calculation of Equation C.2 is almost impossible, we may simplify the process by introducing approximations. As a widely used computational algorithm, the Monte-Carlo method can be used to simulate the behavior of various physical systems. It differs from other numerical methods in its non-deterministic manner by introducing random (pseudo-random) numbers as the input parameters. Interfaces with discrete roughness in a multilayer system

are stochastic by nature, so it is possible to approximately evaluate Equation C.2 using the Monte-Carlo method.

As an example, consider the diffraction profile of a perovskite superlattice $(LaMnO_3/SrTiO_3)_{15}$ ($LaMnO_3$ layer is about 15 ML thick, $SrTiO_3$ layer is about 7 ML thick, and the number of bilayers is 15). Assume $a_1, a_2, a_3 = 3.88$ Å, $b_1, b_2 = 3.88$ Å and $b_3 = 3.96$ Å, we can simulate the XRD profile in the (001) diffraction range. Figure C.1 gives the result for a single iteration. We may repeat the evaluation several times, and the final limit as the population of the samplings goes to infinity is the exact profile for Equation C.2. Figure C.2 gives the result for 10 000 iterations. We notice that the satellite peaks in Figure C.2 are more defined then those in Figure C.1. Although the Monte-Carlo simulation usually works well when the target function is "smooth" in nature, the diffraction intensities may deviate from the mean values by orders of magnitudes. In addition, Monte-Carlo simulations with large numbers of iterations must run for extremely long periods of time. In the case of 10 000 iterations, the calculation takes about 2 hours using an Intel Core 2 Duo computer. Thus this type of simulations exhibit instability and computing inefficiency. It is also not suitable for simulations aimed at structural refinement. Therefore, Equation C.1 remains the best option for the refinement procedure.

D

Central satellite peak FWHM determination in the normal direction

The InAs/GaSb SL samples studied in Chapter II were grown on a 1 mm thick GaSb (001) buffer layer which was epitaxially grown on top of Te-doped GaSb (001) substrates. The SL 0^{th} order or central peak is not resolved from the GaSb buffer and GaSb substrate intrinsic peaks, which makes it difficult to determine the FWHM of the 0^{th} order SL peak directly from XRD data.

According to the diffraction theory of superlattices, [41] the FWHM is determined by the material Debye-Waller factor, continuous disorder (noncrystalline origin) and discrete disorder (crystalline origin). Only discrete disorder modifies the FWHM according to the order of satellite peaks. Our derivation shows that when the broadening contribution by discrete disorder is excluded from the original experimental data, the 0^{th} order peak FWHM can be obtained.

According to the theory, the high angle peaks can be indexed about the average lattice constant $\langle d \rangle$ by:

$$\frac{2\sin\Theta_m}{\lambda_{X-ray}} = \frac{1}{\langle d \rangle} \pm \frac{m}{\Lambda} = \frac{N_A + N_B \pm m}{\Lambda} \tag{D.1}$$

where, $\langle d \rangle = \frac{N_A d_A + N_B d_B}{N_A + N_B}$, $\Lambda = N_A d_A + N_B d_B$, and m is the index of satellite peaks. The variation in $\langle d \rangle$ is obtained from

$$\delta\left(\frac{2\sin\Theta_m}{\lambda_{X-ray}}\right) = \delta\left(\frac{N_A + N_B \pm m}{\Lambda}\right) + \Delta \tag{D.2}$$

where Δ is the order-independent broadening caused by factors other than discrete order. Introducing the discrete disorder in N_A and N_B, as δN_A and δN_B gives

$$\frac{2\cos\Theta_m}{\lambda_{X-ray}}\delta\Theta_m = \frac{(d_B - d_A)\,(N_B\delta N_A - N_A\delta N_B)}{\Lambda^2} \mp m\frac{(d_A\delta N_A + d_B\delta N_B)}{\Lambda^2} + \Delta \tag{D.3}$$

Because $\cos\Theta_m$ is nearly a constant over a small range around the major diffraction peak, the intercept of a linear fit of $\delta\Theta_m$ vs. m gives us the value of the first term on the right hand side of the equation, which is also the FWHM of the 0^{th} order peak. Since the actual experimental data is determined by a very complicated profile, we choose a second order polynomial fit instead of a linear fit to calculate the 0^{th} order peak FWHM, because the statistical error does not add linearly.

Bibliography

[1] Jens Als-Nielsen and Des McMorrow. *Elements of Modern X-ray Physics*. Wiley, 2001.

[2] B. E. Warren. *X-ray Diffraction*. Addison-Wesley, 1969.

[3] H. M. Rietveld. *Acta Crystallogr.*, 22:151, 1967.

[4] H. M. Rietveld. *J. Appl. Crystallogr.*, 2:65, 1969.

[5] S. K. Burley and J. B. Bonanno. *Annu. Rev. Genomics. Hum. Genet.*, 3:243, 2002.

[6] A. A. Chernov. *J. Struct. Biol.*, 142:3, 2003.

[7] D. Jeruzalmi. *Methods Mol. Biol.*, 364:2006, 2006.

[8] H. Hauptman. *Curr. Opin. Struct. Biol.*, 7:672, 1997.

[9] P. Debye. *Ann. Phys.*, 43:49, 1914.

[10] I. Waller. *Z. Phys.*, 17:398, 1923.

[11] C. B. Walker. *Phys. Rev.*, 103:547, 1956.

[12] B. E. Warren. *J. Appl. Phys.*, 25:814, 1954.

[13] H. Cole and B. E. Warren. *J. Appl. Phys.*, 23:335, 1952.

[14] H. Lipson. *Prog. Metal Phys.*, 2:1, 1950.

[15] D. R. Chipman. *J. Appl. Phys.*, 27:739, 1956.

[16] D. T. Keating and B. E. Warren. *J. Appl. Phys.*, 22:286, 1951.

[17] J. D. Jackson. *Classical Electrodynamics*. Wiley, 1998.

[18] H. Kiessig. *Ann. Phys.*, 10:769, 1931.

[19] L. G. Parrat. *Phys. Rev.*, 95:359, 1954.

[20] S. K. Sinha, E. B. Sirota, and S. Garoff et al. *Phys. Rev.*, B 38:2297, 1988.

[21] F. Peiro, A. Cornet, and J. C. Ferrer et al. *Mater. Res. Soc. Symp. Proc.*, 417:265, 1996.

[22] R. D. Twesten, D. M. Follstaedt, and E. J. Heller et al. *Bull. Am. Phys. Soc.*, 41:693, 1996.

[23] A. Mascarenhas, R. G. Alonson, and G. S. Horner et al. *Superlattices Microstruct.*, 12:57, 1992.

[24] B. K. C. Hsieh, J. N. Baillargeon, and K. Y. Cheng. *Appl. Phys. Lett.*, 57:2244, 1990.

[25] B. Simon. *Adv. Appl. Math.*, 3:463, 1982.

[26] M. Kohmoto, L. P. Kadanoff, and C. Tang. *Phys. Rev. Lett.*, 50:1870, 1983.

[27] S. Ostlund and R. Pandit. *Phys. Rev.*, B 29:1394, 1984.

[28] D. Levine and P. J. Steinhardt. *Phys. Rev. Lett.*, 53:2477, 1984.

[29] A. Hu, Z. X. Wen, and S. S. Jiang et al. *Phys. Rev.*, B 48:829, 1993.

[30] L. Esaki and R. Tsu. *IBM Res. Note*, pages RC–2418, 1969.

[31] L. Esaki and R. Tsu. *IBM J. Res. Dev.*, 14:61, 1970.

[32] L. Esaki, L. L. Chang, and R. Tsu. *Proc. 12th Int. Conf. Low Temp. Phys.*, page 551, 1970.

[33] Ivan K. Schuller. *Phys. Rev. Lett.*, 44:1597, 1980.

[34] G. A. Sai-Halasz, L. Esaki, and W. A. Harrison. *Phys. Rev.*, B 18:2812, 1978.

[35] D. L. Smith and C. Mailhiot. *J. Appl. Phys.*, 62:2545, 1987.

[36] R. Rehm, M. Walther, and J. Schmitz et al. *Proc. SPIE*, 5783:123, 2005.

[37] M. Razeghi, Y. Wei, and J. Bae et al. *Proc. SPIE*, 5246:501, 2003.

[38] Armin Segmuller and A. E. Blackeslee. *J. Appl. Crystallogr.*, 6:19, 1973.

[39] W. Sevenhans, M. Gijs, and Y. Bruynseraede et al. *Phys. Rev.*, B 34:5955, 1986.

[40] Mary Beth Stearns. *Phys. Rev.*, B 38:8109, 1988.

[41] Eric E. Fullerton, Ivan K. Schuller, and H. Vanderstraeten et al. *Phys. Rev.*, B 45:9292, 1992.

[42] E. E. Fullerton, J. Pearson, and C. H. Sowers et al. *Phys. Rev.*, B 48:17432, 1993.

[43] Yurika Ishibashi, Naoki Ohashi, and Takaaki Tsurumi. *Jpn. J. Appl. Phys.*, 39:186, 2000.

[44] C. C. Leznoff and A. B. P. Lever. *The Phthalocyanines*. Wiley, 1986-1993.

[45] A. Braun and J. Tcherniac. *Ber. Dtsch. Chem. Ges.*, 40:2907, 1907.

[46] H. Von Tobel. *Swiss Patent*, 525937, 1972.

[47] B. D. Berezin. *Izv. Vyssh. Ucheb. Zaved. Khim. Tekhnol.*, 6:841, 1963.

[48] B. D. Berezin. *Izv. Vyssh. Ucheb. Zaved. Khim. Tekhnol.*, 7:111, 1964.

[49] O. V. Gromova and M. G. Romanova. *Tekst. Prom.*, 4:57, 1973.

[50] N. Uyeda, M. Ashida, and E. Suito. *J. Appl. Phys.*, 36:1453, 1965.

[51] K. Z. Ogorodnik. *Opt. Spektrosk.*, 37:600, 1974.

[52] S. Suzuki and Y. Arai. *Japanese Kokai*, 7222429, 1972.

[53] C. Hamann. *Krist. Tech.*, 6:491, 1971.

[54] P. E. Fielding and N. C. Stephenson. *Aust. J. Chem.*, 18:1691, 1965.

[55] C. J. Brown. *J. Chem. Soc.*, A 10:2488, 1968.

[56] M. Ashida, N. Uyeda, and E. Suito. *Bull. Chem. Soc. Jpn.*, 39:2616, 1966.

[57] F. L. Pfeiffer. *U. S. Patent*, 3051721, 1962.

[58] B. P. Brand. *U. S. Patent*, 3150150, 1964.

[59] B. I. Knudsen, H. S. Rolskov, and O. L. Koge. *U. S. Patent*, 3160635, 1964.

[60] J. Sharp and M. Abkowitz. *J. Phys. Chem.*, 77:477, 1973.

[61] Stephen R. Forrest. *Chem. Rev.*, 97:1793, 1997.

[62] Zhenan Bao, Andrew J. Lovinger, and Ananth Dodabalapur. *Appl. Phys. Lett.*, 69:3066, 1996.

[63] K. Xiao, Y. Liu, and G. Yu et al. *Appl. Phys.*, A 77:367, 2003.

[64] R. Sathyamoorthy and S. Senthilarasu. *J. Electrochem. Soc.*, 154:H1, 2007.

[65] S. Yim, S. Heutz, and T. S. Jones. *J. Appl. Phys.*, 91:3632, 2002.

[66] S. Yim and T. S. Jones. *Phys. Rev.*, B 73:161305, 2006.

[67] O. Berger, W.-J. Fischer, and B. Adolphi et al. *J. Mater. Sci. - Mater. Electron.*, 11:331, 2000.

[68] R. D. Gould. *Coord. Chem. Rev.*, 156:237, 1996.

[69] M. K. Debe and K. K. Kam. *Thin Solid Films*, 186:289, 1990.

[70] S. Heutz, S. M. Bayliss, and R. L. Middleton et al. *J. Phys. Chem.*, B 104:7124, 2000.

[71] R. Prabakaran, R. Kesavamoorthy, and G. L. N. Reddy et al. *Phys. Status Solidi*, 229:1175, 2002.

[72] A. C. Brieva, T. E. Jenkins, and D. G. Jones et al. *J. Appl. Phys.*, 99:073504, 2006.

[73] Casey W. Miller, A. Sharoni, and G. Liu el al. *Phys. Rev.*, B 72:104113, 2005.

[74] A. C. Durr, F. Schreiber, and M. Munch el al. *Appl. Phys. Lett.*, 81:2276, 2002.

[75] D. L. Smith and C. Mailhiot. *Surf. Sci.*, 196:683, 1988.

[76] H. Mohseni, E. Michel, and Jan Sandoen el al. *Appl. Phys. Lett.*, 71:1403, 1997.

[77] H. Mohseni, A. Tahraoui, and J. Wojkowski et al. *Appl. Phys. Lett.*, 77:1572, 2000.

[78] H. J. Haugan, F. Szmulowicz, and G. J. Brown et al. *Appl. Phys. Lett.*, 84:5410, 2004.

[79] Yajun Wei and Manijeh Razeghi. *Phys. Rev.*, B 69:085316, 2004.

[80] F. Szmulowicz, H. Haugan, and G. J. Brown. *Phys. Rev.*, B 69:155321, 2004.

[81] H. J. Haugan, L. Grazulis, and G. J. Brown et al. *J. Cryst. Growth*, 261:471, 2004.

[82] D. W. Stokes, R. L. Forrest, and J. H. Li et al. *J. Appl. Phys.*, 93:311, 2003.

[83] Chris Pearson, C. Dorin, and J. Mirecki Millunchick et al. *Phys. Rev. Lett.*, 92:056101, 2004.

[84] N. Herres, F. Fuchs, and J. Schmitz et al. *Phys. Rev.*, B 53:15688, 1996.

[85] J. R. Waterman, B. V. Shanabrook, and R. J. Wagner et al. *Semicond. Sci. Technol.*, 8:S106, 1993.

[86] R. Kaspi. *J. Cryst. Growth*, 201/202:864, 1999.

[87] C. K. Pan, D. C. Zheng, and T. G. Finstad et al. *Phys. Rev.*, B 31:1270, 1985.

[88] B. R. Bennett. *Appl. Phys. Lett.*, 73:3736, 1998.

[89] B. R. Bennett, B. V. Shanabrook, and M. E. Twigg. *J. Appl. Phys.*, 85:2157, 1999.

[90] Dapeng Xu, A. P. Litvinchuk, and X. Wang et al. *J. Cryst. Growth*, 251:547, 2003.

[91] J. Steinshnider, J. Harper, and M. Weimer et al. *Phys. Rev. Lett.*, 85:4562, 2000.

[92] Rita Magri and Alex Zunger. *Phys. Rev.*, B 65:165302, 2002.

[93] A. Y. Polyakov, N. B. Smirnov, and A. V. Govorkov et al. *J. Vac. Sci. Technol.*, B 23:1, 2005.

[94] S. J. Xu, X. C. Wang, and S. J. Chua et al. *Appl. Phys. Lett.*, 72:3335, 1998.

[95] Leonard C. Feldman Terry L. Alford and James W. Mayer. *Nanoscale Thin Film Analysis*. Springer, 2007.

[96] Hans Lüth. *Interfaces and Thin Films*. Springer-Verlag, 2001.

[97] W. Brütting. *Physics of Organic Semiconductors*. Wiley-VCH, 2005.

[98] R. H. Tredgold. *Order in Thin Films*. Cambridge University Press, 1994.

[99] H. Hong, M. Tarbia, and H. Chayet et al. *J. Appl. Phys.*, 79:3082, 1996.

[100] M. Ashida and E. Suito N. Uyeda. *J. Cryst. Growth*, 8:45, 1971.

[101] F. Iwatsu, T. Kobayashi, and N. Uyeda. *J. Phys. Chem.*, 84:3223, 1980.

[102] M. S. Mindorff and D. E. Brodie. *Can. J. Phys.*, 59:249, 1981.

[103] J. C. Buchholz and G. A. Somorjai. *J. Chem. Phys.*, 66:573, 1977.

[104] M. Evangelisti and J. Bartolome. *Phys. Rev.*, B 66:144410, 2002.

[105] S. Lee, M. Yudkowsky, and W. P. Halperin et al. *Phys. Rev.*, B 35:5003, 1987.

[106] Hiroyuki Yamada, Toshihiro Shimada, and Atsushi Koma. *J. Chem. Phys.*, 108:10256, 1998.

[107] C. J. Brown. *J. Chem. Soc.*, A:2494, 1968.

[108] Jan Janczak and Ryszard Kubiak. *J. Alloys Compd.*, 190:121, 1992.

[109] Paolo Ballirano, Ruggero Caminiti, and Claudio Ercolani et al. *J. Am. Chem. Soc.*, 120:12798, 1998.

[110] B. Szczepaniak and P. Bragiel. *Vacuum*, 46:465, 1995.

[111] P. N. Day, Zhiqiang Wang, and R. Pachter. *J. Mol. Struct.*, 455:33, 1998.

[112] P. Wong. *Phys. Rev.*, B 32:7417, 1985.

[113] J. O. Osso, F. Schreiber, and M. I. Alonso et al. *Org. Electron.*, 5:135, 2004.

[114] Takeaki Sakurai, Ryosuke Fukasawa, and Katsuhiro Akimoto. *Jpn. J. Appl. Phys.*, 45:255, 2006.

[115] Takeaki Sakurai, Ryosuke Fukasawa, and Shunsuke Kawai et al. *Jpn. J. Appl. Phys.*, 45:397, 2006.

[116] S. Yim, T. S. Jones, and Q. Chen et al. *Phys. Rev.*, B 69:235402, 2004.

[117] Masato Ofuji, Katsuhiko Inaba, and Kazuhiko Omote et al. *Jpn. J. Appl. Phys.*, 41:5467, 2002.

[118] Masato Ofuji, Katsuhiko Inaba, and Kazuhiko Omote et al. *Jpn. J. Appl. Phys.*, 42:7520, 2003.

[119] Maskazu Nakamura, Takeshi Matsunobe, and Hiroshi Tokumoto. *J. Appl. Phys.*, 89:7860, 2001.

[120] Takuya Kambayashi, Hiromichi Ohta, and Hajime Hoshi et al. *Cryst. Growth Des.*, 5:143, 2005.

[121] Masanori Watanabe, Kenichi Sano, and Morio Inoue et al. *Appl. Surf. Sci.*, 130-132:663, 1998.

[122] O. D. Gordan, M. Friedrich, and D. R. T. Zahn. *Org. Electron.*, 5:291, 2004.

[123] O. D. Gordan, M. Friedrich, and D. R. T. Zahn. *Thin Solid Films*, 455:551, 2004.

[124] Susan M. Critchley, Martin R. Willis, and Michael J. Cook et al. *J. Mater. Chem.*, 2:157, 1992.

[125] Krishanu Ray and Hiroo Nakahara. *Phys. Chem. Chem. Phys.*, 3:4784, 2001.

[126] S. J. Park and D. P. Norton. *Surf. Coat. Technol.*, 200:5778, 2006.

[127] C. Rosenblatt, R. Pindak, and N. A. Clark et al. *Phys. Rev. Lett.*, 42:1220, 1979.

[128] J. D. Litster. *Phys. Today*, 35:5, 1982.

[129] C. Rosenblatt and N. M. Amer. *J. Appl. Phys.*, 36:432, 1980.

[130] J. Daillant and M. Alba. *Rep. Prog. Phys.*, 63:1725, 2000.

[131] H-R. Wenk and P. Van Houtte. *Rep. Prog. Phys.*, 67:1367, 2004.

[132] Herbert Goldstein. *Classical Mechanics*. Addison-Wesley, 1980.